ORSAY
SERIAL No.: 6194

Université de PARIS-SUD
U.F.R. Scientifique d'Orsay

THESIS

submitted

with a view to obtaining

the qualification of DOCTOR OF SCIENCE

FROM THE UNIVERSITY OF PARIS XI ORSAY

BY

Romuald Duperrier

SUBJECT: INTENSE BEAM DYNAMICS IN RFQs

Defended on 7 July 2000 before the examing board:

Messrs. HAISSINSKI Jacques (President)
JOLY Serge (rapporteur)
LACLARE Jean-Louis
MUELLER Alexandre
PAGANI Carlo (rapporteur)
TKATCHENKO André

to my parents,

to Evelyne,

Acknowledgements

I would like to thank Jean-Michel Lagniel, head of the IPHI project and André Tkatchenko, my thesis advisor for kindly guiding me in my work. Their help was invaluable, they were always willing to give of their time and they followed the results enthusiastically.

My deepest thanks also go to Nicolas Pichoff. He wholehartedly shared his experience with me and expressed an unfailing interest in my work. He was always there when needed and his comments were always extremely pertinent. To him I express my deepest gratitude.

I would also like to thank Didier Uriot for his patience in debugging the TOUTATIS code. His programming skills were of great assistance to me.

My thanks also go to Pierre Mattéi and Robin Ferdinand who shared with me their experience of designing the RFQ for the IPHI project.

I am also grateful to Serge Joly (CEA-SP2A, Bruyéres le Châtel) and Carlo Pagani (INFN, Milano), my thesis reporters, for their pertinent comments, thanks to which my thesis gained coherence.

I am grateful to Jean-Louis Laclare (CEA, Saclay), Alexandre Mueller (IPN, Orsay) and Jacques Haissinski (LAL, Orsay) for agreeing to be members of the examining board and accepting the ensuing responsibilities.

My special thanks go to Alessandra Lombardi (CERN). In her own time she shared with me the measurements made using RFQ2, despite the extra work this involved. This is an increasingly rare occurrence and I hope our collaboration will last for many years to come.

Finally, I wish to thank Pierre-Yves Beauvais and his group who provided me with their assistance over the last three years. They never failed to support me and were always on hand when needed.

Contents

Chapter 1

Introduction

The RFQ in high-power accelerators

The function of an accelerator is to produce a beam of charged particles with an energy and intensity corresponding to the users' requirements. It consists of a source, acceleration modules and particle transport sections. Up to now, existing equipment designs have been able to meet beam core[1] requirements whether for measurement or simulation purposes. But this is no longer the case, particularly for installations producing intense beams of protons and light ions (deutons etc.)[2].. It has been found that a small proportion of the beam can impinge on the inner wall of the structure and cause activation of the installation [1].. Activation greatly complicates maintenance. The small proportion of particles whose spread is greater than the size of the beam core is referred to as halo.

High intensity accelerators have a number of applications [2]:

- Nuclear physics and particle physics, for which injectors providing high-quality beams of ever-greater intensity are necessary (CERN, DESY, Fermilab etc.).
- Spallation neutron sources with flux increased by two orders of magnitude compared to the performance of existing reactors for biology, physics etc.
- Medical accelerators for production of radioisotopes (markers for medical imagery).
- The irradiation of materials and injection of neutral particles for heating of plasma for tokamaks (fusion with magnetic containment).
- Treatment of nuclear waste by exposure to high neutron flux produced by spallation, with or without the production of energy.
- The production of energy with a cycle based on thorium, which is more abundant than uranium.

[1] the part extending from the centre of gravity and the mean quadratic dimensions or RMS (Root Mean Square).
[2] from a few tens to a few hundred mA with high duty cycles.

- The production of tritium.

There is a great need for such facilities. Since the fifties, there have been numerous projects, and a substantial number of facilities have been built. Some were in the form of cyclotrons or linear accelerators (linacs), operating continuously or with a high duty cycle compatible with industrial scale installation requirements. Views sometimes differed as to whether to choose a cyclotron or a linac. Here we are not concerned with the relative advantages of the two types. Suffice to say that linacs are generally being chosen for most of the on-going projects, and it is this type of structure that we will consider in detail. The following section covers the stages by which energy levels in the GeV range and intensities of a few tens of mA can be reached.

The characteristics of high-power linacs

In this section, we consider the different options available for building a linac. We have limited the scope to a conventional design, as shown in Figure 1.1.

Source

An Electron Cyclotron Resonance (ECR) source is generally used. This consists of a chamber in which plasma is contained by means of a set of coils. The plasma is heated by a radiofrequency power source (magnetron or klystron). The electrons are accelerated by resonance between the magnetic field and the RF generator frequency, hence the name. The charged particles produced by ionization (protons, deutons etc.) are ejected by a set of high voltage electrodes which establish the energy of the primary beam (approximately 100 keV). The voltage of the system can also be pulsed to obtain pre-chopping of the beam. The source is followed by a transport line consisting of two solenoids for injection into an RFQ.

RFQ

The RFQ (Radio Frequency Quadrupole) linear accelerator, with which a few MeV can be reached, has a number of functions:

- bunching the particles at the selected frequency,
- accelerating, with minimal loss, the bunches formed between 100 keV and a few MeV,
- provide radial and longitudinal containment of the beam when space-charge dominated[3]..

These processes take place continuously along the axis of propagation of the particles to ensure that the system is as adiabatic as possible. This arrangement is analyzed in detail in the next section.

[3]Space charge forces are due to the decontainment potential created by the beam itself.

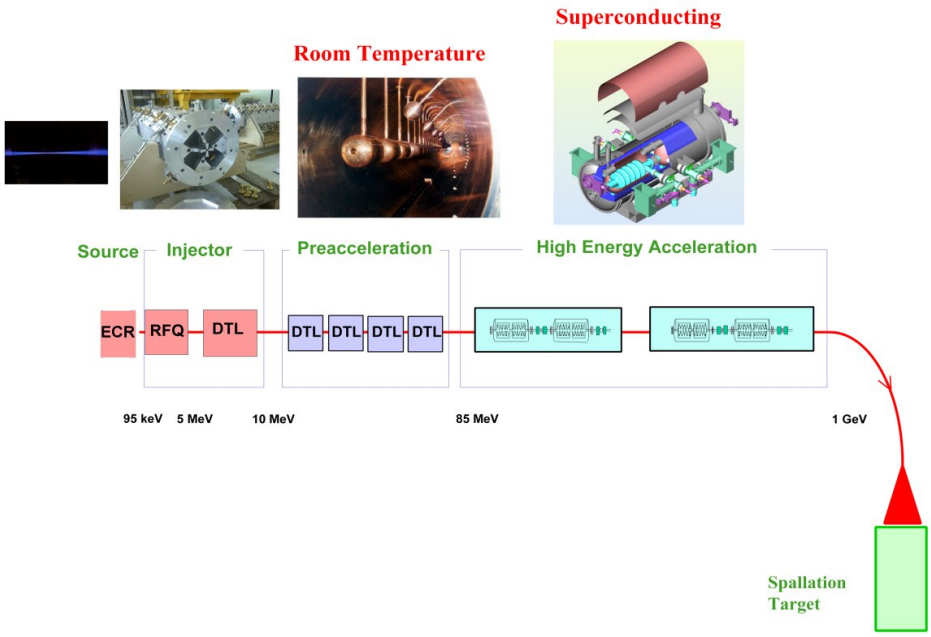

Figure 1.1: Typical high-power accelerator arrangement.

Drift Tube Linac (DTL)

This structure receives the beam of a few MeV and accelerates the bunches supplied by the RFQ up to around 100 MeV. This accelerating cavity, also referred to as an Alvarez structure [3], picks up the beam when the field produces deceleration, by means of slip tubes. Radial focusing is provided by magnetic quadrupoles placed either *in situ* (inside the slip tubes [4]), or between the cavities [5]..

Coupled Cavity Linac (CCL)

This stage uses less RF power than the DTL at energies higher than 100 MeV. Focusing is by magnetic quadrupoles placed between the cavities. The use of superconducting cavities is increasing (high accelerator gradient and efficiency). This last stage enables an energy level of 1 to 2 GeV to be reached, which is necessary for the effective production of spallation neutrons in a target placed at its end.

The main problems to be solved

The problems faced when building such linacs are numerous and complex because the levels of performance are some two orders of magnitude higher than those of existing installations. There are numerous critical issues:

- masonry structures and alignment of the installations,
- associated power supplies, correctors and quadrupoles,
- vacuum,
- provision for electricity and cooling,
- magnetic measurements and radiofrequency field measurements,
- computer systems and electronics, control system,
- design of cavities (fields and mechanical strength),
- radiological protection, resistance to radiation, nuclear safety,
- RF windows and couplers, beam/RF slaving,
- machining of components.

All these key issues are the subject of specifications reflecting the tolerance limits resulting from the beam dynamics. The validity of the tolerance limits derived from simulation is thus a critical point. It is therefore extremely important to carry out in-depth theoretical and experimental studies to gain a better understanding of the dynamics of the particles in such linacs. More specifically, in order to assess the cost and feasibility of the high-energy section (superconducting cavities representing $2/3$ of the total cost), it is indispensable to accurately characterise the beam leaving the low-energy stage (injector: source, RFQ, DTL ≤ 10 MeV) . This is the purpose of the IPHI[4] and LEDA[5] projects conducted conjointly by the CEA and CNRS[6] and by the Los Alamos National Laboratory [5, 6] (Figure 1.2) respectively. For these injectors, particle losses are critical. The consequences of any such losses are multiple: activation of the copper[7], outgasing in the cavity resulting in flashover, and erosion of the inner surface increasing the amount of flashover, to mention only the most important ones. For the last twenty years, the PARMTEQM[8] code has been the international standard for simulating the dynamics in RFQ simulators. The LANL transport code, initially written by Ken Crandall in 1979, was subsequently modified on a number of occasions by Ken Crandall himself and other contributors (Lloyd Young). The changes essentially related to image effects, space charge forces and allowance for the actual configuration of the radiofrequency fields of the beam zone (the useful zone). PARMTEQM was based on approximations simplifying treatment of the dynamics. The simplifications were

[4]French acronym standing for High-Energy Proton Injector

[5]Low Energy Demonstration Accelerator

[6]French Atomic Energy Commission and National Centre for Scientific Research

[7]The activation threshold for copper is 2.16 MeV, it is therefore extremely important to accurately know the energies of the lost particles.

[8]Phase And Radial Motion in Transverse Electric Quadrupole with Multipoles.

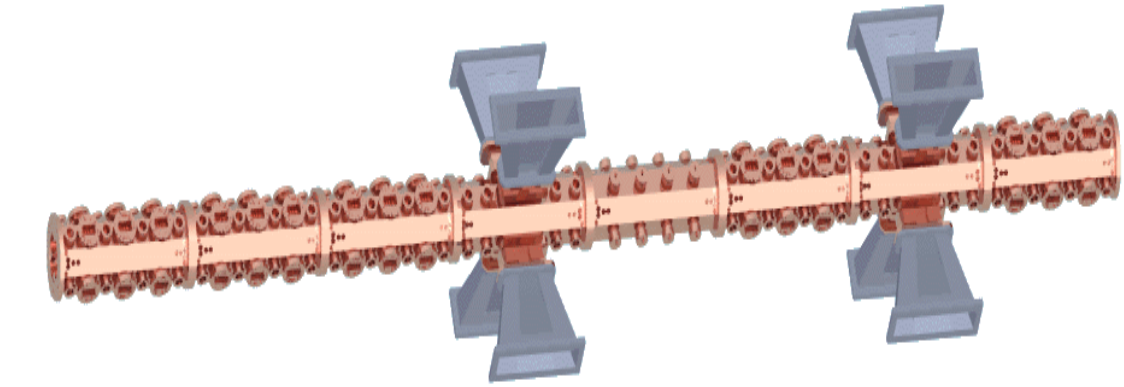

Figure 1.2: Artist's view of the IPHI project RFQ.

necessary to limit the calculation time on the computers available at the time. Since then, applications have focused on beam acceleration with very short duty cycles, with the main purpose of simulating changes in the beam core. This is no longer the case as, in addition to the change in the RMS[9] parameters, it was also necessary to gain a better understanding of the characteristics of the particles making up the halo (location of losses and energy of the lost particles) as well as those of the beam leaving the RFQ to avoid any losses in the high-energy part. This thesis analyzes the approximations used in the PARMTEQM code and quantifies their effect. The second chapter accordingly reviews the basics of the concepts used for dynamics in RFQs. The third chapter covers the hypotheses and equations used in PARMTEQM. The fourth chapter describes in detail a new transport code named TOUTATIS, which integrates time as the independent variable and calculates the fields by means of three-dimensional Cartesian grids. In the fifth chapter, this code, and its derivatives, are used to test the validity of the approximations used in the PARMTEQM code. The sixth chapter covers other work being carried out on dynamics in the RFQs.

[9]Root Mean Square.

Bibliography

[1] N. Pichoff, ”Etude théorique et expérimentale du halo d’un faisceau intense de particules chargées dans un accélérateur”, Paris Sud Orsay University thesis, 11 December 1997.

[2] J.-M. Lagniel, “Vers la construction de linacs à haute intensité”, Journées accélérateurs de la Société FranÁaise de Physique, Roscoff, 20-22 March 1995.

[3] J. Le Duff, “Dynamics and acceleration in linear structures”, CERN Accelerator School, Volume I, proc. 1992.

[4] R. Duperrier, “Optimisation des tubes de glissement du D.T.L. d’I.P.H.I.”, internal report CEA/DSM/GECA/9765.

[5] J.-M. Lagniel, “High Intensity linac studies in France”, Linac 98 conference, Chicago, p. 706.

[6] H. Vern Smith, Jr. David Schneider, “Status update on the Low Energy Demonstration Accelerator (LEDA)”, Linac 98 conference, Chicago, p. 418.

Chapter 2

The radiofrequency quadrupole

The radiofrequency quadrupole (RFQ) is a relatively recent type of linear accelerator. Although the operating principle is basically simple, the RFQ was unknown until the late sixties, when it was invented by Kapchinsky [1] and Teplyakov of the Moscow Experimental and Theoretical Physics Institute (ITEP). Major contributions were made to RFQ design by the Los Alamos National Laboratory (LANL)[2], where a demonstrator named POP (Proof Of Principle) was built and run in 1980. Since then, RFQ has become so popular that, within a few years, dozens were built and commissioned in numerous laboratories and universities throughout the world.

The main features of the RFQ are that it forms bunches, focuses and accelerates a beam of charged particles by means of RF fields only. RFQs are particularly suitable for accelerating low-energy ions (of 1 to 2 MeV per nucleon), and constitutes the best means of doing so.

This chapter covers the operating principle of the RFQ, with particular reference to beam dynamics. The electrodynamics of the structure is not considered in detail, and further information can be obtained in the abundant literature on the subject.

2.1 Operating principle of an RFQ

The operating principle of an RFQ is shown in the diagrams below. Figure 2.1 shows an electrical quadrupole with an electrode polarity that alternates with time. If a beam of charged particles is injected along the longitudinal axis of the structure, and if the particles making up the beam pass through it for a period of time such that the polarity is reversed a number of times[1], they are subjected to an alternating focusing force in each transverse plane (focusing then defocusing etc. in a given plane). The overall effect is containment of the beam. This is directly comparable to that produced by a transport line with magnetic quadrupoles at regular intervals and the polarity of the successive quadrupoles is opposite (alternate focusing).

The geometry of the poles, as described above, prevents the formation of bunches and acceleration of the beam. For this to be possible, the quadrupolar symmetry of the electrodes is

[1] this represents a compromise between the length of the quadrupole, the velocity of the particles and the polarity pulsation. In other words, the quadrupole must have a length of a few $\beta\lambda$ where $\beta = v/c$ (v is the velocity of the particles, c is the speed of light) and $\lambda = 2\pi c/\omega$ (ω is the polarity pulsation).

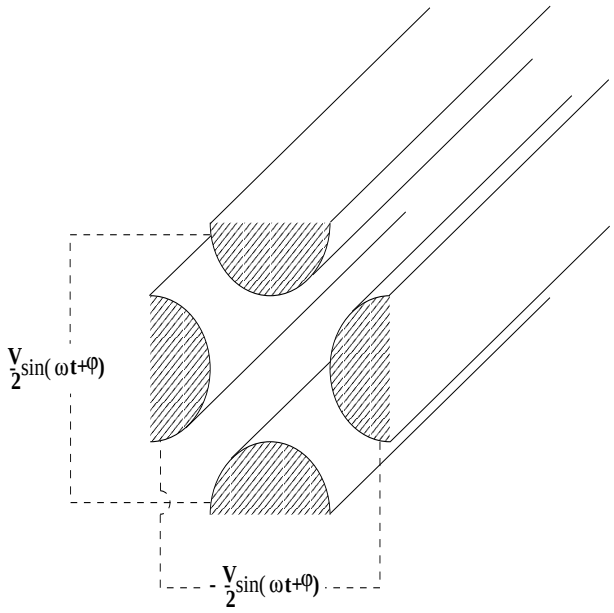

Figure 2.1: Quadrupole with alternating polarity.

disturbed (Figure 2.2). When, the horizontal poles are at a distance a from the axis, the vertical poles are at a distance $m \times a$ from the axis; m is known as the modulation factor). Its value typically varies between 1 and 2.. a is the minimum gap. The dissymmetry is inverted over a distance of $\beta_s \lambda/2$ where β_s is the relativistic factor of the synchronous particle with radiofrequency beat, and λ is the wavelength. The potential along the axis then varies periodically and a component of the longitudinal field is created. This is the key aspect of an RFQ: the period of the modulation is applied in such a manner that particles and waves are synchronized. The longitudinal force always has a focusing effect and can produce acceleration, whereas the transverse forces produce alternating focusing. It is to be noted that it is not possible to obtain a focusing force in three planes at the same time. When the particles move in time with an electromagnetic wave, the situation is virtually static and the following equation:

$$\vec{\nabla}.\vec{E} = \frac{\partial E_x}{\partial x} + \frac{\partial E_y}{\partial y} + \frac{\partial E_z}{\partial z} = 0 \tag{2.1}$$

can be applied. For there to be a focusing force in each plane at the same time, the three terms would have to have the same sign, and the equation (2.15) would therefore only be true if they were null.

An RFQ operates at high frequency, typically several tens to several hundreds of MHz (352.2 MHz for the RFQ at IPHI). The result is that at the energies considered, the cells have lengths, $\beta\lambda/2$, of the order of one centimeter. There are two types of pole geometry. In one, four rods of circular cross-section are inserted into a cylindrical cavity around the axis of the structure [3,4]. The cross-sections of the rods vary with the characteristic modulation of the RFQ (Figure 2.3). With this type of geometry, the structure is referred to as a rod type RFQ. Alternatively, the cavity can be divided into quadrants (Figure 2.4), in which case the structure is referred to as a vane

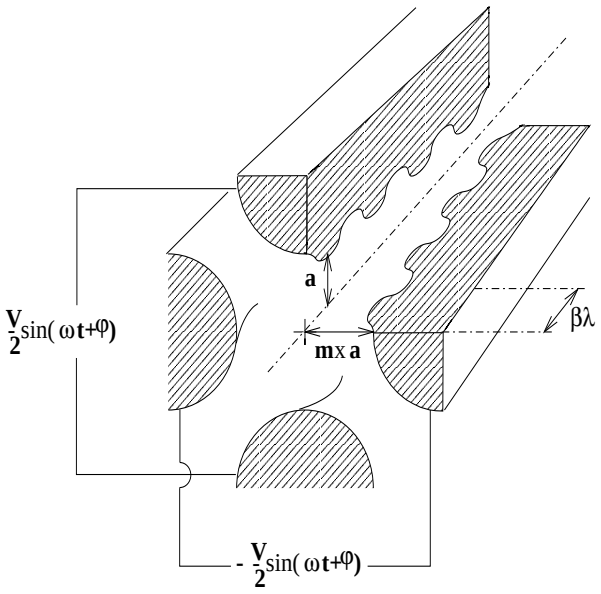

Figure 2.2: Quadrupole with alternating polarity and modulated poles (a is minimum opening, $m \times a$ is maximum opening, $\beta\lambda$ is the modulation period, and m is the modulation factor). A cell corresponds to one mesh of the geometry with a length of $\beta\lambda/2$..

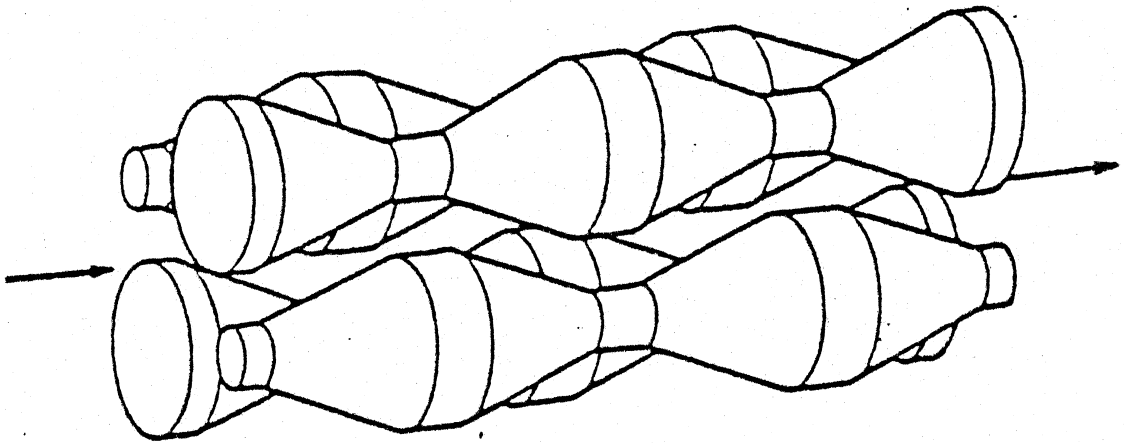

Figure 2.3: Geometry of poles in RFQs with rods.

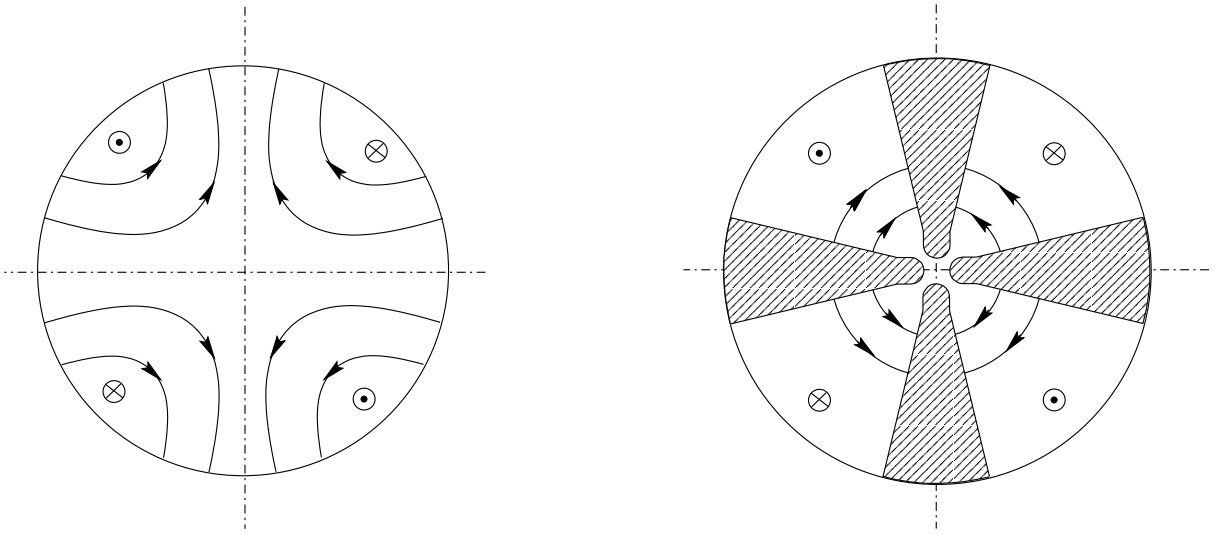

Figure 2.4: TE_{210} mode in a cylindrical cavity that is empty, i.e. not charged, and in a vane-type RFQ (cross-section at mid-length).

type RFQ. The ends of the vanes are profiled as shown in Figure 2.2.. Vane type RFQs are not considered here, although most of the issues raised apply equally well to them.

2.2 Static approximation in the useful zone

To perform the specific functions of an RFQ, a quadrupole symmetry electrical transverse mode is necessary. The TE_{210} mode is used. The third index must be null to avoid longitudinal fluctuation of the transverse focusing forces[2].. The spatial distribution of the electromagnetic fields is shown in Figure 2.4.. The magnetic lines of force pass through the plane of the page. It is frequently desirable for the designer of the electrodynamic system to be able to represent the cavity by an equivalent circuit. Figure 2.5 shows a simplified equivalent circuit for a vane type RFQ. It is to be noted that the useful zone is essentially capacitive, with the result that the vector potential, $\overrightarrow{A}$, can be disregarded for this region in the Maxwell equations. The electric field:

$$\overrightarrow{E} = -\overrightarrow{\nabla}\Psi - \frac{\partial \overrightarrow{A}}{\partial t} \tag{2.2}$$

can therefore be written as being pure divergence of a scalar potential Ψ:

$$\overrightarrow{E} = -\overrightarrow{\nabla}\Psi \tag{2.3}$$

[2]In practice, a number of views prevail. Some consider that the amplitude should be varied within a range of 10 to 20%, others consider that the amplitude should remain constant. Whatever the case, TE_{210} is used. Variation of its amplitude is obtained by adjustment of geometry.

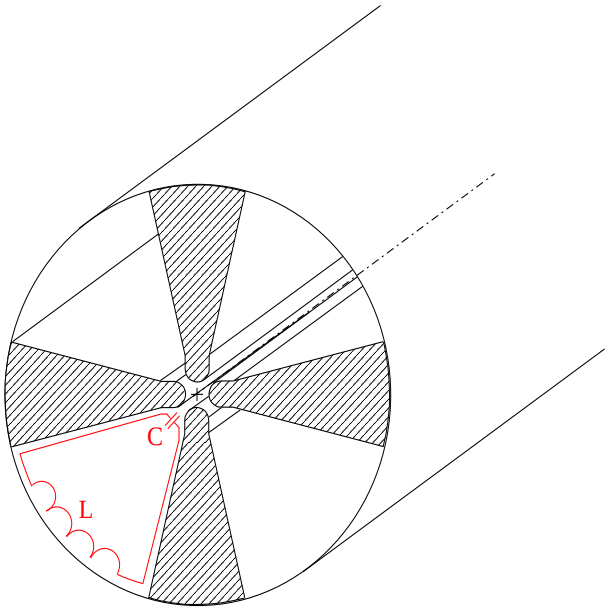

Figure 2.5: Simplified equivalent circuit for vane-type RFQ.

The consequences are extremely significant. The electrodynamic problems are totally distinct from those associated with the beam dynamics[3].. Resolution of the wave equations can, in a broad useful zone, be replaced by resolution of the Laplace equation:

$$\Delta\Psi = 0 \tag{2.4}$$

for optimal representation of the fields in the region. Two methods are available:

- An analytical solution to equation (2.4) can be opted for, and its expression determines the form of the poles.
- Criteria are adopted for imposing the shape of the poles, the resulting potential is then represented either by an appropriate harmonic base or by numeric resolution by discretization of the domain.

It should be noted that there are a number of possibilities, a fact emphasized by Kapchinsky. We are beginning to develop the approach adopted by Kapchinsky, which also serves as a basis for the PARMTEQM code. It consists in using two cylindrical coordinate Laplace equation solution harmonic basis. This technique is described in the following section. Appendix A contains a review of harmonic breakdown. For further details, a second volume by Durand on electrostatics entitled “Conductors” covers the subject in some detail [5].

[3]This is only true to a certain degree. The creation of a structure of this type necessarily involves interaction between the different disciplines (mechanics, electrodynamics, beam dynamics, vacuum, civil engineering, electronics etc.).

2.3 Cylindrical harmonics in an RFQ

The cylindrical coordinate system (r, θ, z) appears to be the most suitable (quadrupolar symmetry) for describing the potential in the useful zone of an RFQ. Equation (2.4) becomes:

$$\frac{1}{r}\frac{\partial}{\partial r}\left(r\frac{\partial \Psi(r,\theta,z)}{\partial r}\right) + \frac{1}{r^2}\frac{\partial^2 \Psi(r,\theta,z)}{\partial \theta^2} + \frac{\partial^2 \Psi(r,\theta,z)}{\partial z^2} = 0 \tag{2.5}$$

where $\Psi(r, \theta, z)$ is the electrostatic scalar potential which is multiplied by $\sin(\omega_{RF}t + \varphi)$ to allow for the radiofrequency beat effect. Solving this equation, which is detailed below, is a relatively complex matter and the reader can refer directly to page 25 to find the results. By seeking the solution of the type:

$$\Psi(r,\theta,z) = R(r)\cdot\Theta(\theta)\cdot Z(z) \tag{2.6}$$

by substituting (2.6) into (2.5), the following is obtained:

$$Z(z)\cdot\Delta_{r,\theta}\left(R(r)\cdot\Theta(\theta)\right) + R(r)\cdot\Theta(\theta)\cdot\Delta_z\left(Z(z)\right) = 0 \tag{2.7}$$

where $\Delta_{u,v}$ is the Laplacian in relation to the coordinates u and v which implies:

$$\begin{cases} \Delta_{r,\theta}\left(R(r)\cdot\Theta(\theta)\right) \mp k^2\cdot R(r)\cdot\Theta(\theta) &= 0 \\ \frac{\partial^2 Z(z)}{\partial z^2} \pm k^2\cdot Z(z) &= 0 \end{cases} \tag{2.8}$$

where k is an arbitrary constant. The second equation in (2.8) can have the following solutions:

$$\begin{array}{rcl} Z(z) &=& A\cdot\sinh(kz) + B\cdot\cosh(kz) \\ Z(z) &=& A^{'}\cdot\sin(kz) + B^{'}\cdot\cos(kz) \\ Z(z) &=& A^{''}\cdot z + B^{''} \end{array} \tag{2.9}$$

depending on whether (-), (+) or ($k = 0$) has been selected in the second equation of (2.8). For the first equation of (2.8) to be true, it is necessary that:

$$\begin{cases} r^2\frac{\partial^2 R(r)}{\partial r^2} + r\frac{\partial R(r)}{\partial r} + \left[\pm m^2 \mp (kr)^2\right]\cdot R(r) &= 0 \\ \frac{\partial^2\Theta(\theta)}{\partial\theta^2} \mp m^2\cdot\Theta(\theta) &= 0 \end{cases} \tag{2.10}$$

where m is a constant. The angular solutions are of the same type as the longitudinal solutions:

$$\begin{array}{rcl} \Theta(\theta) &=& A\cdot\sinh(m\theta) + B\cdot\cosh(m\theta) \\ \Theta(\theta) &=& A^{'}\cdot\sin(m\theta) + B^{'}\cdot\cos(m\theta) \\ \Theta(\theta) &=& A^{''}\cdot\theta + B^{''} \end{array} \tag{2.11}$$

depending on whether (-), (+) or ($m = 0$) has been selected. For the radial equation, cases where m and k are null also need to be considered. If the combination (-) and (-), or (-) and ($m = 0$) is selected, the solution will be:

$$R(r) = A \cdot I_m(kr) + B \cdot I_{-m}(kr) + C \cdot K_m(kr) + D \cdot K_{-m}(kr) \tag{2.12}$$

where $I_{\pm m}$ and $K_{\pm m}$ are modified Bessel functions of the first and second order $\pm m$, respectively. If the combination (+) and (-) is adopted, it is sufficient to replace m by $i \cdot m$ in (2.12)[4], the combination (-) or ($m = 0$) and (+) in the radial differential equation gives:

$$R(r) = A \cdot J_m(kr) + B \cdot J_{-m}(kr) + C \cdot Y_m(kr) + D \cdot Y_{-m}(kr) \tag{2.13}$$

where $J_{\pm m}$ and $Y_{\pm m}$ are Bessel functions of the first and second order $\pm m$, respectively. The expression (2.13) is also the solution for the combination (+) and (+) when m is replaced by $i \cdot m$.. The case ($k = 0$) gives:

$$\begin{array}{rcl} R(r) & = & A \cdot r^m + B \cdot r^{-m} \\ R(r) & = & A^{'} \cdot \cos(m \cdot \log(r)) + B^{'} \cdot \sin(m \cdot \log(r)) \\ R(r) & = & A^{''} \cdot \log(r) + B^{''} \end{array} \tag{2.14}$$

for (-), (+) and ($m = 0$) respectively. In short, allowing only for Bessel functions of imaginary orders, and with m and k real, a Laplace equation solution can be written with cylindrical coordinates using developments such as (2.15).

$$\begin{array}{rcl} \Psi(r,\theta,z) & = & \sum_k [A_k^1 \cdot \sinh(kz) + B_k^1 \cdot \cosh(kz)] \cdot [C_k^1 \cdot J_0(kr) + D_k^1 \cdot Y_0(kr)] \cdot [E_k^1 \cdot \theta + F_k^1] \\ & + & \sum_k \sum_m [A_{km}^2 \cdot \sinh(kz) + B_{km}^2 \cdot \cosh(kz)] \cdot [C_{km}^2 \cdot J_m(kr) + D_{km}^2 \cdot J_{-m}(kr)] \\ & & \quad \cdot [E_{km}^2 \cdot Y_m(kr) + F_{km}^2 \cdot Y_{-m}(kr)] \cdot [G_{km}^2 \cdot \cos(m\theta) + H_{km}^2 \cdot \sin(m\theta)] \\ & + & \sum_k [A_k^3 \cdot \sin(kz) + B_k^3 \cdot \cos(kz)] \cdot [C_k^3 \cdot I_0(kr) + D_k^3 \cdot K_0(kr)] \cdot [E_k^3 \cdot \theta + F_k^3] \\ & + & \sum_k \sum_m [A_{km}^4 \cdot \sin(kz) + B_{km}^4 \cdot \cos(kz)] \cdot [C_{km}^4 \cdot I_m(kr) + D_{km}^4 \cdot I_{-m}(kr)] \\ & & \quad \cdot [E_{km}^4 \cdot K_m(kr) + F_{km}^4 \cdot K_{-m}(kr)] \cdot [G_{km}^4 \cdot \cos(m\theta) + H_{km}^4 \cdot \sin(m\theta)] \\ & + & \sum_m [A_m^5 \cdot z + B_m^5] \cdot [C_m^5 \cdot r^m + D_m^5 \cdot r^{-m}] \cdot [E_m^5 \cdot \sin(m\theta) + F_m^5 \cdot \cos(m\theta)] \\ & + & [A^6 \cdot z + B^6] \cdot [C^6 \cdot \log(r) + D^6] \cdot [E^6 \cdot \theta + F^6] \\ & + & \sum_m [A_m^7 \cdot z + B_m^7] \cdot [C_m^7 \cdot \cos(m \cdot \log(r)) + D_m^7 \cdot \sin(m \cdot \log(r))] \\ & & \quad \cdot [E_m^7 \cdot \sinh(m\theta) + F_m^7 \cdot \cosh(m\theta)] \end{array} \tag{2.15}$$

This set of series will be extremely useful later on. It will be seen that Ken Crandall has made substantial use of these series and that many of them are used for different parts of the

[4] i is the pure imaginery number equal to $\sqrt{-1}$..

Coefficients that cancel out	Reasons given
$E_k^1;E_k^3;E^6;E_m^7;F_m^7$	angular periodicity
$A_k^1;B_k^1;A_{km}^2;B_{km}^2;A_m^5;A^6;A_m^7$	longitudinal periodicity
$D_k^1;E_{km}^2;F_{km}^2;D_k^3;E_{km}^4;F_{km}^4;D_m^5;C^6;C_m^7;D_m^7$	finite potential along axis (Oz)
$B^6;D^6;F^6$	null potential along axis (Oz) at mid-cell
$H_{km}^4;E_m^5$	rotated quadrupole symmetry

Table 2.1: Sorting of coefficients for RFQ in expression (2.15)

RFQ in PARMTEQM. It is now necessary to identify the terms which possess the symmetries of the RFQ. This stage is summarized in Table 2.1..

Rotated quadrupole symmetry requires that m be an even integer, $I_m(kr)$ and $I_{-m}(kr)$ then being identical. Assuming that the structure is periodic about z, which is true as long as the modulation factor varies little between cells:

$$k \to n \cdot k \tag{2.16}$$

where:

$$k = \frac{2\pi}{\beta\lambda} \tag{2.17}$$

where n is an integer. The development liable to give the best representation of the potential of the useful zone of an RFQ in cylindrical coordinates is therefore:

$$\Psi(r,\theta,z) = \frac{V}{2}\left[\sum_{m=1}^{+\infty} A_{0m}\cdot r^{2m}\cdot\cos(2m\theta) + \sum_{m=0}^{+\infty}\sum_{n=1}^{+\infty} A_{nm}\cdot I_m(kr)\cdot\cos(2m\theta)\cdot\cos(nkz)\right] \tag{2.18}$$

where $(m+n)$ is odd for quadrupolar symmetry, and V is the potential difference between the two poles. This type of series offers rapid convergence, i.e. the first terms are sufficient to obtain a high degree of accuracy.

2.4 Time/position matching

An RFQ is therefore an accelerator which uses focusing with a time-based periodicity. This raises an important issue: matching of the beam from a time-independent structure (a conventional transport line consisting of quadrupoles and magnetostatic solenoids) with that of a time-dependent structure such as an RFQ whose acceptance varies with the radiofrequency phase of the pole polarity. Ken Crandall has made a major contribution by suggesting gradual reduction of the pole gap, which has the effect of creating a ramp for the amplitude of the focusing forces

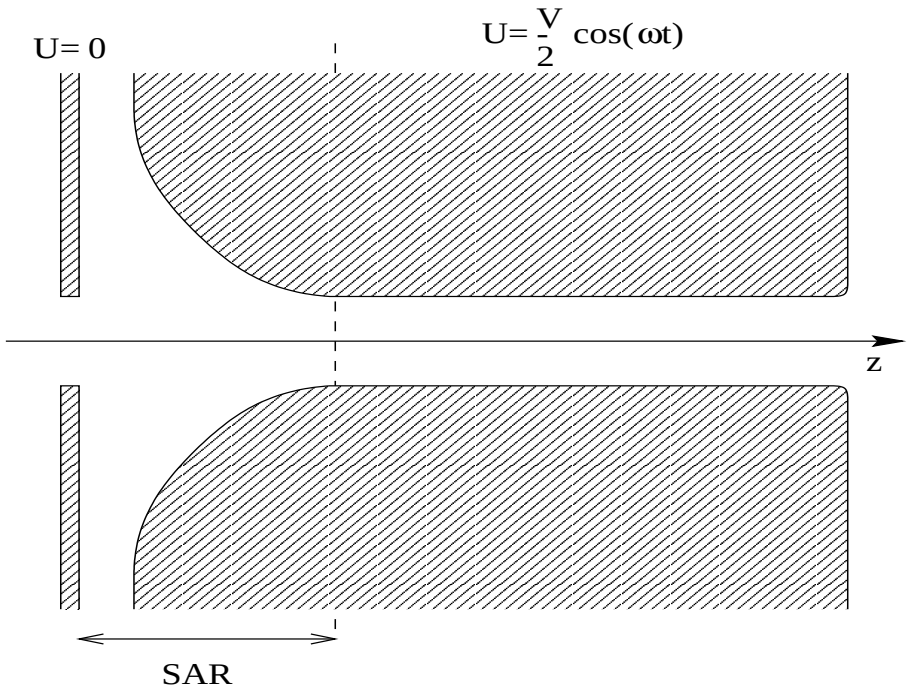

Figure 2.6: Longitudinal profile of the vanes of an RFQ in the Radial Matching Section.

(Figure 2.6). If such a ramp is created, over a certain distance and in a certain manner for example, it is possible to make the beam parameters at the end of the structures time-independent (Figure 2.7). We will explain in further detail what we mean by a certain distance and a certain manner in the next chapter.

2.5 Conclusion of chapter

In this chapter we have seen how RFQs operate, and what the start-of-the-art is for description of the useful zone on the basis of a cylindrical harmonic breakdown. The principle of time/position matching has also been described. The advantages of the PARMTEQM code remain to be considered, and this is the subject of the next chapter which contains a detailed review of the main approximations in the code, particularly as regards calculation of the fields due to the structure, calculation of the space charge forces and integration of the dynamics equations.

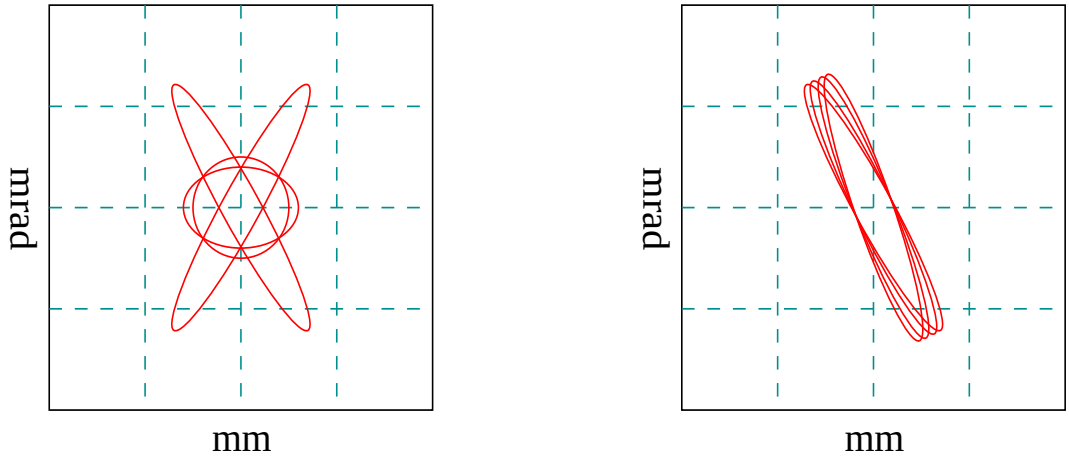

Figure 2.7: The acceptance of an RFQ with and without a Radial Matching Section at different radiofrequency phases.

Bibliography

[1] I.M. Kapchinsky and V.A Teplyakov, “Linear ion accelerator with spatially homogeneous strong focusing”, ITEP, 1970, Prib. Tekh. Eksp., Vol. 2.

[2] K. R. Crandall et al., “Radio Frequency Quadrupole beam dynamics design studies”, Proc. Linear Accelerator Conference, 1979, Vol. 3, p.205.

[3] J. M¸ller, A. Schempp, internal report 78-8, Frankfurt University, 1979.

[4] A. Schempp et al., “RFQ development at Frankfurt”, Linac 82 Conference Proceedings, page 150.

[5] E. Durand, “Electrostatique”, Masson & Cie, 1966, Volume II.

Chapter 3

PARMTEQM transport code

The PARMTEQM transport code constitutes the internationally-recognized standard for the transport of charged particles in RFQs. Before investigating the limits of its validity for the transport of intense beams, which is the subject of Chapter 5, it is first necessary to consider in detail the different techniques used in the code. This constitutes the necessary introduction to the following chapters.

3.1 The algorithm used for transport

The calculation is made on the basis of particle distribution in a 6D space (x, x', y, y', ϕ, W).. All the particles are at the same point Z_s, which corresponds to the longitudinal position of the synchronous particle. The phase relating to this synchronous particle:

$$\varphi = \phi - \phi_s \tag{3.1}$$

is used to estimate the longitudinal distribution of the bunch needed for calculation of the image[1] and space charge forces. For each particle, the forces are calculated using analytical expressions with tabulated coefficients for the external fields. These forces are applied to the particles by a leap-frog effect. For the space charge forces, the charge distribution is discretized in a 2D mesh with symmetry of revolution whenever the bunch is at mid-cell. The cross-section of the beam is then virtually circular. This discretization into rings makes it possible to calculate the forces, as the electrostatic contribution of an evenly-charged ring is precisely known. These forces are applied at each calculation increment. The effects of images are estimated at the beginning and middle of the cell by analytical expressions with tabulated coefficients, the forces being integrated over a half-cell unlike the space charge and external forces which are integrated over one tenth of a cell.

The strategy used for simulation of the transport of ions in an RFQ used in PARMTEQM can be summarized as follows: image and radiofrequency fields based on harmonic developments

[1]The effects of images are due to the charges induced by the beam on the surface of the conductor, which gives rise to a force that disturbs movement.

with tabulated coefficients, space charge fields calculated using a grid (r-z) for a bunch reconstituted by means of a transform (z→t→z), the movement integration parameter being z, with a cell discretized into 10 elements. The following sections describe a number of these stages in detail.

3.2 Calculation of the external fields

In PARMTEQM, representation of the external fields is based on the harmonic developments described in the previous chapter. Depending on the zone of the RFQ considered, certain harmonics are selected. The need for this multipolar representation was introduced in 1982 by Jean-Louis Laclare and Annick Ropert [1]. For a while, PARMTEQM made do with the two-term potential described in Appendix B..

3.2.1 The body of the RFQ

For the body of the RFQ, the first eight terms of expression (2.18) are sufficient for representing quadrupolar symmetry and longitudinal periodicity modulation of the vanes:

- the non-periodic quadrupolar term (A_{01})
- the non-periodic dodecapolar term (A_{03})
- the first periodic monopolar term (A_{10})
- the first periodic octopolar term (A_{12})
- the first periodic dodecapolar term (A_{23})
- the first periodic quadrupolar term (A_{21})
- the second periodic monopolar term (A_{30})
- the second periodic octopolar term (A_{32})

The periodicity is of course longitudinal. The non-periodic coefficients are normalized relative to R_0, the average pole gap.

The development used is therefore as follows:

$$\begin{aligned}\Psi(\rho,\theta,z) \;=\; \tfrac{V}{2}\;\{&A_{01}\left(\tfrac{\rho}{R_0}\right)^2\cos(2\theta)+A_{03}\left(\tfrac{\rho}{R_0}\right)^6\cos(6\theta)\\&+A_{10}I_0(k\rho)\cos(kz)+A_{12}I_4(k\rho)\cos(4\theta)\cos(kz)\\&+A_{21}I_2(2k\rho)\cos(2\theta)\cos(2kz)+A_{23}I_6(2k\rho)\cos(6\theta)\cos(2kz)\\&+A_{32}I_4(3k\rho)\cos(4\theta)\cos(3kz)+A_{30}I_0(3k\rho)\cos(3kz)\}\end{aligned} \tag{3.2}$$

where V is the potential difference between successive vanes. At each longitudinal position, the transverse cross-sections of the equipotential surfaces, corresponding to the above formula, are asymptotic curves due to combination of terms in $\cos(n\theta)$ where n is an integer. It is therefore impossible, in practice, to profile poles exactly in accordance with this formula, as the amplitude of the field would become infinite. The PARMTEQM code therefore uses a harmonic breakdown of a numeric solution calculated with CHARGE 3D[2] on the basis of equation (3.2) [2]. CHARGE 3D calculates the charge distribution on the surface of the poles of an RFQ, the latter being represented by semi-circles with radii and transverse positions that are variable in the longitudinal direction [3]. This variation is determined by the structure designer. Appendix B covers the different geometries used for vane-type RFQs. Once the pole geometry has been calculated by CHARGE 3D, the numerical solution is projected on the basis of harmonics in a domain where the basis is orthogonal. In view of the coordinate system selected, this domain is bounded by a cylinder of radius a.. We shall return later to the consequences of this limitation. The coefficients are calculated independently with the following relationships:

$$A_{0m} = \frac{16}{\pi V a^{2m} L_c} \int_0^{\frac{\pi}{2}} \int_0^{L_c} U(a,\theta,z) \cdot \cos(2m\theta) d\theta dz \tag{3.3}$$

$$A_{n0} = \frac{8}{\pi V I_0(nka) L_c} \int_0^{\frac{\pi}{2}} \int_0^{L_c} U(a,\theta,z) \cdot \cos(nkz) d\theta dz \tag{3.4}$$

$$A_{nm} = \frac{16}{\pi V I_{2m}(nka) L_c} \int_0^{\frac{\pi}{2}} \int_0^{L_c} U(a,\theta,z) \cdot \cos(2m\theta) \cdot \cos(nkz) d\theta dz \tag{3.5}$$

where $U(a,\theta,z)$ is the numerical solution of CHARGE 3D. The tables compile coefficients for the different cell configurations. It is these tables that are interpolated from by the PARMTEQM code to obtain the coefficients for each cell of the structure it simulates.

3.2.2 The entrance radial matching section

A number of developments have been proposed for the radial matching section of an RFQ [1,4]. The LANL codes use the following formulation:

$$\Psi(\rho,\theta,z) = \frac{V}{2} \sum_{m=0}^{3} A_m \left[I_{2m}(kr) \cdot sin(kz) + 3^{-(2m+1)} I_{2m}(3kr) \cdot sin(3kz) \right] \cdot \cos(2m\theta) \tag{3.6}$$

where the A_m are adjusted to obtain virtual continuity with the formulation for the first cell of the RFQ (curvature of vanes and potential amplitude) [5] and:

$$k = \frac{\pi}{2L_{SAR}} \tag{3.7}$$

where L_{SAR} is the entrance section length. The terms $m = 0$ allow for the possibility of starting the RFQ with a modulation, an alternative that is rarely used. To obtain the correct beam

[2]Electrostatic computer code written by Ken Crandall .

parameters for this formulation and the channel following the entrance section, the PARMTEQM user relies on the TRACE 3D code. This code, covering beam envelope transport, uses a 2×2 matrix formalism for the RFQ. It was written by Ken Crandall and is based on a simplified formulation of expression (3.6). This simplified formulation notably disregards the dodecapolar component and equates the quadrupolar component with a "pure" quadrupolar component ($A_{01} = 1$) in development (3.2).

3.2.3 Exit section

At the exit from the RFQ channel, vane modulation produces an exit potential oscillating along the longitudinal axis. Depending on the moment when the particles pass through this region, they can gain or lose energy. To control this effect, and meet the time-independent[3] beam requirement, Ken Crandall has proposed [5] a geometry generating the following potential along the axis:

$$\Psi(z,t) = \frac{3AV}{8}\left[\cos(kz) + \frac{1}{3}\cos(3kz)\right]\sin(\omega t) \tag{3.8}$$

where $z = 0$ at the beginning of the section and $z = L_{ss}$ at the end plate, $k = \pi/2L_{ss}$, ω is the radiofrequency pulse and $AV/2$ is the potential along the axis on leaving the last cell. The longitudinal field along the axis is:

$$E_z = \frac{3AV}{8}k\left[\sin(kz) + \sin(3kz)\right]\sin(\omega t) \tag{3.9}$$

Given φ, the phase of the radiofrequency when a particle is at $z = 0$, ωt can be replaced by $\varphi + k'z$, where $k' = 2\pi/\beta\lambda$.. Assuming that the variation in velocity of the particle passing through the section is negligible, the energy gain is:

$$\Delta W(\varphi, L_{sf}) = \int_0^{L_{ss}} E_z dz = \frac{3AV}{8}\left[\Im_1(L_{ss})\sin(\varphi) + \Im_2(L_{ss})\cos(\varphi)\right] \tag{3.10}$$

where:

$$\Im_1(L_{sf}) = \int_0^{\frac{\pi}{2}} \left[\sin(kz) + \sin(3kz)\right] \cdot \cos(k'z) \cdot d(kz) \tag{3.11}$$

and:

$$\Im_2(L_{sf}) = \int_0^{\frac{\pi}{2}} \left[\sin(kz) + \sin(3kz)\right] \cdot \sin(k'z) \cdot d(kz) \tag{3.12}$$

Figure 3.1 shows the variations in energy gain in unit $AV/2$ as a function of the width of section L_{sf} in unit $\beta\lambda$ and the phase of the particle at the section entrance. It should be noted that when L_{sf} is smaller than $\sim \beta\lambda/2$, the section behaves as a longitudinally focusing accelerating cell. However, the section is then too short to perform its time/position matching function. When L_{sf} is greater than $\sim 3\beta\lambda/2$, the energy gain becomes negligible and the time/position matching

[3] This is less important at the exit than at the entrance where the beam is continuous. As the bunch is formed, there is a slight extension in phase compared to the radiofrequency fields.

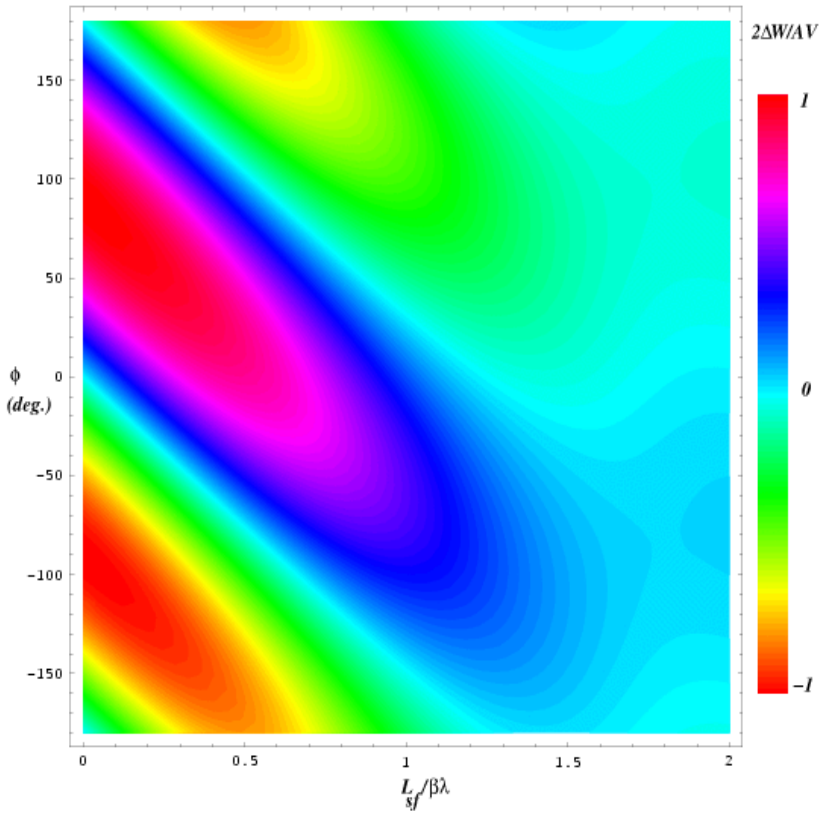

Figure 3.1: Variation in energy gain in unit $AV/2$ as a function of the length of the section L_{sf} in $\beta\lambda$ units and the phase of the particle at the section entrance.

function becomes effective when L_{sf} is greater than $\sim 2\beta\lambda$ [4].. In this case, the Twiss parameters of the beam become identical in each transverse plane. This is an advantage if a solenoid is placed after the RFQ, and a disadvantage if it is a magnetic quadrupole. In addition, the bunch is no longer kept longitudinal. These difficulties can be resolved by inserting a special cell between the exit section and the last accelerating cell. This is referred to as the transition cell and is described in the following section.

3.2.4 Transition cell

To overcome the difficulties mentioned in the preceding section and to provide a smooth transition between the dissymmetry of the last accelerating cell and the quadrupolar symmetry exit section, Ken Crandall has proposed introducing a transition cell [6] between the exit section and the last accelerating cell. This cell solves the problem of uncertainty concerning the energy introduced by the exit section and enables greater flexibility in adjusting the size and divergence of the beam at the exit. To describe the potential provided by these functions, PARMTEQM uses

[4]This action depends on the bunch phase dimension, and $2\beta\lambda$ is a good compromise.

the following formulation:

$$\Psi(\rho,\theta,z) = \frac{V}{2}\left\{\left(\frac{\rho}{R_0}\right)^2\cos(2\theta) \pm \left[A_{10}I_0(K\rho)\cos(Kz) + A_{30}I_0(3K\rho)\cos(3Kz)\right]\right\} \quad (3.13)$$

where $K = \pi/2L_{st}$ with L_{st} being the length of the transition cell. Parameters A_{10} , A_{30} and L_{st} are determined in such a manner as to ensure continuity with the adjacent sections. The horizontal and vertical profiles of the vanes are then given by:

$$\left(\frac{x}{R_0}\right)^2 - A_{10}I_0(Kx)\cos(Kz) - A_{30}I_0(3Kx)\cos(3Kz) = 1 \quad (3.14)$$

and:

$$-\left(\frac{y}{R_0}\right)^2 - A_{10}I_0(Kx)\cos(Kz) - A_{30}I_0(3Ky)\cos(3Kz) = -1 \quad (3.15)$$

The $(-)$ sign is used for the second and third terms. The horizontal vane thus begins at $m \times a$ and the vertical one at a when $z = 0$ (beginning of cell). As the longitudinal terms are null when $z = L_{st}$, the two vanes are effectively at R_0.. However, we also require the gradient to be null at the end of the cell. By differentiating equations (3.14) and (3.15) relative to z, and by imposing that drift is null at $z = L_{st}$, a relationship combining A_{10} and A_{30} is obtained:

$$A_{30} = \frac{I_0(KR_0)}{3I_0(KR_0)}A_{10} \quad (3.16)$$

Figure 3.2 shows a typical configuration of the pole profile. Parameters A_{10} and K remain to be determined. This can be done numerically using equations (3.14) and (3.15) by imposing the following boundary conditions:

$$\Psi(m \times a, 0, 0) = V/2 \quad (3.17)$$

and:

$$\Psi(a, \pi/2, 0) = -V/2 \quad (3.18)$$

as $K = \pi/2L_{st}$:

$$\Psi(R_0, 0, L_{st}) = V/2 \quad (3.19)$$

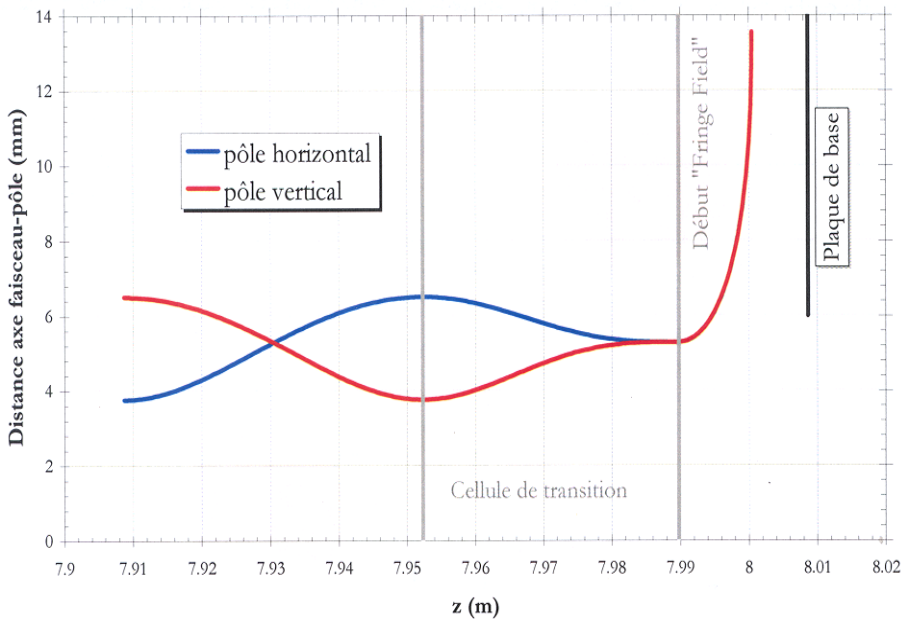

Figure 3.2: Longitudinal profile of the vanes at the end of the RFQ (transition cell + exit section).

and:

$$\Psi(R_0, \pi/2, L_{st}) = -V/2 \tag{3.20}$$

When these conditions are met, it can be demonstrated that, in the first order:

$$K^2 \approx k^2/3 \tag{3.21}$$

which gives the relationship:

$$L_{st} \approx \sqrt{3/4}\frac{\beta\lambda}{2} \tag{3.22}$$

It is also possible to demonstrate that the radii of longitudinal curvature of the formulation effectively ensure continuity with those of the neighboring cells [6]. This is why this cell is referred to as the transition cell.

3.2.5 Peak field assessment

Substantial advantages can be derived from a structure with high electrical fields, the foremost of which being that the linac is shorter and the current limits are higher. It is therefore important, at the design stage, to determine the peak field, before any consideration is given to surface condition or other parameters for the voltage capacity of the transport line. PARMTEQM can

be used to assess the peak field. The method is based on tables which contain form factors as a function of geometrical parameters (modulation, average radius, length of cell, radius of transverse curvature of the poles and the type of longitudinal profile, see Appendix B). This form factor, F, gives the peak field $\widehat{E}$ by means of the following formula:

$$\widehat{E} = F\frac{V}{R_0} \tag{3.23}$$

where V is the potential difference between adjacent poles and R_0 is the average radius. These form factors were calculated using the *CHARGE 3D* code [3]. This code calculates the surface density of charge on the RFQ poles. The peak field can then easily be calculated as it is proportional to this quantity. The stages by which *CHARGE 3D* calculates the charge surface density are described below.

The potential at a point $\overrightarrow{r}$ near to the conducting surfaces, between which there is a difference in potential, can be described as a function of the charge density σ induced on the surfaces:

$$\Psi(\overrightarrow{r}) = \sum_i \int_{S_i} \sigma_i(\overrightarrow{s}) \cdot G(\overrightarrow{r};\overrightarrow{s}) dS_i \tag{3.24}$$

where $G(\overrightarrow{r};\overrightarrow{s})$ is the potential produced at point $\overrightarrow{r}$ by the charge at point $\overrightarrow{s}$ on the i^{th} surface S_i and $\sigma_i(\overrightarrow{s})dS_i$ is the module of the charge. The technique used by the program for finding the charge density σ is as follows. The area representing the vane is assigned parameters, and x, y and z coordinates of the point considered on the surface are given by two independent variables, u and v, where $0 \leq u \leq 1$ and $0 \leq v \leq 1$:

$$\begin{cases} x &= \alpha + \rho_t\left[1 - \cos(\pi u)\right] \\ y &= \rho_t \sin(\pi u) \\ z &= Lv \end{cases} \tag{3.25}$$

where α is the longitudinal profile of the vane and ρ_t is the transverse radius of curvature which can depend on z (see Appendix B page 159)[5].. For each point on the plane (u, v) there is a corresponding point (x, y, z) on the surface of the pole. Charge density σ can also be expressed as a function of u and v and the integral (3.24) can be replaced by an integral for the plane (u, v).. σ is represented by bicubic splines whose coefficients are determined by minimization of the quantity:

$$\Re = \int_S \left[\Psi(\overrightarrow{s}) - 1\right]^2 dS \tag{3.26}$$

The result can be used to calculate the potential by multiplying by the peak voltage. The peak field directly proportional to $\hat{\sigma}$ can also be calculated. In Figure 3.3, a map of F derived from the PARMTEQM tables is plotted for the different values of m and cell length in units of R_0.. Figures 3.4 to 3.9 show maps made for different ρ_t/R_0 ratios using the scale of 1.0 to 1.8. These maps correspond to a longitudinal profile extrapolated from the two-term potential. It should be noted how F increases as ρ_t/R_0 increases and with long cells. This is due to the gap between the

[5]The vane is described by a circle alone, and no other geometrical considerations are taken into account.

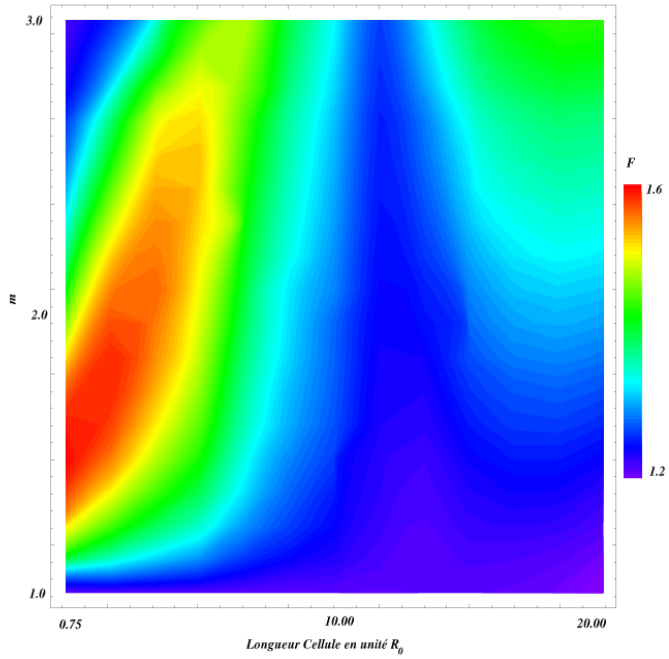

Figure 3.3: Map of F as a function of the length of the cell (in units of R_0) and m with a radius of transverse curvature, ρ_t, of $0.89 \times R_0$ with a scale of 1.2 to 1.6.

vanes and the transverse-longitudinal coupling induced by the Bessel function of the two-term potential [7]. The drop in F in certain high modulation short cells is due to unrealistic geometry [2].

3.3 Integration of the dynamics equations

The complexity of the electric field expression (includes Bessel functions) prevents analytical solving of the equation for movement in an RFQ. Incremental integration must therefore be resorted to. There are many incremental integration algorithms in the literature. For example, the Runge-Kutta algorithm and Lie algebra constitute algorithms that are frequently used in simulation of accelerator beam transport. In PARMTEQM, a leap-frog approach is used. This algorithm is based on linear discretization of the trajectories, which are linear relative to an independent parameter. In PARMTEQM, this parameter is the longitudinal position of the particle, and is referred to as z code. The longitudinal position is chosen as an independent parameter for historical reasons. It notably facilitates comparison with the diagnostics of the beam made at a given position in the transport line. There are also codes in which time is the independent parameter, referred to as t codes (LIDOS, TOUTATIS). In the leap-frog technique, acceleration, hence force, is calculated at an intermediate position between those for which the displacements are calculated. The movement equations are described in detail below to illustrate these concepts.

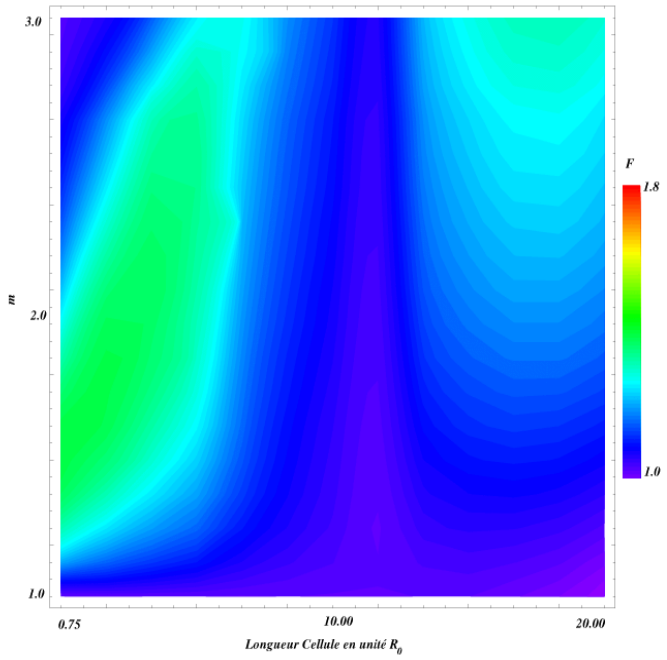

Figure 3.4: Map of F as a function of the length of the cell (in units of R_0) and m with a radius of transverse curvature, ρ_t, of $0.6 \times R_0$..

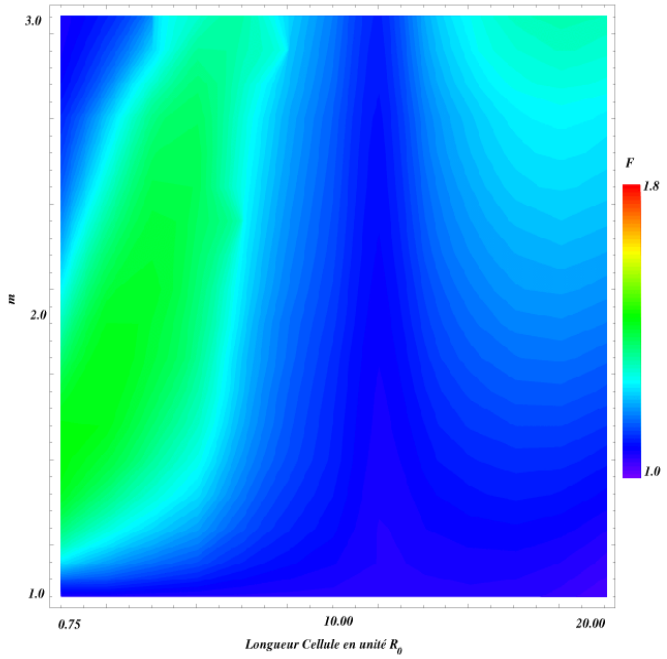

Figure 3.5: Map of F as a function of the length of the cell (in units of R_0) and m with a radius of transverse curvature, ρ_t, of $0.75 \times R_0$..

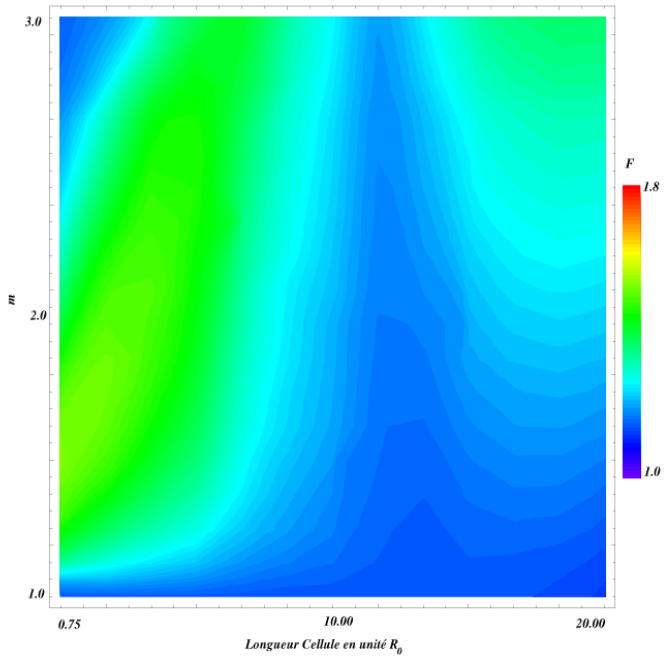

Figure 3.6: Map of F as a function of the length of the cell (in units of R_0) and m for a radius of transverse curvature, ρ_t, of $0.89 \times R_0$..

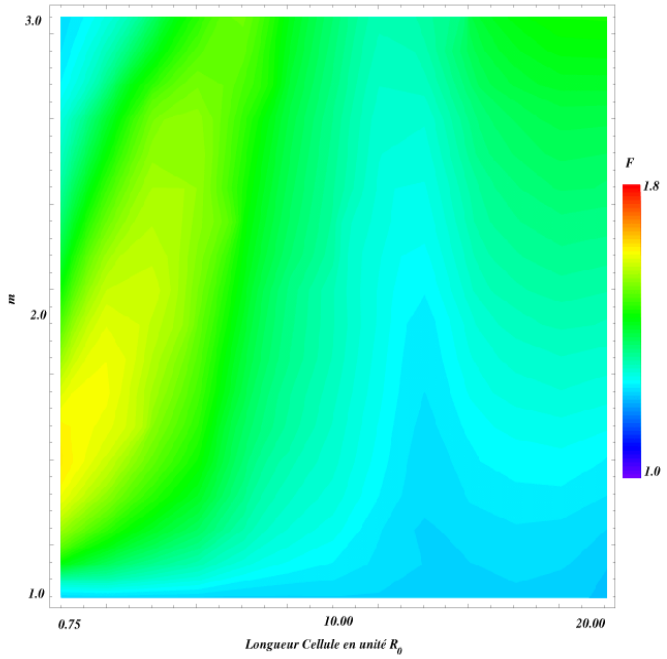

Figure 3.7: Map of F as a function of the length of the cell (in units of R_0) and m for a radius of transverse curvature, ρ_t, of $1.00 \times R_0$..

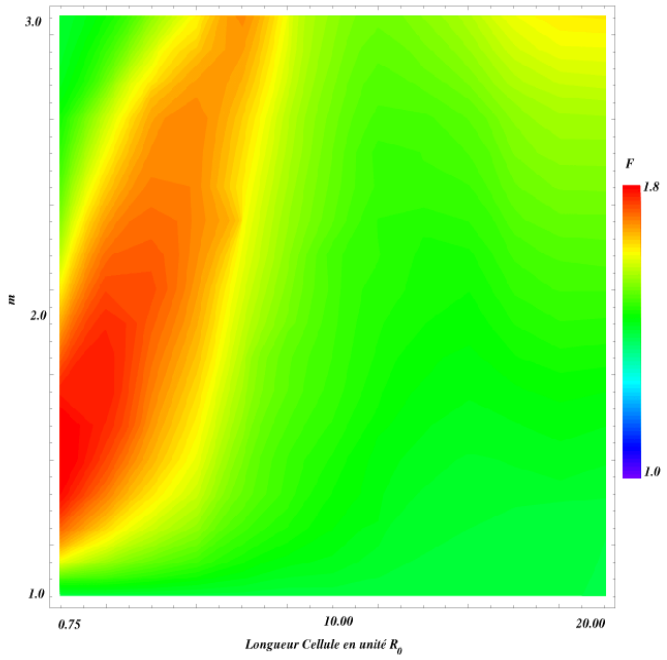

Figure 3.8: Map of F as a function of the length of the cell (in units of R_0) and m for a radius of transverse curvature, ρ_t, of $1.15 \times R_0$..

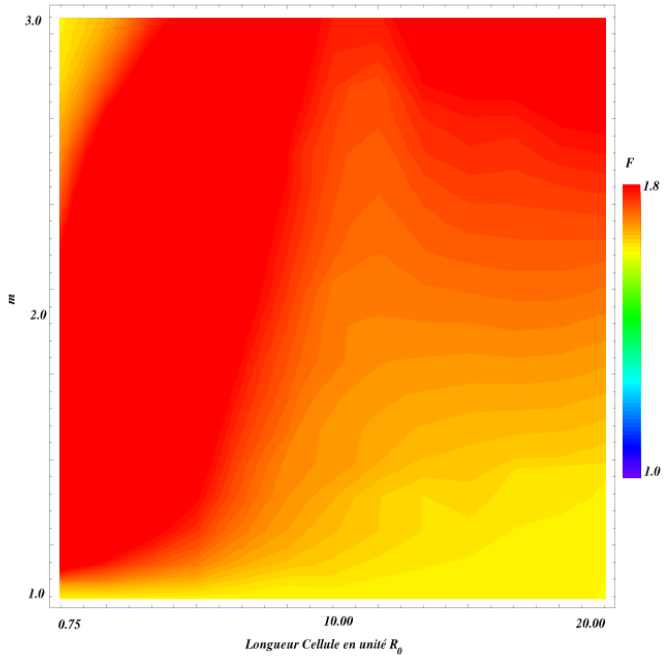

Figure 3.9: Map of F as a function of the length of the cell (in units of R_0) and m for a radius of transverse curvature, ρ_t, of $1.30 \times R_0$..

According to the fundamental principle of dynamics:

$$\frac{d\overrightarrow{p}}{dt} = Ze\overrightarrow{E} \tag{3.27}$$

where $\overrightarrow{p}$ is the quantity of movement of the particle, $\overrightarrow{E}$ the residual electric field, Z the charge number and e the elementary charge. Allowing for restricted relativity, the equation can be written as follows:

$$\frac{d(\gamma\overrightarrow{\beta})}{dt} = \frac{Zec}{E_0}\overrightarrow{E} \tag{3.28}$$

where E_0 is the energy of mass at rest and c the speed of light. To discretize the equation, consideration can be given to infinitesimal variation in the quantity $\gamma\overrightarrow{\beta}$, thus:

$$\delta(\gamma\overrightarrow{\beta}) = \frac{Zec}{E_0}\overrightarrow{E}\delta t \tag{3.29}$$

To use the longitudinal position as an independent parameter, the following variable change can be made:

$$\delta t = \frac{\delta z}{\overline{\beta_z}c} \tag{3.30}$$

where $\overline{\beta_z}c$ is the average velocity of the micro-particle as it travels over δz.. It is now possible to write the expressions necessary for incremental movement integration:

$$\left\{\begin{array}{rcl}
(\gamma\beta_x)_{i+1/2} & = & (\gamma\beta_x)_{i-1/2} + \frac{Ze}{\overline{\beta_z}E_0}E_x(\overrightarrow{OM}_i)\sin(\varphi_i)\delta z \\
(\gamma\beta_y)_{i+1/2} & = & (\gamma\beta_y)_{i-1/2} + \frac{Ze}{\overline{\beta_z}E_0}E_y(\overrightarrow{OM}_i)\sin(\varphi_i)\delta z \\
(\gamma\beta_z)_{i+1/2} & = & (\gamma\beta_z)_{i-1/2} + \frac{Ze}{\overline{\beta_z}E_0}E_z(\overrightarrow{OM}_i)\sin(\varphi_i)\delta z \\
x_{i+1} & = & x_i + x'_{i+1/2}\delta z \\
y_{i+1} & = & y_i + y'_{i+1/2}\delta z \\
\varphi_{i+1} & = & \varphi_i + \frac{\omega_{rf}}{(\beta_z)_{i+1/2}c}\delta z
\end{array}\right. \tag{3.31}$$

where:

$$\left\{\begin{array}{rcl}
x'_{i+1/2} & = & \frac{(\gamma\beta_x)_{i+1/2}}{(\gamma\beta_z)_{i+1/2}} \\
y'_{i+1/2} & = & \frac{(\gamma\beta_y)_{i+1/2}}{(\gamma\beta_z)_{i+1/2}}
\end{array}\right. \tag{3.32}$$

ω_{rf} is the radiofrequency pulse. The functional subscripts indicate that the quantity considered is calculated at an intermediate position between those at which the quantities with integer subscripts are calculated. The principle is illustrated in Figure 3.10.. The cross corresponds to calculation of the position whereas the arrows correspond to calculation of vecity.

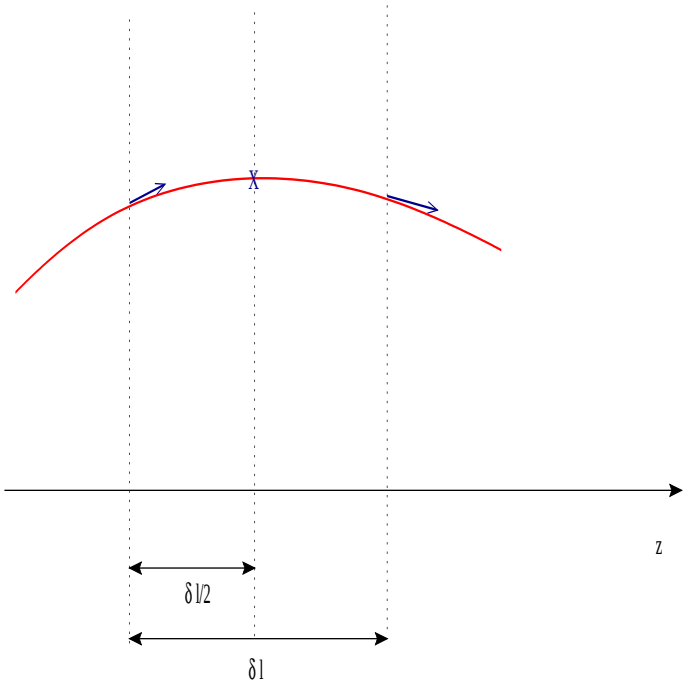

Figure 3.10: Discretization of the longitudinal trajectory by the “leap-frog” method.

The accuracy of this algorithm depends only on the size of increment δz, and no other approximations are introduced. To simplify processing and reduce calculation time[6], Ken Crandall introduced an additional simplification into this algorithm: the paraxiality hypothesis. This hypothesis provides that as the trajectories of the particles are virtually parallel to the axis of reference of the structure, the total β quantity can be equated to β_z and vice-versa:

$$\beta = \sqrt{\beta_x^2 + \beta_y^2 + \beta_z^2} \cong \beta_z \; car \; \beta_z \gg \beta_x \; et \; \beta_y \tag{3.33}$$

It is therefore necessary to replace $\overline{\beta_z}$ and $(\beta_z)_{i+1/2}$ by $\overline{\beta}$ and $(\beta)_{i+1/2}$ respectively in equations (4.4)[7] .
To evaluate these quantities, the energy gain is first calculated:

$$W_{i+1/2} = W_{i-1/2} + Ze \cdot E_z(\overrightarrow{OM}_i) \cdot \delta z \tag{3.34}$$

The transverse contribution to the total kinetic energy is therefore disregarded. Using this new value, a $\overline{\gamma}$ over δz is calculated:

$$\overline{\gamma_i} = 1 + \frac{W_{i-1/2} + W_{i+1/2}}{2E_0} \tag{3.35}$$

[6]It should be remembered that the code was written in 1977, when computers were far less powerful!

[7]In fact, it is not $\overline{\beta_z}$ which is used in PARMTEQM but $\overline{\gamma\beta_z}$.. As γ is close to 1, this is not a major problem but nevertheless a source of error.

hence:

$$(\beta_z)_{i+1/2} = \sqrt{1 - \frac{1}{\left(1 + \frac{W_{i+1/2}}{E_0}\right)^2}} \tag{3.36}$$

and:

$$\overline{\beta_i} = \sqrt{1 - \frac{1}{\overline{\gamma_i}^2}} \tag{3.37}$$

The values calculated can be used in equations (4.4). The process is therefore repeated until the desired longitudinal position is reached. The size of increment δz is one tenth of the length of the cell.

3.4 Image effects

To estimate the effects of image charges, the program uses the results of calculation derived from simulation with CHARGE 3D. This code can be used to calculate the surface distribution of charges on a conductor [3], the image charge is calculated by a beam represented either by a point charge (bunch) or by a highly charged wire (continuous beam) that is equivalent. The numerical solution is projected on a base of cylindrical harmonics:

$$\Psi(\rho,\theta,z) = K\cdot\left[\sum_{m=0}^{4} A_{2m}\left(\frac{\rho}{R_0}\right)^{2m}\cos(2m\theta) + \sum_{n=0}^{2}\sum_{m=0}^{4} A_{n,2m} I_{2m}\left(\frac{2\pi r}{\beta\lambda}\right)\cos(2m\theta)\cos\left(\frac{2\pi z}{\beta\lambda}\right)\right] \tag{3.38}$$

where K is a normalization constant defined by:

$$K = 30\frac{I}{\beta} \tag{3.39}$$

for the wire and:

$$K = 30\frac{I\lambda}{R_0} \tag{3.40}$$

for the point charge. As the beam passes from the continuous state to the modulated state in terms of density along the RFQ, it is represented as being superimposed on a cylindrical beam and a sphere, both being evenly charged. The proportion of this superimposition is determined by the two constants f_s and f_c which weight K.. These two quantities must comply with the following relationship:

$$f_s + f_c = 1 \tag{3.41}$$

To determine them, it is necessary to obtain a second relationship. The rms length of a cylindrical beam of length $\beta\lambda$ is equivalent to $\beta\lambda/2\sqrt{3}$.. The rms length, $\tilde{z}$, of the bunch is intermediate between that of a sphere and a cylinder, and is given by:

$$\tilde{z}^2 = f_c \times \frac{L_c^2}{3} + f_s \times R_s^2 \tag{3.42}$$

where $L_c = \beta\lambda/2$ is the half-length of the cylindrical beam, and $R_s = \sqrt{\tilde{x}\tilde{y}}$ is the rms radius of the sphere. By combining expressions (3.41) and (3.42), the following is obtained:

$$f_s = \frac{\frac{L_c^2}{3} - \tilde{z}^2}{\frac{L_c^2}{3} - R_s^2} \tag{3.43}$$

Once the two constants have been calculated, the tabulated forces due to the cylinder and the sphere can be weighted and applied to the particles[8].. The amplitude of these forces is small. To give an idea of proportion, for a beam with a radius equal to half the average gap, R_0, these forces represent 3% of the space charge [8]. When the beam is off the axis, harmonics of odd orders appear. The method nevertheless remains identical.

3.5 Space charge forces

3.5.1 Calculation of fields

(SCHEFF sub-program)

The space charge forces are applied to the particles at each calculation increment. These forces are calculated by interpolation in a 2D grid (r-z). This grid is calculated whenever the synchronous particle is at mid-cell, at which moment the beam is virtually round. The charge distribution reconstituted for this instant is discretized in the grid. Weights are attributed for each ring. Once each stage is completed, the fields are calculated by summing the contribution of each ring of the mesh that produces an exactly-known field. This last calculation is based on tables to reduce calculation time [8,9].

The advantage of this method is that it is not necessary to know the potential at the grid boundary, unlike in relaxation methods. This however becomes a disadvantage if the aim is to make allowance for image effects. This method cannot make allowance for interaction between pole geometry (imposed potential) and charge distribution. The use of a mesh with symmetry of revolution simplifies processing and reduces calculation time.

3.5.2 Reconstitution of a bunch at mid-cell

This is the most difficult transform made by the code. To calculate the space charge forces cleanly, it is necessary to know the positions of all the particles at a given moment. In a z code, it is the absolute phase of the particle is known at a given place in the linac. These two situations are very different, particularly when the beam has a large phase extension (low energy part of

[8] As the poles are outside the beam, the fields due to the line and the point are truly equivalent to the fields of the cylinder and sphere respectively (Gauss theorem).

the RFQ). To be able to start the process described above for calculation of the fields, the code uses a series of transform matrices which only cover the quadrupolar term. These matrices can transport particles between phases at a 5* increment (z→t transform). The reverse matrices are also determined for returning to the initial situation once the field calculation has been completed in the grid [8] (t→z transform).

3.6 Loss management

3.6.1 Transverse losses

The natural criterion for estimating whether a particle is lost or not is simply contact of the particle with the poles. Allowance therefore needs to be made for the geometry of the poles at each increment on the trajectory of each particle. To reduce the calculation time and remove the particles from the term outside the cylinder used as the integration domain for the harmonic developments, the PARMTEQM code applies a completely different criterion. For each calculation increment, the code determines whether the transverse coordinates of the particle are within a square whose size is twice the minimum gap for the cell in question. Any particles outside the square are considered to be lost. This criterion reflects the hypothesis that a particle with an amplitude such that it is outside the square cannot return inside the square.

3.6.2 Phase offset particles

At each calculation increment, all the particles therefore have the same azimuthal dimension and it is their phase φ that provides for the longitudinal distribution of the bunch. Bunching efficiency is not 100%, and in the simulation, a number of macro-particles are not accelerated. Their phase offsets continually increase, until the window of width 2π centered on the synchronous phase is not large enough to contain all the particles. As there is no practical way of increasing the size of the window[9], the trick used in PARMTEQM is to translate the phase of the offset particles by $\pm 2\pi$:

- $(+)$ if the particle is late
- $(-)$ if it is early (this can occur at the start of simulation, the digital noise associated with the space charge forces can eject the particles from the window).

This phase translation is based on the radiofrequency beat period.

[9] Allowance would then have to made for neighboring bunches.

3.7 Conclusion of chapter

This chapter shows the various simplified hypotheses used in the PARMTEQM code. In terms of present-day requirements for high-current RFQ projects, these simplifications can raise the following questions: what errors can they cause and, if there are any errors, what is their relative importance for transmission, distribution of the beam at the exit, and the location of losses? To answer these questions, it is necessary to have experimental or theoretical reference material, or to remove the approximation from the PARMTEQM code, depending on the case.

The following chapter describes the process of creation of a new transport code which reduces the number of working hypotheses and will be used as a reference for a number of the comparative studies in Chapter 5.

Bibliography

[1] J.L. Laclare, A. Ropert, “The Saclay RFQ”, internal report L.N.S. 063, 1 June 1982.

[2] K.R. Crandall, “Effects of vane-tip geometry on the electric fields in Radio-Frequency Quadrupole Linacs”, L.A.N.L. report LA-9695-MS, 1983.

[3] K.R. Crandall, “Computation of Charge Distribution On or Near Equipotential Surfaces”, L.A.N.L. report LA-3512 , December 1966.

[4] N. Tokuda, S. Yamada, “New Formulation of the Radial Matching Section”, Proceedings Linac conference 81, 19-23 October 1981, Santa Fe, LANL report LA-9234-C, 313 , February 1982.

[5] K.R. Crandall, “RFQ radial Matching Sections and fringe fields”, Proceedings Linac 84, p. 109, GSI-84-11.

[6] K.R. Crandall, “Ending RFQ vanetips with quadrupole symmetry”, Proceedings Conference Linac 94, 1994, p.227.

[7] R. Duperrier, “Calculs du champ électrique maximum dans une cellule RFQ”, CEA/DSM/DAPNIA/SEA/IPHI/9843 report, August 1998.

[8] K. R. Crandall, R. H. Stokes, T. P. Wangler, “RF Quadrupole Beam Dynamics Design Studies”, Linac 1979.

[9] N. Pichoff, “Etude théorique et expérimentale du halo d’un faisceau intense de particules chargées dans un accélérateur”, Paris Sud Orsay University thesis, 11 December 1997.

Chapter 4

The TOUTATIS transport code

A high-power linear accelerator can only operate if activation of the structure remains acceptable. For the low-energy stage, the RFQ structure is the part most sensitive to particle loss, which must be predicted with the greatest possible accuracy. The TOUTATIS code was written to meet this requirement, and reduces to a minimum the hypotheses and approximations for the transport of intense beams in RFQs. This chapter describes the numerical methods used to finalize the code.

4.1 Algorithm for simulating transport in an RFQ

The strategy used in the TOUTATIS code for simulating transport is shown schematically in Figure 4.1.. The process begins with distribution of macro-particles in 6D space (i.e. 3 for position and 3 for velocity). The centroid of the positions is calculated to determine the longitudinal position of the bunch in the RFQ. All the grids used in the numerical calculations are centered on this azimuthal zone. Once the position is determined, a mesher discretizes the geometry of the RFQ poles in the vicinity of the distribution. This charge distribution is discretized in the same grid to allow for space charge and image effects. The discretization of the charges is carried out by linear interpolation to neighboring nodes[1].. During this stage, the vanes are polarized with allowance for radiofrequency scalar potential amplitude and time. Once this grid preparation stage is completed, a process for solving the Poisson equation is begun. Once this process is completed, the forces derived from the numerical solution are applied to the particles using a leap-frog approach. The process then enters a loop until the desired longitudinal position is reached.

This section outlines the transport algorithm used in TOUTATIS. The following sections cover the different stages in greater detail.

[1] This type of discretization is referred to as cloud in cell.

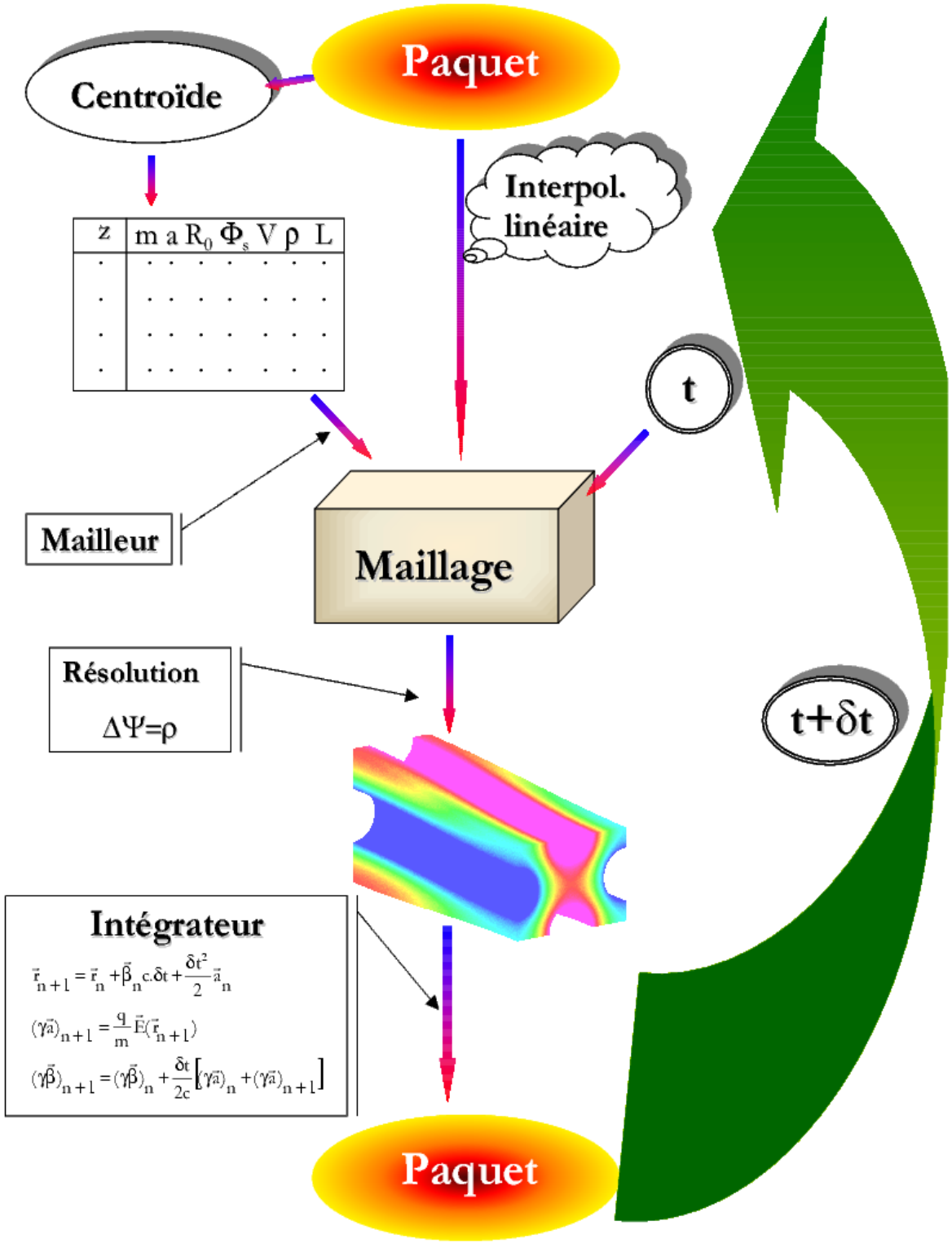

Figure 4.1: Algorithm used in TOUTATIS.

4.2 Movement equation integration

TOUTATIS is based on incremental integration of movement, the integration being somewhat more complex than that of PARMTEQM. Another difference is that the independent parameter is time, and it is therefore referred to as a t code. The choice of time as the independent parameter in TOUTATIS is a straightforward one. It is even unavoidable if the aim is to accurately calculate the self-consistent forces of the beam in a simple manner (i.e. space charge and image effects). It is to be noted that the Russian LIDOS code is also time-based, but uses a leap-frog approach.

Beam emittance is directly proportional to the Jacobian of the transform. To ensure that the integration system does not result in spurious variation of emittance, the Jacobian of the transform must be equal to 1. In detail, according to the basic principles of dynamics:

$$\frac{d\overrightarrow{p}}{dt} = Ze\overrightarrow{E} \tag{4.1}$$

where $\overrightarrow{p}$ is the quantity of movement of the particle and $\overrightarrow{E}$ the residual electric field, while Z is the charge state and e is the elementary charge. Allowing for restricted relativity, the equation can be written as follows:

$$\frac{d(\gamma\overrightarrow{\beta})}{dt} = \frac{Zec}{E_0}\overrightarrow{E} \tag{4.2}$$

with E_0, the energy of mass at rest and c the speed of light. To discretize this equation, infinitesimal variation in quantity $\gamma\overrightarrow{\beta}$ is considered, giving:

$$\delta(\gamma\overrightarrow{\beta}) = \frac{Zec}{E_0}\overrightarrow{E}\delta t \tag{4.3}$$

It is now possible to write the expressions necessary for integration of incremental movement [1]:

$$\left\{\begin{array}{rcl} x_{i+1} & = & x_i + (\beta_x)_i c\delta t + \frac{Zec^2}{\gamma_i E_0}E_x(\overrightarrow{OM}_i)\frac{\delta t^2}{2} \\ y_{i+1} & = & y_i + (\beta_y)_i c\delta t + \frac{Zec^2}{\gamma_i E_0}E_y(\overrightarrow{OM}_i)\frac{\delta t^2}{2} \\ z_{i+1} & = & z_i + (\beta_z)_i c\delta t + \frac{Zec^2}{\gamma_i E_0}E_z(\overrightarrow{OM}_i)\frac{\delta t^2}{2} \\ (\gamma\beta_x)_{i+1} & = & (\gamma\beta_x)_i + \frac{\delta t}{2}\frac{Zec}{E_0}\left[E_x(\overrightarrow{OM}_i) + E_x(\overrightarrow{OM}_{i+1})\right] \\ (\gamma\beta_y)_{i+1} & = & (\gamma\beta_y)_i + \frac{\delta t}{2}\frac{Zec}{E_0}\left[E_y(\overrightarrow{OM}_i) + E_y(\overrightarrow{OM}_{i+1})\right] \\ (\gamma\beta_z)_{i+1} & = & (\gamma\beta_z)_i + \frac{\delta t}{2}\frac{Zec}{E_0}\left[E_y(\overrightarrow{OM}_i) + E_y(\overrightarrow{OM}_{i+1})\right] \end{array}\right. \tag{4.4}$$

in which factor γ_i alone is necessary to isolate the velocities, obtained with the expression:

$$\gamma_i = \sqrt{1 + \left[(\gamma\beta_x)_i\right]^2 + \left[(\gamma\beta_y)_i\right]^2 + \left[(\gamma\beta_z)_i\right]^2} \tag{4.5}$$

This system involves storing the fields experienced by the particle at increment i so as to be able to calculate the velocities at increment $i+1$.. Increment δt is typically equal to one twentieth of

the radiofrequency period. Let us check that the Jacobian of the transform is effectively equal to 1:

$$\Im = \begin{vmatrix} \frac{\partial u_{i+1}}{\partial u_i} & \frac{\partial u_{i+1}}{\partial v_i} \\ \frac{\partial v_{i+1}}{\partial u_i} & \frac{\partial v_{i+1}}{\partial v_i} \end{vmatrix} \tag{4.6}$$

where $u = x, y, z$ and $v = \gamma\beta_x, \gamma\beta_y, \gamma\beta_z$.. As the force depends only on position (electric field), the following is obtained:

$$\begin{array}{rcl} \frac{\partial u_{i+1}}{\partial u_i} & = & 1 + \frac{Zec^2}{\gamma_i E_0}\frac{\delta t^2}{2}\frac{\partial E_u(\overrightarrow{OM}_i)}{\partial u_i} \\ \frac{\partial u_{i+1}}{\partial v_i} & = & \frac{c\delta t}{\gamma_i} \\ \frac{\partial v_{i+1}}{\partial u_i} & = & \frac{\delta t}{2}\frac{Ze}{\gamma_i E_0}\left\{\frac{\partial E_u(\overrightarrow{OM}_i)}{\partial u_i} + \frac{\partial E_u(\overrightarrow{OM}_{i+1})}{\partial u_i}\left[1 + \frac{\delta t^2}{2}\frac{Zec}{\gamma_i E_0}\frac{\partial E_u(\overrightarrow{OM}_i)}{\partial u_i}\right]\right\} \\ \frac{\partial v_{i+1}}{\partial v_i} & = & 1 + \frac{\delta t^2}{2}\frac{Zec}{\gamma_i E_0}\frac{\partial E_u(\overrightarrow{OM}_{i+1})}{\partial u_i} \end{array} \tag{4.7}$$

By substitution into (5.23), the calculation of $\Im$ gives:

$$\begin{array}{rcl} \Im & = & \left[1 + \frac{Zec^2}{\gamma_i E_0}\frac{\delta t^2}{2}\frac{\partial E_u(\overrightarrow{OM}_i)}{\partial u_i}\right] \times \left[1 + \frac{\delta t^2}{2}\frac{Zec}{\gamma_i E_0}\frac{\partial E_u(\overrightarrow{OM}_{i+1})}{\partial u_i}\right] \\ & & -\frac{c\delta t^2}{2}\frac{Ze}{\gamma_i^2 E_0}\left\{\frac{\partial E_u(\overrightarrow{OM}_i)}{\partial u_i} + \frac{\partial E_u(\overrightarrow{OM}_{i+1})}{\partial u_i}\left[1 + \frac{\delta t^2}{2}\frac{Zec}{\gamma_i E_0}\frac{\partial E_u(\overrightarrow{OM}_i)}{\partial u_i}\right]\right\} \\ & = & 1 \end{array} \tag{4.8}$$

Therefore, this algorithm does indeed conserve emittance in the phase space at each increment of linear transport.

4.3 Calculation of electrical potential

Control of particle losses necessitates accurate determination of the electrical fields. As discussed in Chapter 2, the Poisson equation needs to be considered:

$$\Delta\Psi(\overrightarrow{r}) = \rho(\overrightarrow{r}) \tag{4.9}$$

where $\Psi(\overrightarrow{r})$ is the electrical potential and $\rho(\overrightarrow{r})$ is the charge density per unit volume [1].. The special shape of the poles and the multiple configurations of $\rho(\overrightarrow{r})$ prevent the use of analytical solutions of equation (4.9) (discontinuities of poles [2, 3], beam envelope corresponding to modulation [4], etc.). Numerical solution of equation (4.9) remains the only realistic alternative and present-day progress in computer systems now makes it a possibility for RFQs. In the following sections, the methods used for solving the Poisson equation in the TOUTATIS code are reviewed.

4.3.1 The finite differences method

To situate the problem, let us assume that the useful zone is covered with a net of cubic meshes of side h and that the electrical potential is known at a few points in the net (i.e. the electrodes). As the potential sought corresponds to equation (4.9), we can see that the value Ψ_i of the potential at node i is equal to a linear combination of the values of the neighboring nodes. Value $\Psi_{(h)}$ obtained at a point in the discrete problem for a certain value of h, differs from the exact value of Ψ of the known problem, but the error:

$$\varepsilon_h = \Psi - \Psi_{(h)} \tag{4.10}$$

tends to zero when $h \rightarrow 0$ [5].. It is therefore possible to get as close to the exact value as is desired. The finite differences method is the easiest to implement and the most general. It provides a result in every case. The section contains a detailed description of the main issues in implementing the method.

4.3.1.1 Developments

In the vicinity of a coordinate point (x_0, y_0, z_0), a regular function and its derivatives can be developed as a Taylor series of the following type:

$$\Psi(x,y,z) = \Psi_0 + \sum_{l}^{\infty}\sum_{m}^{\infty}\sum_{n}^{\infty} a_{lmn}(x-x_0)^l(y-y_0)^m(z-z_0)^n \tag{4.11}$$

where $\Psi_0 = \Psi(x_0, y_0, z_0)$.. If the development is limited to k terms and if it is true for k points close to (x_0, y_0, z_0), the result is a system of k linear equations for determining the a_{lmn} coefficients as a function of $(\Psi_1 - \Psi_0)...(\Psi_k - \Psi_0)$.. The a_{lmn} are partial derivatives of Ψ in (x_0, y_0, z_0)[2].. If this function corresponds to a partial derivative equation, this equation can be transformed into a relationship linking Ψ_0 and Ψ_1,Ψ_2, ...Ψ_k.. Here, the partial derivative equation is the Poisson equation.

[2]Note: If f(x) can be developed as a Taylor series, this function corresponds to:

$$f(x) = \sum_{n=0}^{\infty} a_n x^n$$

where:

$$a_n = \frac{f^{(n)}(0)}{n!}$$

4.3.1.2 Second order approximation

When series (4.11) is limited to the second order, $\Psi(x,y,z)$ can be written as follows:

$$\begin{aligned}\Psi(x,y,z) &= \Psi_0 + (x-x_0)\left.\frac{\partial\Psi}{\partial x}\right|_0 + (y-y_0)\left.\frac{\partial\Psi}{\partial y}\right|_0 + (z-z_0)\left.\frac{\partial\Psi}{\partial z}\right|_0 \\ &\quad +\tfrac{1}{2}(x-x_0)^2\left.\frac{\partial^2\Psi}{\partial x^2}\right|_0 + \tfrac{1}{2}(y-y_0)^2\left.\frac{\partial^2\Psi}{\partial y^2}\right|_0 + \tfrac{1}{2}(z-z_0)^2\left.\frac{\partial^2\Psi}{\partial z^2}\right|_0 \\ &\quad +(x-x_0)(y-y_0)\left.\frac{\partial^2\Psi}{\partial x\partial y}\right|_0 + (x-x_0)(z-z_0)\left.\frac{\partial^2\Psi}{\partial x\partial z}\right|_0 + (z-z_0)(y-y_0)\left.\frac{\partial^2\Psi}{\partial y\partial z}\right|_0\end{aligned} \tag{4.12}$$

By writing that (4.12) is satisfied at 6 points close to (x_0, y_0, z_0), a system of 6 linear equations is obtained. This can be used to determine the derivatives:

$$\left.\frac{\partial^2\Psi}{\partial x^2}\right|_0 ; \left.\frac{\partial^2\Psi}{\partial y^2}\right|_0 ; \left.\frac{\partial^2\Psi}{\partial z^2}\right|_0 \tag{4.13}$$

at point (x_0, y_0, z_0).. It is then necessary to determine these formulas for the cases where the reference point is "distant from" or "close to" the surface of the conductor. This surface constitutes a boundary of the Dirichlet type (normal field). We will discuss the two-dimensional case only to avoid unnecessarily complicating the expressions. The finite differences equations for the three-dimensional case are obtained in the same manner.

4.3.1.3 Application to normal branches for internal nodes

Normal branches correspond to cases where the neighboring points are at equal distances from the reference point (Figure 4.2). By writing (4.12) at points 1, 2, 3 and 4, the following relationships are obtained:

$$\begin{cases} h^2\left.\frac{\partial^2\Psi}{\partial x^2}\right|_0 = \Psi_1 + \Psi_3 - 2\Psi_0 \\ \\ h^2\left.\frac{\partial^2\Psi}{\partial y^2}\right|_0 = \Psi_2 + \Psi_4 - 2\Psi_0 \end{cases} \tag{4.14}$$

If Ψ complies with equation (4.9), the second order approximation, nesting (4.9) and (4.14), gives:

$$4\Psi_0 = \Psi_1 + \Psi_2 + \Psi_3 + \Psi_4 - h^2\rho_0 \tag{4.15}$$

which is effectively the relationship sought. ρ_0 is the source term at point 0.. This value results from discretization of the charges in the grid. This relationship is applied to each node of the net by successive iterations. During each iteration, as the new values are calculated, they are used for calculating the following nodes, in accordance with the Gauss-Seidel method[3].. The following section relates to nodes at a distance less than h from the surface of the conductor.

[3]Unlike the Jacobi method, where the recalculated values are reused at the next iteration. The convergence is then less rapid and twice as much memory has to be set aside.

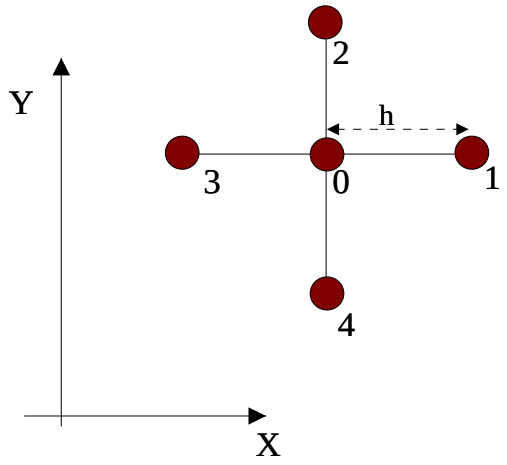

Figure 4.2: Geometrical configuration with normal branches.

4.3.1.4 Application to unequal branches with internal modes

When the node in question is at a distance less than h from the surface of the conductor, it is necessary to allow for the actual distance between it and the node in order to avoid "steps" in the geometrical representation of the conductor[4].. Considering expression (4.12), at points 1, 2, 3 and 4 of Figure 4.3, the following is obtained:

$$\begin{cases} \left(\frac{h_1+h_3}{2}\right)\left.\frac{\partial^2\Psi}{\partial x^2}\right|_0 = \frac{1}{h_1}(\Psi_1-\Psi_0)+\frac{1}{h_3}(\Psi_3-\Psi_0) \\ \left(\frac{h_2+h_4}{2}\right)\left.\frac{\partial^2\Psi}{\partial y^2}\right|_0 = \frac{1}{h_2}(\Psi_2-\Psi_0)+\frac{1}{h_4}(\Psi_4-\Psi_0) \end{cases} \tag{4.16}$$

By substituting these expressions into (4.9), the Poisson equation is obtained, in the following form:

$$\left[\frac{1}{h_1h_3}+\frac{1}{h_2h_4}\right]\Psi_0 = \frac{1}{(h_1+h_3)}\left(\frac{\Psi_1}{h_1}+\frac{\Psi_3}{h_3}\right)+\frac{1}{(h_2+h_4)}\left(\frac{\Psi_2}{h_2}+\frac{\Psi_4}{h_4}\right)-\frac{1}{2}\rho_0 \tag{4.17}$$

This is the unequal branch equation sought. The expression is extremely practical when the dimensions of the grid differ with direction. In the present case, the longitudinal and transverse dimensions, which are functions of $\beta\lambda$ and the average gap respectively, can effectively be very different (β is the relativistic velocity of the synchronous particle and λ the length of the radiofrequency wave). This point is covered in detail in Section 4.3.2.1..

[4]The analyst is then forced to considerably increase node density to properly represent the conductor.

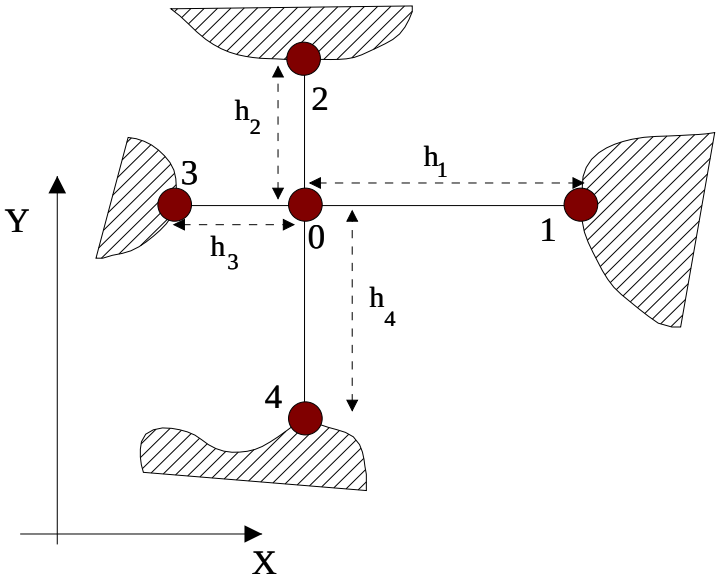

Figure 4.3: Diagram illustrating the unequal branch case.

4.3.1.5 Grid boundary conditions

4.3.1.5.1 Transverse plane

When the nodes at the edge of the net are at a distance greater than h from any conductor as measured from the center of the grid towards the edge, we impose that the flux through the boundary is null (Neumann condition). Flux $\overrightarrow{E}$ is given by the following relationship:

$$\overrightarrow{E} = -\overrightarrow{\nabla}\Psi \tag{4.18}$$

A Neumann condition on a horizontal surface therefore signifies that $E_y = 0$.. This approximation is acceptable as long as the true flux existing at the boundary does not affect the solution in the useful zone. In practice, this Neumann condition is applied by imposing that $\Psi_2 = \Psi_0$ in (4.14) with 2, a hypothetical point, at a distance of h outside the mesh (Figure 4.4).

4.3.1.5.2 Longitudinal plane

Two cases arise:

- the grid is in a part of the RFQ structure that can be equated to a channel mesh, the front and rear sides of the mesh are thus identical (toroidal mesh of square cross-section). This condition makes it possible to include the effect of adjacent bunches.
- the grid is either at the end of the structure, or in a zone where there is a discontinuity in the poles (i.e. radiofrequency coupling gap), and a Neumann condition is imposed on the two surfaces. It has also been verified that the disturbance caused by the Neumann condition is negligible relative to that caused by the gap itself.

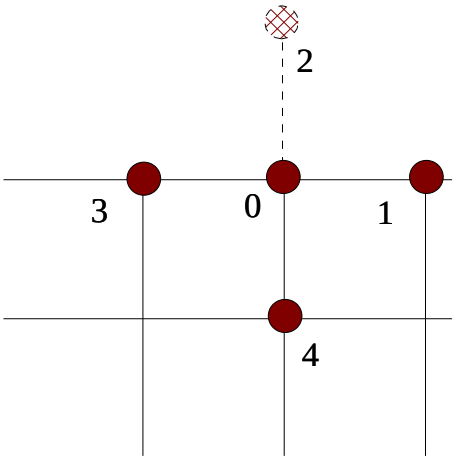

Figure 4.4: Application of Neumann condition to node 0, i.e. $\Psi_2 = \Psi_0$ in (4.14).

The fundamental principles of the finite differences method having been established, it is now necessary to create the grid that will be used as a basis for the relationships described above.

4.3.2 Strategy for automatic creation of grids with conductor

4.3.2.1 Sizing of grid

4.3.2.1.1 Transverse size

In the previous section, the choice of the transverse size of the mesh results from a compromise between keeping the number of nodes to a minimum (memory use and calculation speed) and the quality of the solution in the useful zone. The compromise is set at twice the average radius (R_0), the half-size of the grid in TOUTATIS.

4.3.2.1.2 Longitudinal size

The length of the grid is set at $\beta\lambda$.. This choice appears to be the most appropriate in view of the quasi-periodicity of the beam and the structure. However, this choice can result in problems when the bunch is well formed. Very few nodes will then remain for representing macro-particle distribution (Figure 6.11). One solution is to increase the number of nodes [6].. However, this method results in greatly increased calculation time and results in a finer mesh in areas where this is unnecessary. It will be seen that it is advantageous to increase the density of the mesh on the bunch.

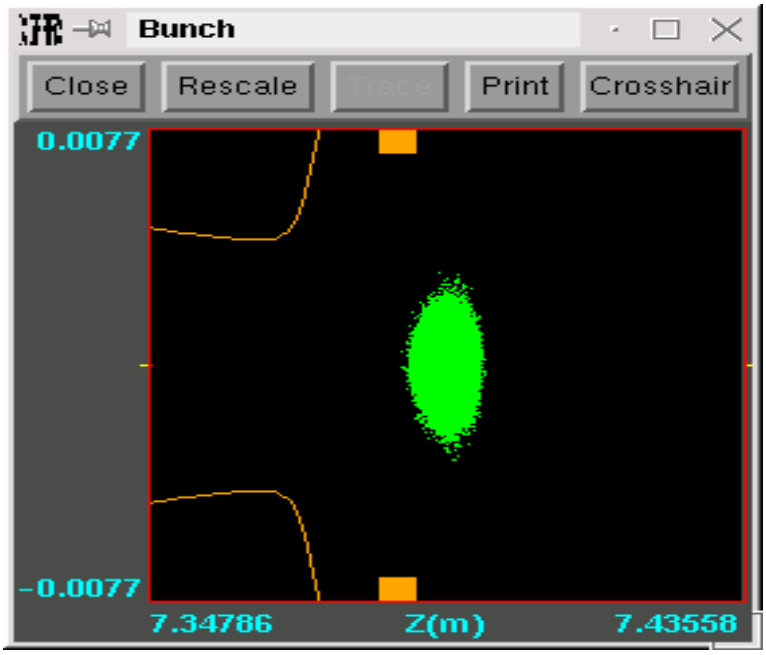

Figure 4.5: Bunch of particles at end of RFQ

4.3.2.2 Discretization of vane geometry

4.3.2.2.1 Assigning parameters to conductor surface

The conductor surface is analytically described by an equation of the $S(x, y, z) = 0$ type. The longitudinal profile of the end of the vane is taken to be sinusoidal, so that the average radius of the cell is given by:

$$R_0(z_0 + \frac{\beta\lambda}{4}) = \frac{1+m}{2}a \tag{4.19}$$

where z_0 is the position of the start of the RFQ cell. For a cell, the longitudinal profile is obtained by applying the following expression:

$$\left\{ \begin{array}{rcl} R_h(z) & = & R_0(z)\left\{1 + \frac{m-1}{m+1}\cos[\frac{2\pi}{\beta\lambda}(z - z_0)]\right\} \\ R_v(z) & = & R_0(z)\left\{1 - \frac{m-1}{m+1}\cos[\frac{2\pi}{\beta\lambda}(z - z_0)]\right\} \end{array} \right. \tag{4.20}$$

where $R_h(z)$ and $R_v(z)$ are the profiles for the horizontal and vertical poles respectively. Function $R_0(z)$ is a linear interpolation between the values of the average radii of successive cells. These average radii have values which are very similar but interpolation is necessary to allow variation of the parameter along the structure while maintaining continuity of the profile of the pole.

The transverse section of each pole in the useful zone is mostly circular (Figure 4.6). This makes them much easier to machine. The circular part is then extended by a flat section at an angle to vertical, the break out angle. This angle can vary as a function of cooling or any other mechanical consideration (it is typically 10*).

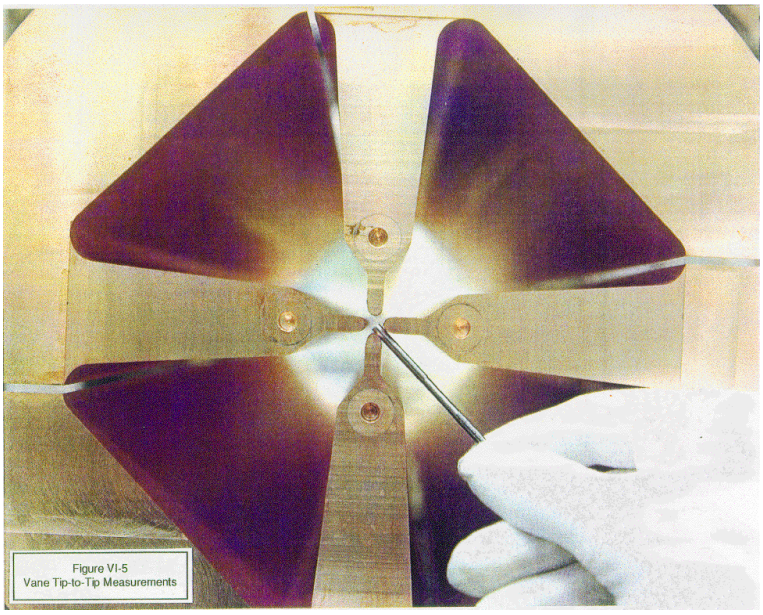

Figure 4.6: Photograph of RFQ transverse section.

The ratio between the average radius R_0 and the pole radius of curvature ρ is generally maintained constant along the structure. This ratio is close to 0.85 and varies with RFQs. The value results from a compromise to minimize non-linearity and peak field amplitude:

$$\frac{\rho}{R_0} = 0.85 \tag{4.21}$$

This relationship determines the variation in ρ as a function of z via $R_0(z)$..

4.3.2.2.2 Finding conductor/grid intersections

The principle consists in scanning axes of reference (*Ox*), (*Oy*) and (*Oz*) and determining the node closest to the surface but outside the conductor. Let us consider Figure 4.7 for scanning along (*Ox*) and (*O*z). The point sought is point 0.. Its indices (i, j, k) are given by the relationships:

$$\left\{ \begin{array}{rcl} i & = & \frac{x_0+\widehat{Y}}{h} \\ j & = & E\left[\frac{f(x_0,z_0)+\widehat{Y}}{h}\right] \\ k & = & \frac{z_0+\frac{\beta\lambda}{2}}{h_z} \end{array} \right. \tag{4.22}$$

where $E[]$ is the integer part operator, h is the transverse pitch of the mesh, h_z is the longitudinal pitch of the mesh, $\widehat{Y}$ is the maximum transverse extent of the mesh, and f is a function derived from the conductor surface equation giving y as a function of x and z. To apply the for-

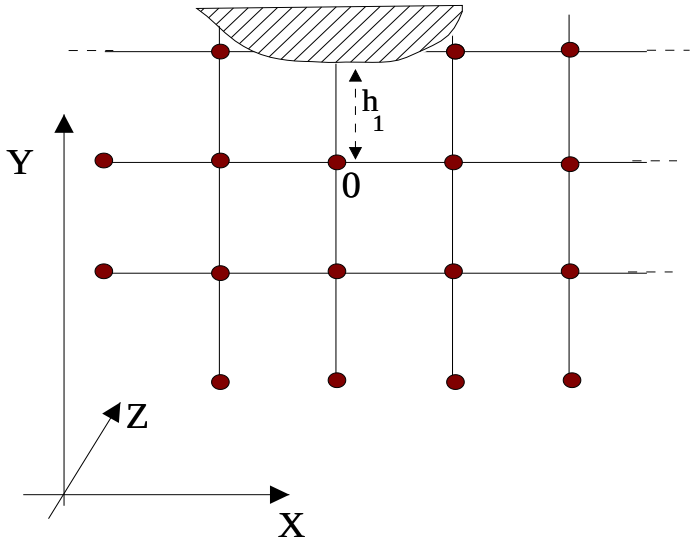

Figure 4.7: Case of finding nodes in the vicinity of conductors.

mulas drawn up for unequal branches, it is necessary to determine the exact distance h_1 (Figure 4.7) between the metal and the node, using the relationship:

$$h_1 = f(x_0, z_0) + \widehat{Y} - j \times h \tag{4.23}$$

When scanning in direction (*Oy*) or (*Oz*), the same method can be applied, taking care to use the correct functions derived from $S(x, y, z)$..

4.3.2.3 Labeling of nodes

Four quantities are assigned to each node of the grid: electrical potential Ψ, charge density per unit volume ρ, residue $\widetilde{\rho}$ and identifier n.. Ψ and ρ are conventional physical quantities at the point represented by the node. Quantity $\widetilde{\rho}$ corresponds to the error remaining after successive iterations during resolution of (4.9). The residue after the ith iteration at node 0 is given by the relationship:

$$\widetilde{\rho_0} = \rho_0 - \frac{4\Psi_0 - \Psi_1 - \Psi_2 - \Psi_3 - \Psi_4}{h^2} \tag{4.24}$$

in accordance with (4.15). This quantity is required for application of multigrid methods and for evaluation of convergence. This point is covered in detail below.

Identifier n is used to indicate the type of node. n is equal to -1 if the node is inside the conductor, potential being imposed. n is equal to 0 for a node with normal branches. Finally n is a positive integer for a node with unequal branches (4.17). The value of n then numbers the node for access to the tables compiling the values of type h_1 in accordance with Section 4.3.2.2.2..

The node labeling stage consists of three phases. First of all, all nodes have labels initialized at 0.. During the conductor/grid intersection search phase, consideration is given to the labels of the nodes with unequal branches. Finally, the nodes inside the conductor are labeled -1.. Once labeling of the nodes is completed, iteration as per the procedures described in Section 4.3.1 can commence.

4.3.3 Multigrid methods

Application of the Gauss-Seidel method, as described in the initial sections, can provide a precise description of the electrical potential in the useful zone of the RFQ. However, calculation time rapidly becomes prohibitive. For instance, a number of days of calculation may be necessary to describe the structure of an RFQ[5].. In an error study involving variation of numerous parameters (beam at entrance, misalignment etc.), the use of a code based on this method obviously requires acceleration of convergence by all possible means. The need for accelerating convergence is not specific to beam transport codes, it has long been a basic requirement of all numerical calculations by relaxation.

Frankel and Young have contributed with a mathematical study of the problem for the simple case of a grid without an encapsulated conductor [5].. They propose multiplying the correction made to Ψ by each iteration at a constant ω, referred to as the *numerical accelerator*.. This method makes it possible to reduce the number of iterations by a factor of 30 or more, depending on the number of nodes involved. Factor ω is calculated analytically as a function of the dimensions $N \times P \times Q \times ...$ of the grid in each direction [5].. When a special conductor geometry is encapsulated in the grid, ω can no longer be calculated analytically. Empirical determination remains possible but can be difficult and time-consuming in terms of calculation time when different geometries need to be considered. In such cases, the best method until the seventies was Chebyshev acceleration [6].. This methods uses the residual of the successive iterations to calculate a suitable accelerator [7], making it possible to achieve performance comparable to that of the Frankel-Young method.

Since the seventies, multigrid methods, introduced by Brandt, have become unavoidable for convergence acceleration [7].. They are used by numerous laboratories and organizations [8, 9, 10].. However, there is not one multigrid method but many, and it is up to the analyst to adapt the basic concepts of these methods to the problem in hand.

4.3.3.1 Basic concepts

There are two key concepts in multigrid methods. The first is seeking to evaluate error in Ψ by successive iterations rather than correcting Ψ by small increments. The search for error is made by relaxation. The second concept is achieving relaxation not in a mesh of the same type but in a coarser of mesh (larger elements). Error evaluation is far quicker, if not virtually instantaneous. To go into details, let us consider that it is required to solve the equation:

[5]For a N^3 mesh where N=65, with a 600-cell structure calculated using an HP-J282 workstation.

$$\Delta\Psi = \rho \tag{4.25}$$

where Δ is a linear operator and ρ represents the sources. By discretizing (4.25) in a uniform grid with a pitch of h, the problem is reduced to a set of equations of the following type:

$$\Delta_h\Psi_h = \rho_h \tag{4.26}$$

During the first iteration, using the Gauss-Seidel method[6], an approximation of Ψ_h is obtained. Note the $\widetilde{\Psi}_h$.. The error then equates to:

$$\xi_h = \Psi_h - \widetilde{\Psi}_h \tag{4.27}$$

The residual, or deficit relative to the sources, is:

$$\delta_h = \Delta_h\widetilde{\Psi}_h - \rho_h \tag{4.28}$$

As Δ_h is linear, the error satisfies the equation:

$$\Delta_h\xi_h = -\delta_h \tag{4.29}$$

The problem therefore consists in finding ξ_h (i.e. the error) in order to correct $\widetilde{\Psi}_h$ and thus obtain Ψ_h.. Using Δ_h would not result in any calculation time being gained. It is preferable to use a coarser grid with a pitch of $H = 2h$.. Equation (4.29) then becomes:

$$\Delta_H\xi_H = -\delta_H \tag{4.30}$$

As Δ_H contains less nodes than Δ_h (8 times less in the three-dimensional case), (4.30) is quicker to solve. For determining ξ_H, it is necessary to obtain δ_H via a new operator referred to as a *restrictor*:

$$\delta_H = \Re\delta_h \tag{4.31}$$

This operator is also referred to as an injection operator. It makes it possible to switch from a *fine* grid to a *coarse* grid. Once ξ_H is calculated, it is also necessary to have an additional operator making it possible to obtain ξ_h:

$$\xi_h = \wp\xi_H \tag{4.32}$$

This operator is also referred to as an *extender*.. It uses interpolations in the coarse grid to calculate the corresponding values in the fine grid. The restrictor and extender operators enable communication between the two levels. They have no separate existence, and must be generated for the problem in hand.

[6] it is, in fact, preferable to carry out at least three.

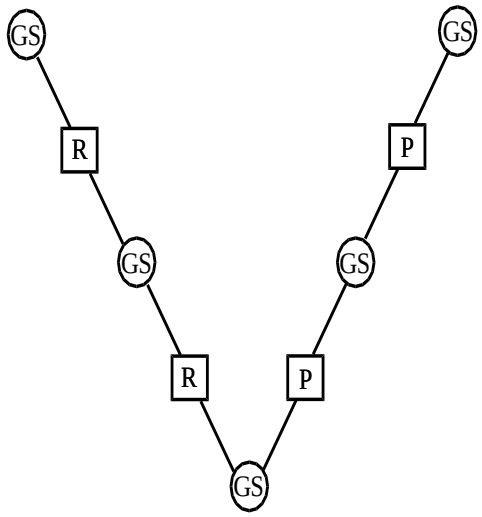

Figure 4.8: A V-shaped cycle .

Finally, all that now remains is to correct Ψ_h:

$$\tilde{\Psi}_h^{i+1} = \tilde{\Psi}_h^i + \xi_h \tag{4.33}$$

The procedure must be repeated to obtain the desired degree of convergence. The approach can be combined at a number of levels. Each grid, of increasing coarseness, is used to estimate the error of the next one. The combinations or cycles are multiple. The analyst has to test a number of types of cycles to obtain an optimized algorithm.

Another trick for accelerating convergence consists in storing the solutions obtained for an RF period. These can therefore be used as a preliminary solution for calculating the following period. The number of cycles necessary is thus reduced by a factor of approximately $4.$. Details are given of some of the commonest cycles, such as that used in the TOUTATIS code.

4.3.3.2 Main cycles

4.3.3.2.1 V-shaped cycle

Figure 4.8 shows the principle of the V-shaped cycle. The stages marked *GS* are where three Gauss-Seidel type iterations are made. *R* represents a restriction and *P* an extension. V-shaped cycles can be carried out in succession to obtain the desired reduction in the residual in the finest grid.

4.3.3.2.2 W-shaped cycle

The principle of this type of cycle is shown in Figure 4.9.. In some cases, it can be used to obtain the solution with a minimum number of iterations on the finest grid, when it becomes a

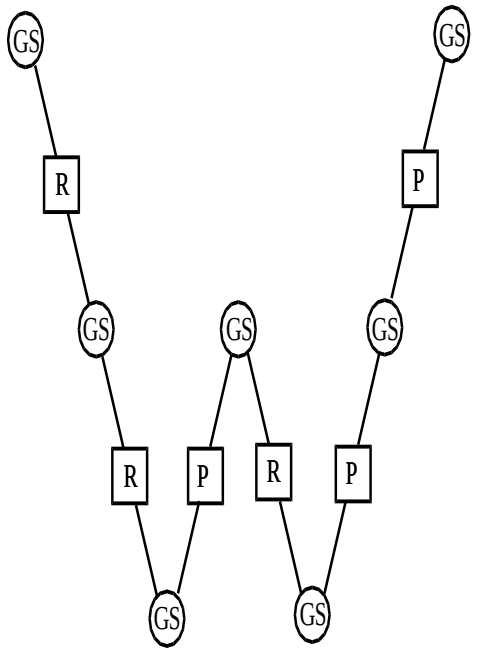

Figure 4.9: A W-shaped cycle.

useful alternative to the conventional V-shaped cycle.

4.3.3.2.3 Total cycle (*Full Algorithm Multigrid)*

Another way of minimizing the number of transitions to finer grids[7], is the total cycle which, in many cases, is the most effective way of using the basic concepts given in Section 4.3.3.1.. Up to now, an intermediate solution on the finest grid was used as the starting point, and the error was estimated on grids of increasing coarseness in succession. In the full algorithm multigrid system, the terms of sources ρ are known at all levels. Either ρ has been discretized on each grid, or ρ_h has been restricted in sequence. The process then begins at the lowest level (Figures 4.10 and 4.11). Then the solution is extended to the upper level. The latter is calculated by a V-shaped cycle, and so on until the final level is reached.

4.3.3.2.4 The cycle used in TOUTATIS

The cycle is a combination of the preceding ones. It uses the principle of the total cycle without having to know the sources at all the levels. This makes calculation time 20 to 30% shorter than with V- and W-shaped cycles, with the code. It is shown in Figure 4.12..

4.3.3.2.5 Restriction and extension operators

These operators, which are used for communication between levels, are extremely important. The effectiveness of the multigrid process depends directly on their quality. In the case of a

[7] requiring longer calculation time.

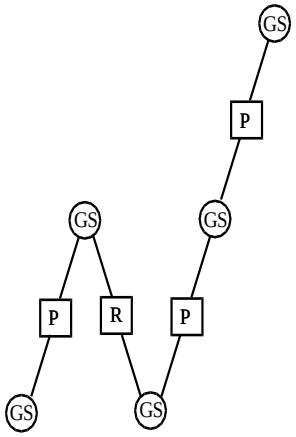

Figure 4.10: A total cycle.

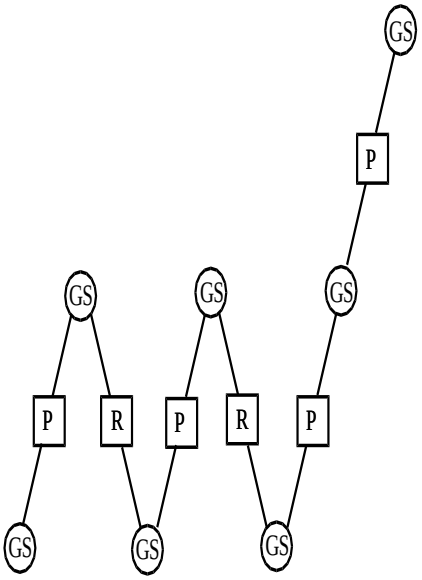

Figure 4.11: Another total cycle.

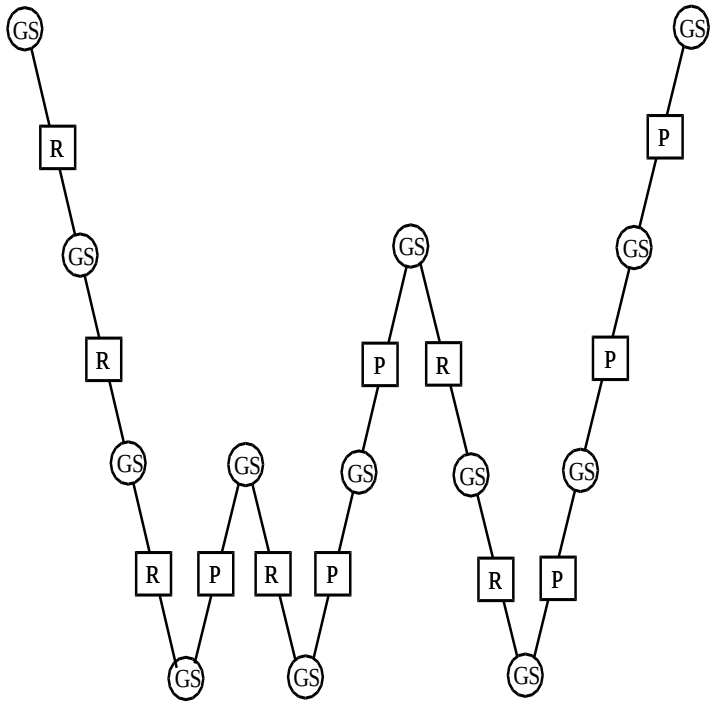

Figure 4.12: The cycle used in TOUTATIS.

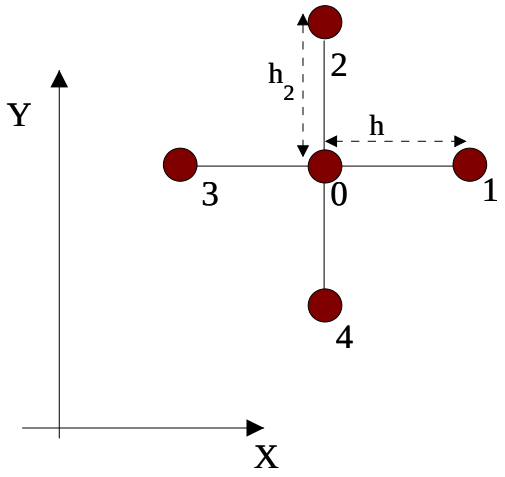

Figure 4.13: Configuration with $h_2 < h$..

grid without encapsulated conductors, the potential is continuous inside the domain with the result that the most commonly used extender is straightforward linear interpolation with constant coefficients. In other words, the values at the common points of the two grids are retained. For the intermediate points of the fine grid, the values are averages calculated using nearby points that have already been initialized. For restriction, the values at the common points of the two grids are retained. This is referred to as *direct injection*..

When the discontinuities in potential make the use of unequal branches necessary, the extender interpolation coefficients must be different, depending on the node in question. In TOUTATIS, the correction values are weighted with allowance for the actual distances between the node with unequal branches and the discontinuity. The closer the node to the conducting surface, the smaller the error.

In Figure 4.13, node 2 is on the conductor in a transverse plane common to the coarse and fine grids. It is desired to calculate error ξ_0 on node 0, knowing errors $\xi_{1,3,4}$ at nodes 1, 3 and 4, the error at node 2 being nil (imposed potential). The values for 1 and 3 are obtained by direct injection of the coarse grid. The value for node 4 is obtained by calculating the average of the errors obtained by direct injection of the nodes neighboring 4 and at a distance of $\sqrt{2}h$, such as nodes 1 and 3. The error on node 0 is obtained with the following expression:

$$\xi_0 = \frac{1}{2}\left[\frac{1}{2}\left(\xi_1 + \xi_3\right) + \frac{h_2}{h_2 + h}\xi_4\right] \tag{4.34}$$

If node 3 is also on the conductor at a distance $h_3 < h$ from node 0, expression (4.34) then becomes:

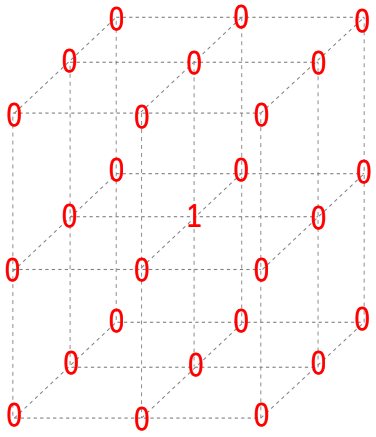

Figure 4.14: Representation of direct injection for restriction as a matrix. The central node is an element of the coarse grid. All the nodes are elements of the fine grid.

$$\xi_0 = \frac{1}{2}\left[\frac{h_3}{h_3+h}\xi_1 + \frac{h_2}{h_2+h}\xi_4\right] \tag{4.35}$$

All the nodes on the plane can thus be calculated. The intermediate planes of the fine grid are finally obtained by simply interpolating between two planes constituted by the method described above.

It is this algorithm that TOUTATIS uses for the cycle shown in Section 4.3.3.2.4.. Section 4.3.5 describes in detail a refinement using a second grid giving a better description of the charge distribution. The second grid, which has no encapsulated conductor, is calculated by means of a V-shaped cycle (Section 4.3.3.2.1). For this cycle, the extender uses the same principles. The relationships of the (4.34) and (4.35) types are simplified as there is no discontinuity of potential in the grid. For the restrictor, there is a more effective operator than the direct injection described in the literature [7].. To represent it, matrix formalism is used. Having three dimensions, the matrix is $3 \times 3 \times 3$.. To understand the basic idea, the direct injection used in the cycle (Section 4.3.3.2.4) is schematically shown in Figure 4.14.. The restrictor used in the V-shaped cycle is shown in Figure 4.15..

When applied in the vicinity of the common node, this matrix gives the same degree of convergence with a smaller number of cycles. It is to be noted that, unlike the cycle restrictor (Section 4.3.3.2.4), this one involves the neighboring nodes of the fine grid. Cycle restriction (Section 4.3.3.2.4) could probably be improved by creating matrices of more complex functions of values $h_i < h$.. This remains to be done.

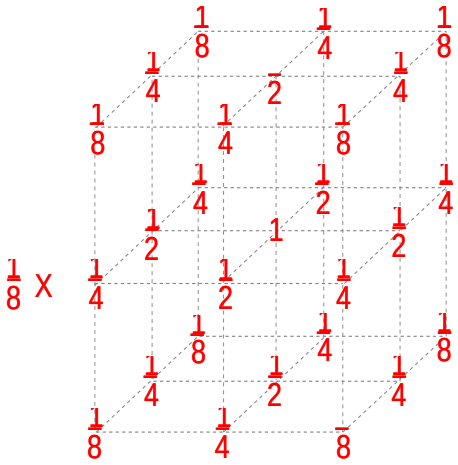

Figure 4.15: Representation of V-shaped cycle restrictor in matrix form.

4.3.4 Convergence

The preceding sections indicate on numerous occasions that the relaxation process must be repeated until adequate reduction of the residual is obtained. This implies laying down one or more criteria for estimating the quality of the solution obtained after each cycle. It is also necessary to test convergence of the process during relaxation to ensure that the numerical system is robust.

4.3.4.1 Estimation of convergence

In multigrid cycles, the geometry of the RFQ must be discretized on all the grids, from the finest to the coarsest. The quality of the extension and/or restriction operators can result in unsatisfactory transfer of data between the levels. This becomes particularly critical when the geometry of the structure becomes complex (end with plate and coupling gap). The “low” levels of the multigrid cycles can be too coarse or poorly initialized to obtain a good estimate of the error of the upper level. It is therefore required to withdraw the level from the cycle to avoid compromising the quality of calculation, even if this means reducing the effectiveness of the method. It is then necessary to define a quantity which can be used as an “anti-divergence alarm”.. In the TOUTATIS code, the norm of the residual is used for this purpose:

$$\aleph = \sum \delta^2 \tag{4.36}$$

which is the sum of the square of the residual of each node in the net. This quantity should diminish if the process converges. Otherwise, the coarsest grid is withdrawn from the cycle at

the expense of finally relaxing only the finest mesh.

4.3.4.2 Quality criterion

When the norm of the residual, ℵ, diminishes, it is necessary to introduce another criterion used for determining whether the "solution" has been found. The word "solution" is in quotes because the true solution is only reached when $h \to 0$, which, of course, cannot be achieved in practice (i.e. $\aleph = 0$). In some computer codes using a multigrid cycle, the authors set a maximum value for ℵ.. This is based on the assumption that it includes a safety margin for a relatively wide range of cases[8].. This margin can therefore be penalizing in terms of calculation time. Another more dynamic criterion is application of the Laplacian operator after each cycle and stopping the calculation when the number of particles found corresponds to that imposed for each node within tolerance limits. Given that the initial distribution of charge is itself affected by error due to firing ($N \pm \sqrt{N}$), the tolerance limit to be applied is easy to determine. It is simply a matter of allowing the same error at each node. The calculation is stopped at cycle j when, for each node, i:

$$N_i - \sqrt{N_i} \leq N_i^j \leq N_i + \sqrt{N_i} \tag{4.37}$$

In nodes where the number of macro-particles is small, the approximation remains acceptable (one particle more or one particle less for nodes with none, for instance).

4.3.5 Adaptive meshing

When the bunches of particles have a small longitudinal extension relative to $\beta\lambda$, resolution of the grid, for describing distribution, becomes poor (see Section 4.3.2.1.2). This degradation can also occur transversally when the cross-section of the beam is small compared to the radius of the average groove in the poles (i.e. R_0). A good solution is to use another grid encapsulated in the main grid. This second grid has dimensions that are functions of the dimensions of the bunch in the three directions[9].. Figure 4.16 illustrates the respective grid geometries.

The method consists of a number of stages. The main grid is first calculated independently of the second meshing. Once the convergence criterion has been met, the adaptive meshing is initialized by interpolation in the main grid. As for the main grid, initialization makes it possible to achieve convergence more rapidly. As the charges were initially discretized at the nodes of the net, the relaxation process is begun using V-shaped cycles. This type is more effective in such a structure without a conductor, with the potential imposed at the transverse surfaces. For the longitudinal surfaces, the boundary conditions are identical to those of the main grid as long as $3.5 \times Z_{rms} > 60\% \times L_c$, where L_c is the length of the cell. The quantity Z_{rms} is determined with the expression:

[8] Number of macro-particles for example.

[9] These are the RMS dimensions, which are used to provide freedom from any statistical fluctuations. The limits are set at 3.5 Z_{rms} and 4 X_{rms} for the half sizes of the mesh in each direction (for the transverse direction, it is the larger of the values, X_{rms} and Y_{rms}, which is selected).

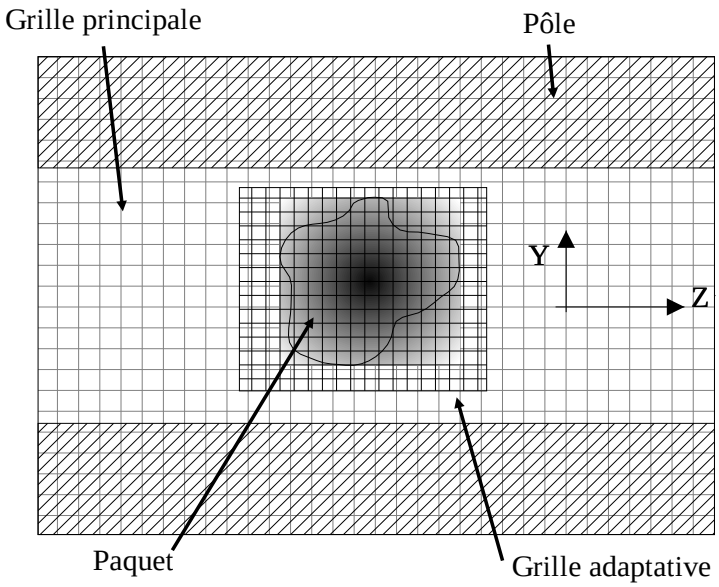

Figure 4.16: Sectional view showing adaptive grid encapsulated in main grid.

$$Z_{rms} = \sqrt{\overline{(z - z_c)^2} - \overline{(z - z_c)}^2} \tag{4.38}$$

where z_c is the centroid of the beam and $\overline{x}$ the average of quantity x over the distribution. When this condition is no longer met, a Dirichlet condition is imposed on the surfaces (potential given by large grid). This value of 3.5 is a compromise between the desire not to reduce the resolution of the net over the distribution and not to substantially influence the final solution with the Dirichlet condition. Another possible method would have been nesting of the two grids during the process of calculation of the main one, with the latter communicating their intermediate solution between each cycle. This communication would make this method slower and would probably converge towards the same solution, as long as the value of 3.5 was not not too greatly diminished.

4.3.6 Test with cylindrical Gaussian distribution

The usual procedure when writing a program solving the Poisson equation is to test it with a reference distribution, and we have done so using a cylindrical Gaussian distribution, corresponding to the expression:

$$\rho(r) = Q \exp(-\frac{r^2}{2\sigma^2}) \tag{4.39}$$

with:

$$Q = \frac{-I}{2\pi\sigma^2\varepsilon_0\beta c} \tag{4.40}$$

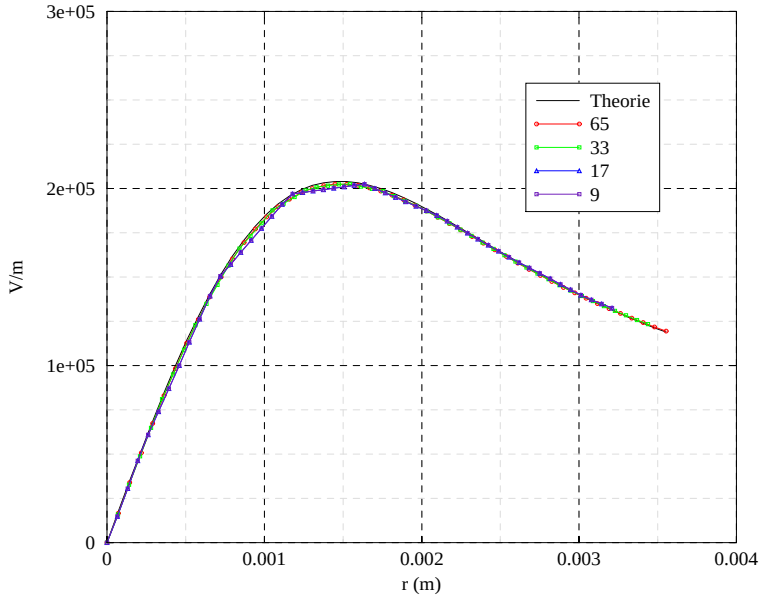

Figure 4.17: Different radial electrical field profiles for different adaptive grid densities relative to the theoretical profile.

where I is the current (100 mA), σ the Gaussian standard deviation (0.934 mm), c the speed of light, β the relativistic factor (0.014229 for 95 keV protons), and ε_0 the permittivity of vacuum. $\rho(r)$ is homogenous at a charge density per unit volume divided by ε_0.. The field produced by this charge distribution is as follows:

$$E_r = -Q\sigma^2 \frac{1 - \exp(-\frac{r^2}{2\sigma^2})}{r} \tag{4.41}$$

Figures 4.17 and 4.18 show the radial electrical field profile given by theory (in black) and the profiles obtained for the different adaptive grid finesses (65 means that there are $65 \times 65 \times 65$ nodes in the finest grid). The difference between the maximum theoretical value and that given in the 33 and 65 cases is less than 0.7%.

4.4 Loss management

4.4.1 Transverse losses

The criterion is simple. A particle is declared to be lost when its trajectory brings into contact with the poles. Allowance must therefore be made for pole geometry at each increment of the trajectory of each particle. To avoid unnecessarily complicated processing, and thus optimize calculation time, for a given particle, allowance is only made for pole geometry if the particle is outside the square $2a$ of a side.

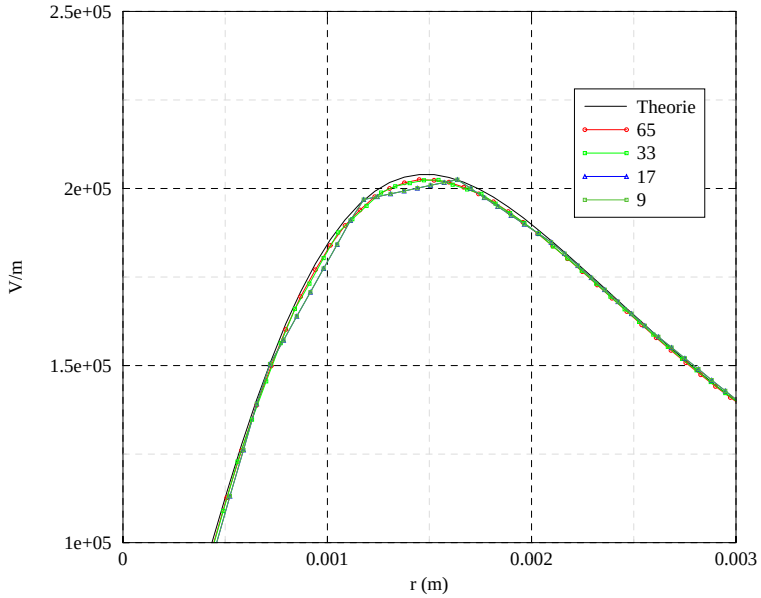

Figure 4.18: Focus on maximum values.

4.4.2 Phase offset particles

When the velocity of the particle is sufficiently different from the synchronous velocity, the window of width $\beta\lambda$ centered on the centroid is no longer large enough to contain all the particles. When an offset particle is early, its transport is suspended for one RF period, the time taken for the bunch to become the preceding bunch. It can then be determined what became of a particle when it entered the following bunch. This case is relatively rare. The case of particle delay is more common. The processing is basically similar. TOUTATIS stores the fields for one period for initialization of the numerical calculations, and therefore transport of a late particle into the next bunch has been implemented.

4.5 Conclusion of chapter

The TOUTATIS transport code was written with a view to obtaining better accuracy while minimizing approximations in simulation of the dynamics of an intense beam in an RFQ. This chapter describes the numerical methods used to finalize the computer code. The basic principles (finite differences and multigrid grid) are described. A suitable strategy for discretization of the RFQ electrode geometry is discussed. A number of refinements such as adapter meshing and storage of intermediate solutions are used to improve the performance of the code.

Unlike PARMTEQM, this code does not assume paraxiality, but calculates the self-consistent forces of the beam for each time increment, and the potential due to geometry is calculated numerically with allowance for the exact shape of the poles.

Bibliography

[1] Private communication by J.-M. Lagniel.

[2] Lloyd Young, “Segmented Resonant Coupled Radio Frequency Quadrupole (RFQ)”, Proceedings of the 1993 Particle Accelerator Conference, Washington, D.C.

[3] Romuald Duperrier et al., “Study of Coupling Gap Effects on Beam Dynamics in Favor of RFQ I.P.H.I. Design”, CEA/DSM/DAPNIA/SEA/IPHI 2000/07.

[4] R. Duperrier et al.“Field Description in an RFQ and its Effect on Beam Dynamics”, M04029, Proceedings Linac 98.

[5] E. Durand, “Electrostatique, Volume III, Méthodes de Calcul, Diélectriques”, Masson & C^{ie}, Editor, 1966.

[6] B. Bondarev, A. Durkin, S.V. Vinogradov, “Multilevel Codes RFQ.3L For RFQ Designing”, IFMIF Accelerator Team Paris Meeting, CDE Workshop, 26-30 May 1997.

[7] William H. Press, Saul A. Teukollsky, William T. Vetterling, Brian P. Flannery, “Numerical Recipes, The Art of Scientific Computing”, Second edition, Cambridge University Press, 1992.

[8] Marcus S. Day, Philip Colella, Micheal J. Lijewski, Charles A. Rendleman, “Embedded Boundary Algorithms for Solving the Poisson Equation on Complex Domains”, Lawrence Berkeley National Laboratory, Office of Energy Research, Applied Mathematical Sciences Program.

[9] L. Adams, “A multigrid algorithm for immersed interface problems”, Seventh Copper Mountain Conference on Multigrids Methods, NASA Conference Publication 3339, NASA, p. 1-14 (1996).

[10] P. Pierini, “A multigrid approach to modeling a high current superconducting linac for waste transmutation”, ICAP 1998 conference, 14-18 September, Monterey.

Chapter 5

Validity and comparison of methods

Chapter 3 covered the main hypotheses and approximations used in PARMTEQM for simulating transport in an RFQ. In this chapter, an attempt is made to quantify the errors induced by these approximations and to determine their relative importance. This is achieved by either modifications to the PARMTEQM code itself or simulation using the TOUTATIS code and the TOSCA electrostatic calculation modulus [1].

5.1 Calculation of external fields

Chapter 3 describes the different approaches used for each part of the RFQ in PARMTEQM. The following sections are concerned with the ability of these approaches to describe the potential.

5.1.1 RFQ body

The PARMTEQM code is based on the eight-term multipolar approach detailed in Section 2.3 [2,3]. Appendix A describes the various methods used to calculate the series coefficients. In this section, consideration is given to means of determining the bounds of validity of this approach in the useful zone by means of two methods: projection and fitting to the geometry of the poles.

5.1.1.1 Calculation of a reference with the Vector Fields TOSCA module

To use the projection method, a reference potential is required. The electrostatic potential of a test cell was therefore calculated with the TOSCA code[1].. Figure 5.1 represents the distribution of potential obtained for a cell with the characteristics indicated in Table 5.1..

This simulation is also used as a reference for estimating the quality of the multipolar approach obtained with the different methods. The section on the peak fields covers the techniques used to make the simulation in greater depth.

[1]Note that for PARMTEQM, the calculations were made with CHARGE 3D [3]..

Parameters	Value or type
Radius of curvature of pole ρ_t/R_0	0.89
Length L_c/R_0	11
Modulation factor m	2
Longitudinal profile	sinusoidal
Minimum gap, a	2/(1+m)

Table 5.1: Characteristics of test cell.

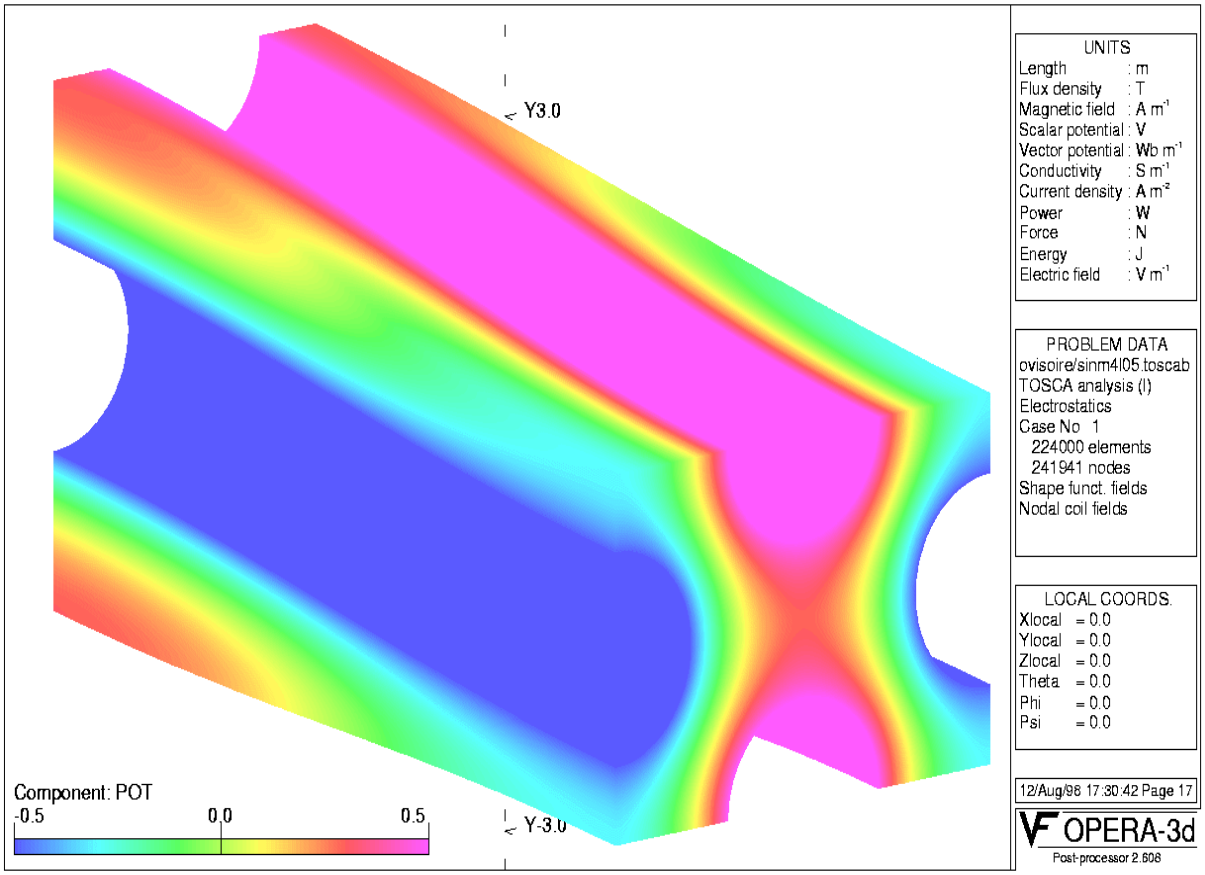

Figure 5.1: Distribution of electrostatic potential in the test cell as calculated with TOSCA.

A_{01}	A_{03}	A_{10}	A_{12}	A_{21}	A_{23}	A_{30}	A_{32}
0.9267	0.00112	0.6006	307.6125	-0.8337	-30753.6794	-0.0109	-7.0949

Table 5.2: Coefficients obtained by projection.

5.1.1.2 Projection

To use this method, it is necessary to limit the domain of integration to the surface of a cylinder of radius a and length L_c.. In view of the quadrupolar symmetry, it is possible to take only one quarter of the surface. The formulae used for the calculation are the following:

$$A_{0m} = \frac{16}{\pi V a^{2m} L_c} \int_0^{\frac{\pi}{2}} \int_0^{L_c} U(a,\theta,z) \cdot \cos(2m\theta) d\theta dz \tag{5.1}$$

$$A_{n0} = \frac{8}{\pi V I_0(nka) L_c} \int_0^{\frac{\pi}{2}} \int_0^{L_c} U(a,\theta,z) \cdot \cos(nkz) d\theta dz \tag{5.2}$$

$$A_{nm} = \frac{16}{\pi V I_{2m}(nka) L_c} \int_0^{\frac{\pi}{2}} \int_0^{L_c} U(a,\theta,z) \cdot \cos(2m\theta) \cdot \cos(nkz) d\theta dz \tag{5.3}$$

where U is the numerical reference. The results obtained for each coefficient are summarized in Table 5.2.. To assess the relative weights of each component, the values are given in Table 5.3 multiplied by their associated radial functions in R_0, the average radius (Bessel function or r^n). Convergence would appear to be rapid, with high order terms making little contribution, particularly near the axis.

Figure 5.2 shows the relative difference between the potential calculated with TOSCA and the series obtained by projection. The scale is logarithmic in order to be able to show the entire useful zone. The two lines at 100% correspond to the numerical noise on the “zero” equipotentials. The black circle describes the cylinder used for integration. It is clearly apparent from these maps that the high-quality solution inside the cylinder cannot be extrapolated beyond it (<1% inside, more than 10% outside). In addition, if it is required to obtain an accuracy greater than 1% *throughout* the useful zone, it must be accepted that the projection approach is inadequate, which was confirmed by Ken Crandall himself during a visit to Saclay. The approach is, however, completely satisfactory as long as the particles remain inside the cylinder.

5.1.1.3 Geometrical fit

The quadruplets of values of the (x_i, y_i, z_i, U_i) type necessary for using this method are taken on the surface defined by the vane geometry. Values U_i then appear. Calculation is made with the Mathematica application. The results obtained for each coefficient are summarized in Table 5.4.. Table 5.5 gives these values multiplied by their associated radial functions in R_0.. It is to be noted that the octupolar component was multiplied by 10. This has a direct effect on beam distribution: the transverse profile increasingly tends to become lozenge-shaped. This particular profile induces uncertainty as to the PARMTEQM space charge calculations (SCHEFF sub-program) which assumes that the beam has symmetry of revolution.

Coefficient×function in R_0	Value
$A_{01}R_0^2$	0.9267
$A_{03}R_0^6$	0.0012
$A_{10}I_0(kR_0)$	0.6129
$A_{12}I_4(kR_0)$	0.0054
$A_{21}I_6(2kR_0)$	-0.0349
$A_{23}I_6(2kR_0)$	-0.0235
$A_{30}I_0(3kR_0)$	-0.0130
$A_{32}I_4(3kR_0)$	-0.0103

Table 5.3: Coefficients obtained by weighted projection by their associated radial functions in R_0..

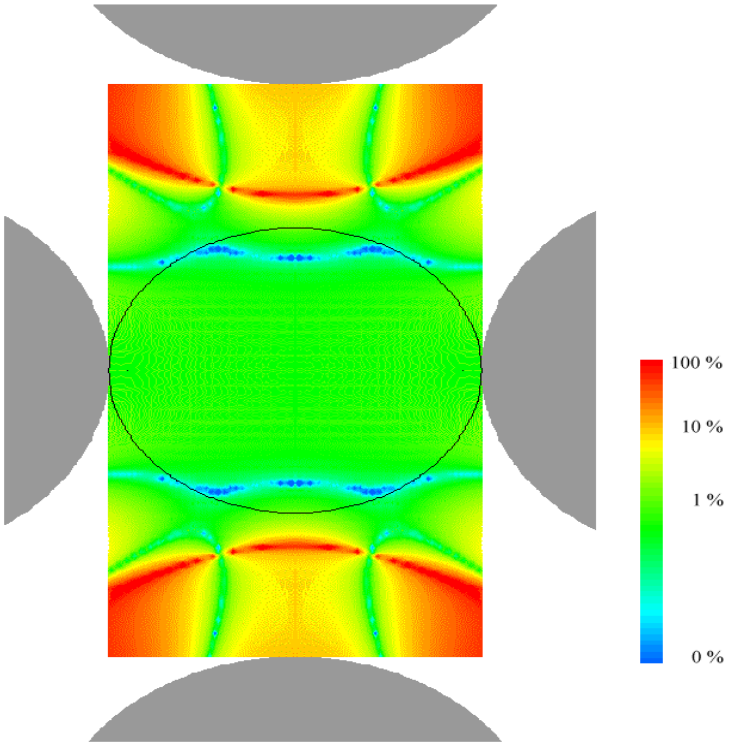

Figure 5.2: Relative difference between numerical potential and the series obtained by projection with a logarithmic scale.

A_{01}	A_{03}	A_{10}	A_{12}	A_{21}	A_{23}	A_{30}	A_{32}
0.9587	0.0211	0.6064	3489.5500	-0.5960	3493.3200	-0.0093	-4.1060

Table 5.4: Coefficients obtained by geometrical fit.

Coefficient×function in R_0	Value
$A_{01}R_0^2$	0.9587
$A_{03}R_0^6$	0.0211
$A_{10}I_0(kR_0)$	0.6188
$A_{12}I_4(kR_0)$	0.0613
$A_{21}I_6(2kR_0)$	-0.0249
$A_{23}I_6(2kR_0)$	0.0027
$A_{30}I_0(3kR_0)$	-0.0111
$A_{32}I_4(3kR_0)$	-0.0059

Table 5.5: Coefficients obtained by weighted fit by their associated radial functions in R_0..

Parameter	Value or type
distribution	4D Water Bag
$\varepsilon_{r.m.s.,norm.}$ at entrance	0.4 π..mm.mrad
entrance current	225 mA
particles	protons
kinetic energy at entrance	90 keV
kinetic energy at exit	5 MeV
frequency	202.56 MHz
constant voltage	178 kV
constant R_0	8.203 mm
constant ρ_t/R_0	0.85
maximum m	2.05

Table 5.6: Main parameters of simulated RFQ.

Figure 5.4 shows the relative differences between the potential calculated with TOSCA and the series obtained by geometrical fit. The accuracy is of a few percent in the useful zone. However, it exceeds 1% in the central zone. As expected, the multipoles predominate at a distance from the axis.

5.1.1.4 Consequences for particle dynamics

It is not possible to draw valid conclusions, for the entire RFQ, concerning the consequences for particle dynamics when using any one of these methods. It is, however, interesting to note the differences for a given RFQ and to review the trends. The RFQ used is a modified version of RFQ2 at CERN. The modification resides in elongation of the structure, the final energy being increased to 5 MeV from the initial 750 keV. Table 5.6 summarizes the main parameters of this RFQ. Transport was calculated with TOUTATIS in every case. The external potential is either calculated or the result of development.

Tables 5.7 and 5.8, which give the rms emittances normalized for each plane and the RFQ exit transmission for each method, shows that the fit does not allow reasonable estimation of the

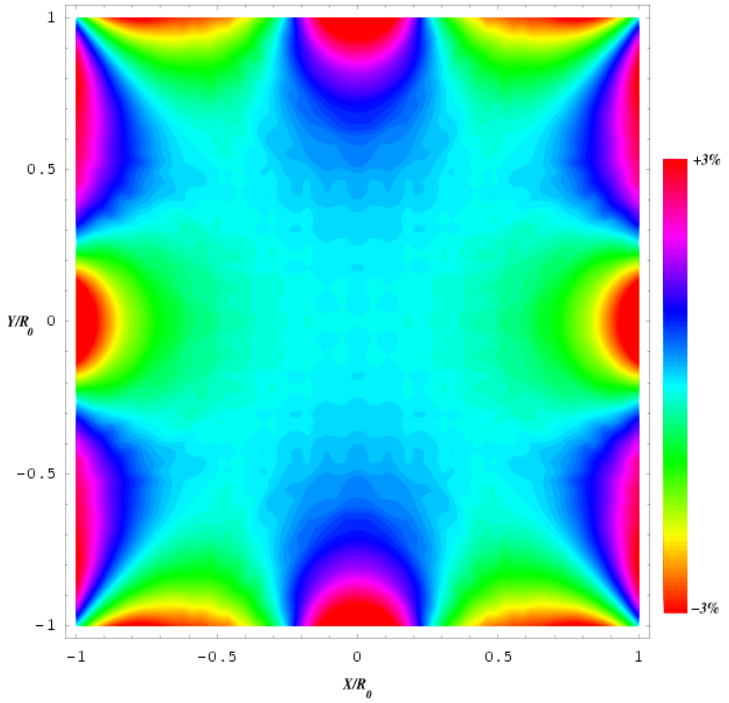

Figure 5.3: Map of the error obtained by fit in the transverse plane at the center of the cell (linear scale).

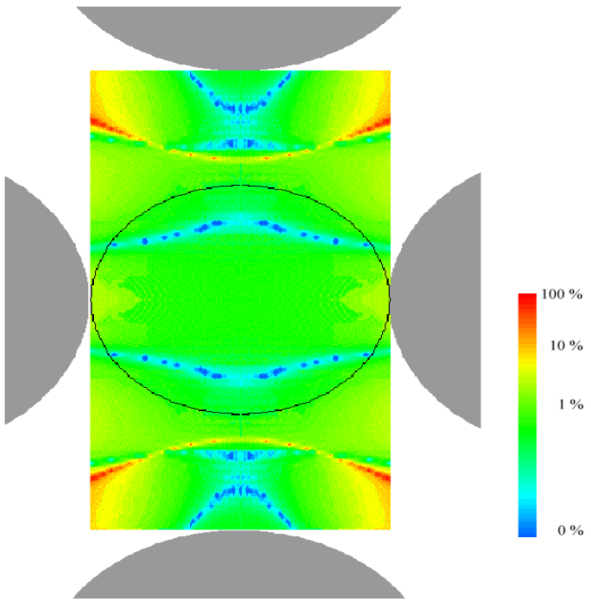

Figure 5.4: Relative difference between numerical potential and the series obtained by fit (logarithmic scale).

	$\widetilde{\varepsilon}_{x,n.}$($\pi$..mm.mrad)	$\widetilde{\varepsilon}_{y,n.}$($\pi$..mm.mrad)	$\widetilde{\varepsilon}_{z,n.}$(deg.MeV)
True field	0.584	0.597	0.202
Projection	0.598	0.612	0.206
Fit	0.518	0.540	0.196

Table 5.7: rms emittances normalized for each plane at the RFQ exit with different methods.

	Yield	Transmission	Yield Variation	Total loss variation
True field	96.2%	97.9%	0.%	0.%
Projection	95.4%	97.3%	- 0.9%	+ 31.7%
Fit	90.9%	95.0%	- 5.5%	+ 139.4%

Table 5.8: Yield and transmission with each method. The first case is the reference for variation calculation. The yield is transmission with allowance for accelerated particles only.

fields in the structure. The average error is around 10% in the transverse plane. The projection method is generally in good agreement. However, it should be noted that there is a variation of more than 30% in the predicted losses with this method.

5.1.1.5 Conclusion

Projection is the method which gives the greatest accuracy in the zone occupied by the beam core. The development obtained cannot accurately describe the potential applied to the particles making up the halo. The suitability of the method depends on the tolerance limits set. It is to be noted that there is no guarantee that the differences would be the same with a different RFQ. Although geometrical fit gives better results in the halo zone, the quality of the results is inadequate in terms of the minimum tolerance limits for linear accelerators (maximum error <1%).

It is impossible to fully simulate the useful zone of an RFQ because cylindrical coordinates are used. The four poles are not asymptotic for obtaining high-voltage resistance of the structure [2,4], their transverse radius of curvature is maintained constant along the cell whereas the distance between the axis and the pole can vary by a factor of 2. The cylindrical harmonics do not possess these properties. The introduction of higher order multipoles gives rise to the appearance of other $\pm V/2$ equipotentials leading to geometries such that the poles cannot be machined (Figure 5.5).

To avoid these imperfections by analytical means, while retaining the geometrical properties imposed at the poles, it is necessary to have a system of coordinates with harmonic developments giving longitudinal periodicity while retaining the transverse curvature of the equipotential surfaces. This means that there is no transverse-longitudinal coupling in the harmonics. However, when it is required to isolate the periodic harmonics in one direction during resolution of the Laplace equation, such coupling arises in almost every case. Even if it is accepted that such harmonics exist, the introduction of discontinuity into the structure (radiofrequency coupling gaps etc.), means that only one numerical simulation will be satisfactory. The use of such numerical

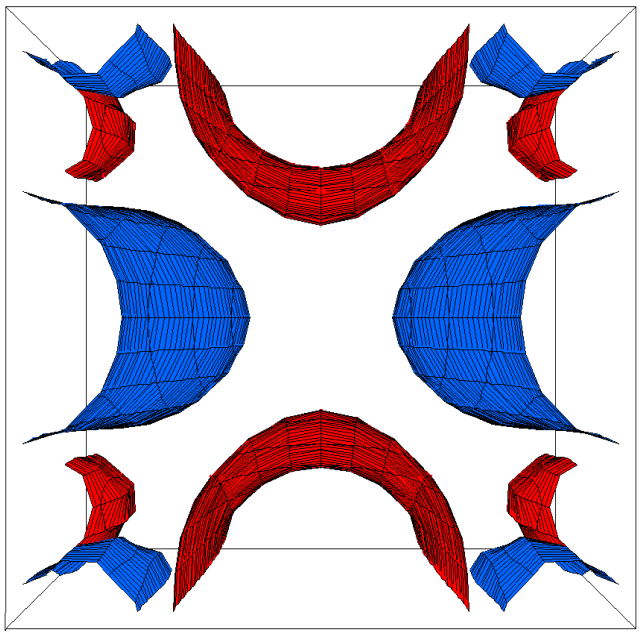

Figure 5.5: $\pm V/2$ equipotential surfaces obtained by geometrical fit.

simulation is now possible as a result of improved computer performance.

5.1.2 Radial matching section at entrance

Chapter 2 showed that it was necessary to introduce a radial matching section at the RFQ entrance. In Chapter 3, the formulation used in PARMTEQM for describing this portion of the RFQ was explained. Consideration is now given to quantifying the performance that can be expected from the formulation and testing of other options.

5.1.2.1 Section optimization method

Let us briefly consider the method used for optimizing the matching section. The RFQ designer must first determine the Twiss parameters[2] needed to optimize matching for the Focusing-Defocusing (FD) channel which makes up the first part of the RFQ. The FD channel is accurately described by the following formula:

$$\Psi(\rho,\theta,t) = \frac{V}{2}\left[A_{01}\left(\frac{\rho}{R_0}\right)^2\cos(2\theta) + A_{03}\left(\frac{\rho}{R_0}\right)^6\cos(6\theta)\right]\sin(\omega_{rf}t+\varphi_{rf}) \qquad (5.4)$$

[2]These parameters are α, β, γ.. They satisfy the relationships: $X=\sqrt{\beta\varepsilon}$, $X'=\sqrt{\gamma\varepsilon}$, $\beta\gamma-\alpha^2=1$.. X is the transverse size of the beam, X' its divergence and ε its geometrical emittance.

where R_0 is the gap, V is the difference in potential between the vanes, and A_{01} and A_{03} are the quadrupolar and dodecapolar coefficients respectively. These coefficients only depend on ρ_t/R_0 where ρ_t is the transverse radius of curvature of the pole.

Once the FD channel is determined, suitable Twiss parameters for the channel are established using a minimization process. The designer then assumes that transport in this section of the RFQ is reversible. This is equivalent to stating that variations in emittance are sufficiently small to be disregarded. The beam matched to the FD channel is then transported from the end of the entrance section to the beginning. This stage is repeated for the different radiofrequency phases at the entrance to the FD channel. The characteristics of the beam, obtained at the RFQ entrance for the different phases, must be extremely close to be considered time-independent. Twiss parameters $< \alpha >$ and $< \beta >$ are then taken as input references for calculation of the linac acceptance.[3]..

The following questions then arise: what vane geometry should be imposed, and what length, to obtain the best possible matching? These questions imply that a quality criterion is available. Here we use yield factor F_e, which is the maximum value of the de-matching factor $F_{des}(z, \varphi_{rf})$, depending on longitudinal position z and phase φ_{rf} in the channel. This function is given by the following formula:

$$F_{des}(z, \varphi_{rf}) = \frac{\widehat{X}_{des}(z, \varphi_{rf})}{\widehat{X}_{ada}(z, \varphi_{rf})} - 1 \tag{5.5}$$

where $\widehat{X}_{ada}$ is the envelope of the matched beam calculated during the first stage of optimization and $\widehat{X}_{des}$ is the beam envelope derived from complete transport beginning at the RFQ entrance with the beam characteristics obtained by averaging the inverse transport. Values of F_e of a few percent indicate good entrance section performance, and any value below around 10% is probably acceptable. Figures below 1% involve refinement. Figure 5.6 summarizes the different stages of optimization of the entrance section.

5.1.2.2 Main formulations

A number of formulations have been proposed for determining the potential of the entrance section [5,6,7]. It is to be noted that [7] (F2) is the reference for PARMTEQM. In this study, consideration is given to the following series:

[3] $<>$ means that an average has been calculated relative to the radiofrequency phases.

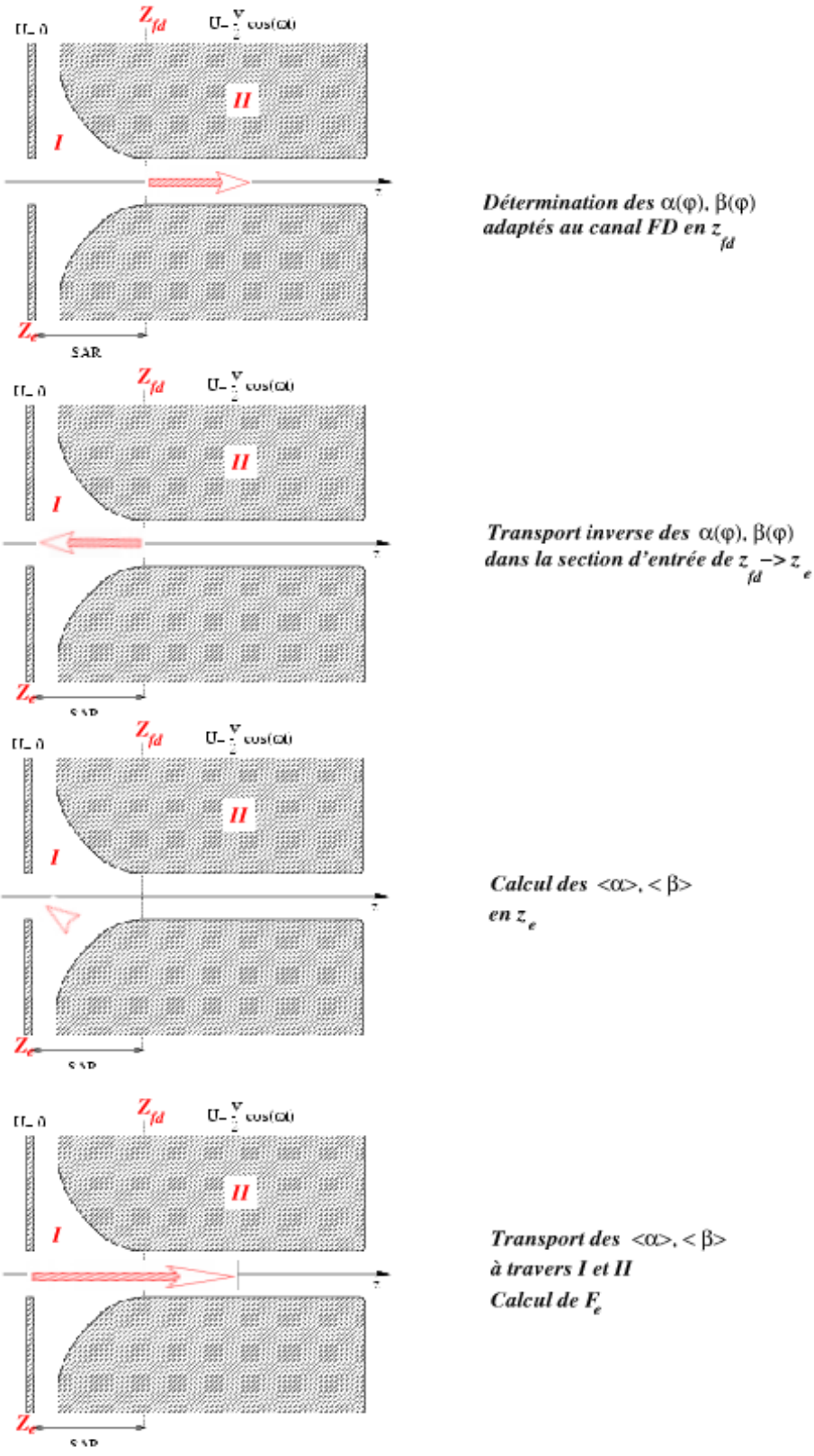

Figure 5.6: Diagram showing the different stages of entrance section optimization.

$$\begin{aligned}
F1:\ \Psi(\rho,\theta,z) &= \tfrac{V}{2}\tfrac{z}{L_{sar}}\textstyle\sum_{m=1,3}\left[A_{0m}\left(\tfrac{\rho}{R_0}\right)^{2m}\cos(2m\theta)\right]\\
F2:\ \Psi(\rho,\theta,z) &= \tfrac{V}{2}\textstyle\sum_{m=1,3}A_m\left[I_{2m}(k\rho)\sin(kz)+3^{-(2m+1)}I_{2m}(3k\rho)\sin(3kz)\right]\cos(2m\theta)\\
F3:\ \Psi(\rho,\theta,z) &= \tfrac{V}{2}\textstyle\sum_{m=1,3}\sum_{n=0,N}\left[A_{0m}\left(\tfrac{\rho}{R_0}\right)^{2n+m}\cos(m\theta)G_n(z)\right]\\
F4:\ \Psi(\rho,\theta,z) &= \tfrac{V}{2}A_1I_2(k\rho)\cos(2\theta)\sin(kz)\\
F5:\ \Psi(\rho,\theta,z) &= \tfrac{V}{2}\tfrac{z}{L_{sar}}\left[A_{01}\left(\tfrac{\rho}{R_0}\right)^{2}\cos(2\theta)\right]
\end{aligned} \tag{5.6}$$

where:

$$G_n(z)=(-1)^n\frac{2!}{4^n n!(n+2)!}\frac{\partial^{2n}G_0(z)}{\partial z^{2n}} \tag{5.7}$$

with:

$$G_0(z)=\frac{\exp\left(-\alpha_q\left(\frac{z-L_{sar}}{L_{sar}}\right)^{2m_q}\right)-\exp\left(-\alpha_q\left(\frac{z+L_{sar}}{L_{sar}}\right)^{2m_q}\right)}{1-\exp\left(-2^{2m_q}\alpha_q\right)} \tag{5.8}$$

and:

$$k=\frac{\pi}{2L_{sar}} \tag{5.9}$$

where L_{sar} is the length of the radial matching section. All these series are part of the Laplace equation solutions (2.4), as per Chapter 2. Formulations $F2$, $F3$, $F4$ correspond to References [7], [6] and [5] respectively. For each development, the different sets of coefficients are determined to ensure optimal continuity with formula (5.4), except for formulation $F4$ which assumes that the FD channel is described by a pure quadrupole (i.e. $A_{01}=1$) [5]. For $F3$, α_q, m_q and L_{sar} can be adjusted.

Before beginning the comparative studies, it is first necessary to consider the advantages and disadvantages of each formulation:

- $F1$ gives the best continuity with the transverse components of the field derived from equation (5.4). Continuity in the longitudinal direction is unsatisfactory, since component $\partial_z\Psi(\rho,\theta,z)$ is not canceled out.

- $F2$ gives satisfactory continuity with the transverse components of the field, it also makes it possible to cancel out the longitudinal component in the vicinity of the FD channel.

- $F3$ is very similar to $F2$ but offers greater parameter flexibility. One of the advantages is that the gap between the end plate of the RFQ and the vane can be monitored [6].

Parameter	Value or type
distribution	uniform
$\varepsilon_{tot.,norm.}$	1 π..mm.mrad
current	100 mA
particles	protons
kinetic energy	95 keV
frequency	352 MHz
voltage	101.4 kV
R_0	4.11 mm
ρ_t/R_0	0.89
A_{01}	0.9826
A_{03}	0.0197

Table 5.9: Main parameters of simulation.

- $F4$ allows smooth connection longitudinally but is extremely simplistic as regards transverse continuity.
- $F5$ has the advantage of enabling quantification of the relative importance of the dodecapolar component relative to the quadrupolar component (i.e. relative to $F1$).

The different yield factors F_e, that can be achieved with these different formulations, as a function of length L_{sar}, are reviewed in the following section.

5.1.2.3 Calculation of F_e with envelope code

In this study, the method described in the previous section is used and transport is calculated with an envelope code written using the functionality of the Mathematica 3.0 application (adaptive Runge-Kutta). The parameters for the beam and the FD channel are given in Table 5.9..

Transport is given by the Frank J. Sacherer envelope equations [8]. The system to be solved is as follows:

$$\left\{ \begin{array}{rcl} \partial_z^2 \widehat{X} + \frac{4<xF_x>}{\gamma m(\beta c)^2 \widehat{X}} - \frac{2K}{\widehat{X}+\widehat{Y}} - \frac{\varepsilon^2}{\widehat{X}^3} & = & 0 \\ \partial_z^2 \widehat{Y} + \frac{4<yF_y>}{\gamma m(\beta c)^2 \widehat{Y}} - \frac{2K}{\widehat{X}+\widehat{Y}} - \frac{\varepsilon^2}{\widehat{Y}^3} & = & 0 \end{array} \right. \tag{5.10}$$

with:

$$K = \frac{qI}{2\pi\varepsilon_0 m(\gamma\beta c)^3} \tag{5.11}$$

where I is the current, q and m are the charge and mass of the particle respectively, γ and β are the relativistic factors of the beam, ε_0 is the permitivity of vacuum, and c is the speed of light in a vacuum. K is referred to as the *generalized perveance* of the beam. During transport,

ε is kept constant. The expression $< xF_x >$ means that the external source is linearized by integrating over the entire distribution. In order to simplify numerical integration of equation (5.10), the Bessel series in the force expressions are truncated after the sixth order. Incremental numerical integration of (5.10) makes it possible to recover the point pairs $(z_i, \widehat{X}_i)$ describing variation in the beam envelope along the axis of propagation. Beginning with reasonable initial conditions, but different from the matched conditions, this envelope consists of different modes of oscillation, including the principal mode sought. To determine the proper initial conditions for the different radiofrequency phases, it is necessary to minimize the difference between the envelope and the expression:

$$A + B\cos(\frac{2\pi z}{\beta\lambda_{rf}} + \varphi_{rf}) \tag{5.12}$$

where A is the average envelope of the beam, and B is the amplitude of modulation of the envelope due to the focusing forces of spatial period $\beta\lambda_{rf}$.. It is therefore assumed that this monofrequency function offers the best representation of the envelope sought, with the envelope beat frequency naturally being that of the focusing forces. Values A and B are therefore sought for which the quantity:

$$\sum_i \left\{ \widehat{X}_i - \left[A + B\cos\left(\frac{2\pi z_i}{\beta\lambda_{rf}} + \varphi_{rf} \right) \right] \right\}^2 \tag{5.13}$$

is a minimum. The procedure used is described in detail in Appendix C.. For each instance of transport over a distance of a number of periods $\beta\lambda_{rf}$, new values of A and B are calculated and taken as initial values for the following transport sequence, i.e.:

$$\left\{ \begin{array}{rcl} (\widehat{X}_0)_{j+1} & = & (A)_j + (B)_j \cos\left(\frac{2\pi z_0}{\beta\lambda_{rf}} + \varphi_{rf}\right) \\ (\partial_z \widehat{X}_0)_{j+1} & = & -(B)_j \frac{2\pi}{\beta\lambda_{rf}} \sin\left(\frac{2\pi z_0}{\beta\lambda_{rf}} + \varphi_{rf}\right) \\ (\widehat{Y}_0)_{j+1} & = & (A)_j - (B)_j \cos\left(\frac{2\pi z_0}{\beta\lambda_{rf}} + \varphi_{rf}\right) \\ (\partial_z \widehat{Y}_0)_{j+1} & = & (B)_j \frac{2\pi}{\beta\lambda_{rf}} \sin\left(\frac{2\pi z_0}{\beta\lambda_{rf}} + \varphi_{rf}\right) \end{array} \right. \tag{5.14}$$

where the quantities with the subscripted j were calculated for the j^{th} instance of transport to obtain the initial conditions of the $(j+1)^{th}$ instance of transport. Convergence of the process is rapid. In less than five instances of transport, the values of A and B only vary by a few tenths of a percent and are such that the quantity F_e is of a few tenths of a percent if we use the expression (5.12) for $\widehat{X}_{ada}(z, \varphi_{rf})$ and $(\widehat{X}_i)_5$ for $\widehat{X}_{des}(z, \varphi_{rf})$.. Figure 5.7 shows the variation in the envelope after three instances of transport.

Once the beam parameters are obtained for the FD channel, it is possible to continue with the process described in Section 5.1.2.1.. We obtain different values of F_e as a function of the length of the entrance section for each formulation (Figure 5.8). The results call for the following comments:

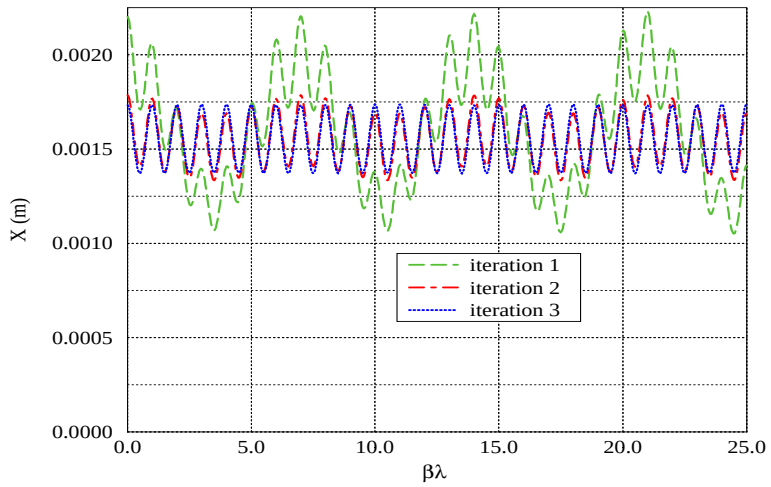

Figure 5.7: $\widehat{X_i}$ for the first three instances of transport with minimization relative to A and B..

- Figure 5.9 shows that the formulation does not allow for the dodecapolar component and the fact that the quadrupolar component is not "pure" (i.e. $A_{01} \neq 1$), reduces the yield of the section.
- Figure 5.10 shows that it is not sufficient only to allow for $A_{01} \neq 1$, but the dodecapolar component must be included in the development used.
- In Figure 5.11, it appears that a linear ramp of the focusing forces gives a lower yield than a ramp of the sinusoidal type (F1 compared to F2 and F3).
- Six cells for the length appears to be a good compromise. Taking a longer section for optimal developments (F2 an F3) reduces F_e but increases the size of the beam and the convergence necessary at the entrance of the structure (Figure 5.13). This means that the beam focusing solenoid must be placed near to the RFQ to obtain these new parameters. It then becomes more difficult to insert diagnostics for characterizing the beam at the RFQ entrance.
- The best performance was obtained with formulations F2 and F3.

5.1.2.4 Calculation of F_e with a multiparticle code

In the previous section, it was assumed that emittance was constant for each instance of transport. This means that the variations in emittance, due to space charge and mismatching, could be

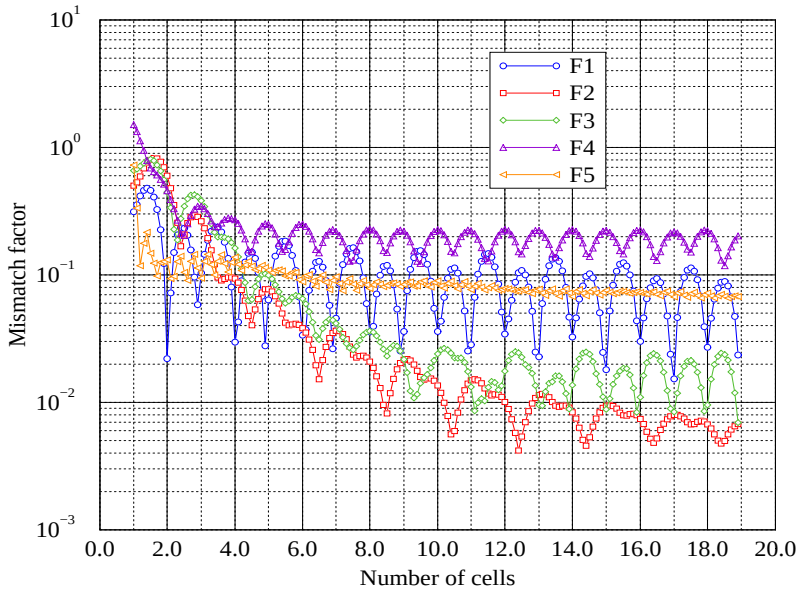

Figure 5.8: Yield factor, F_e, for lengths of 1 to 19 cells with the different formulations (1 cell= $\beta\lambda/2$).

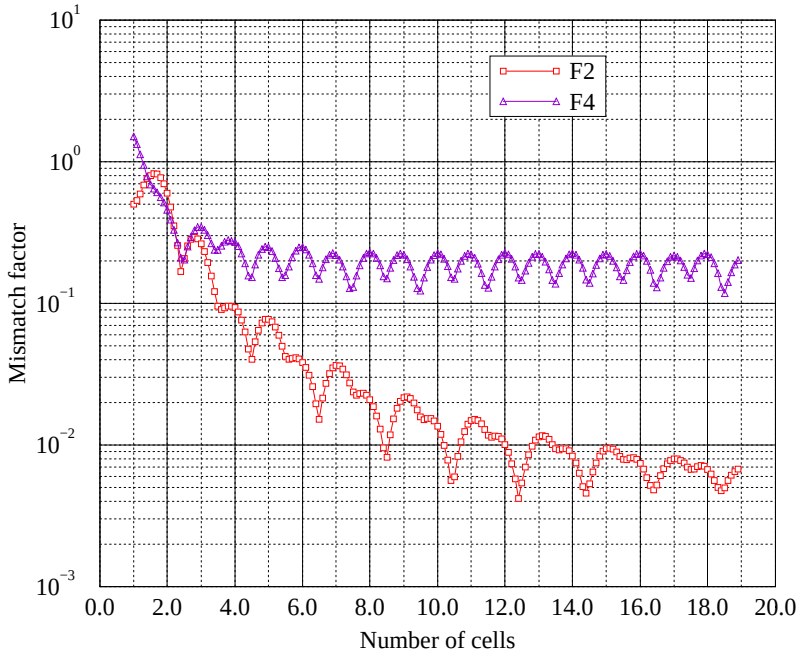

Figure 5.9: Results for formulations F2 and F4.

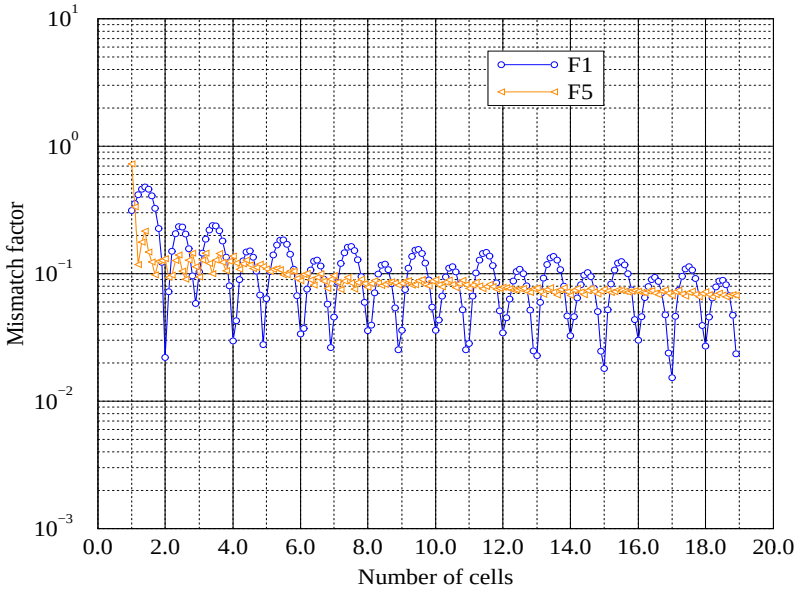

Figure 5.10: Results for formulations F1 and F5.

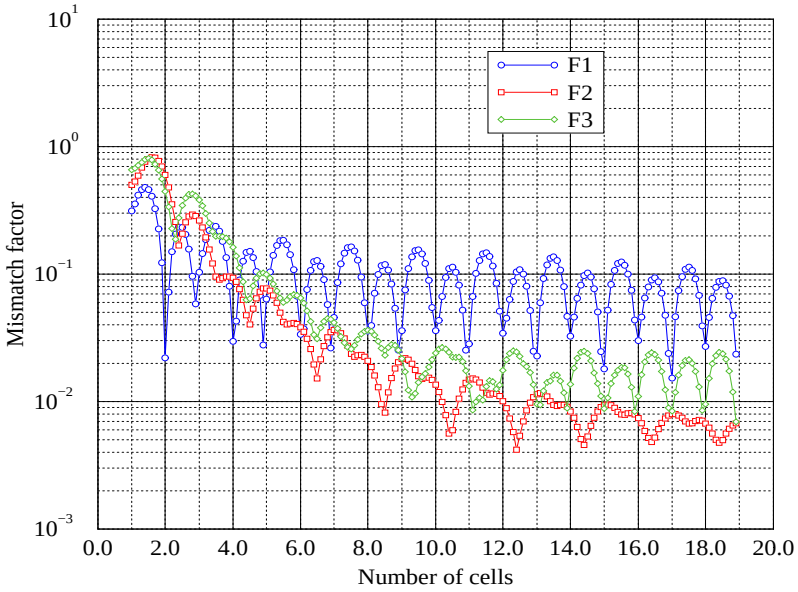

Figure 5.11: Results for formulations F1, F2 and F3.

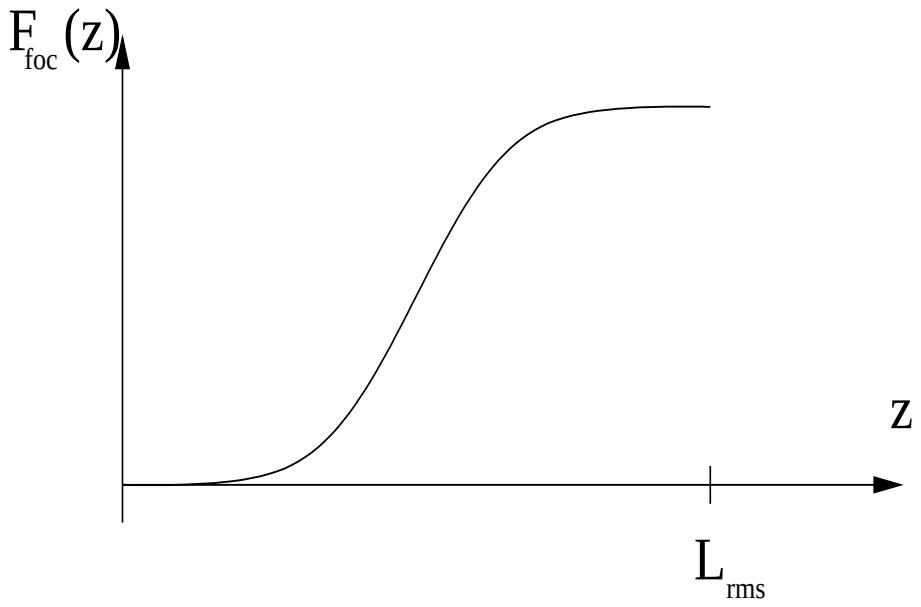

Figure 5.12: Optimum profile for amplitude of external forces in the entrance section (compared to a linear ramp).

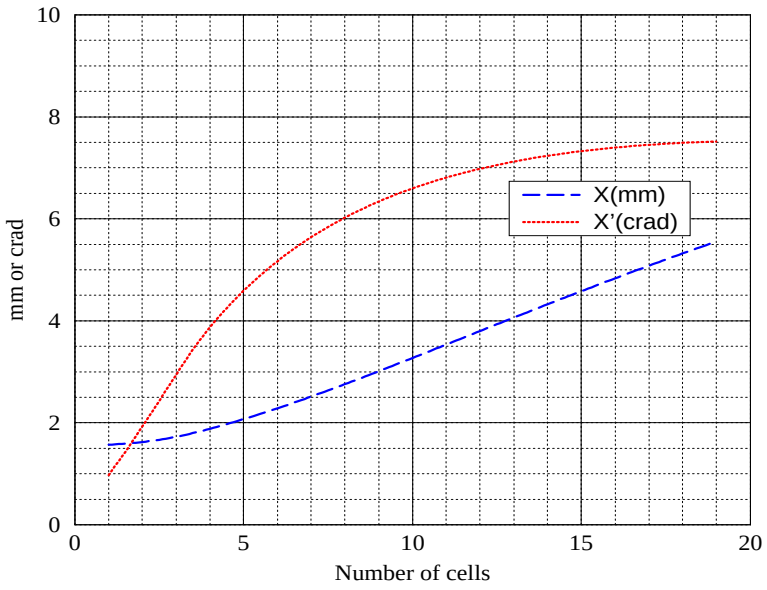

Figure 5.13: Size and convergence of beam necessary at the beginning of the section as a function of the number of cells with formulation F2.

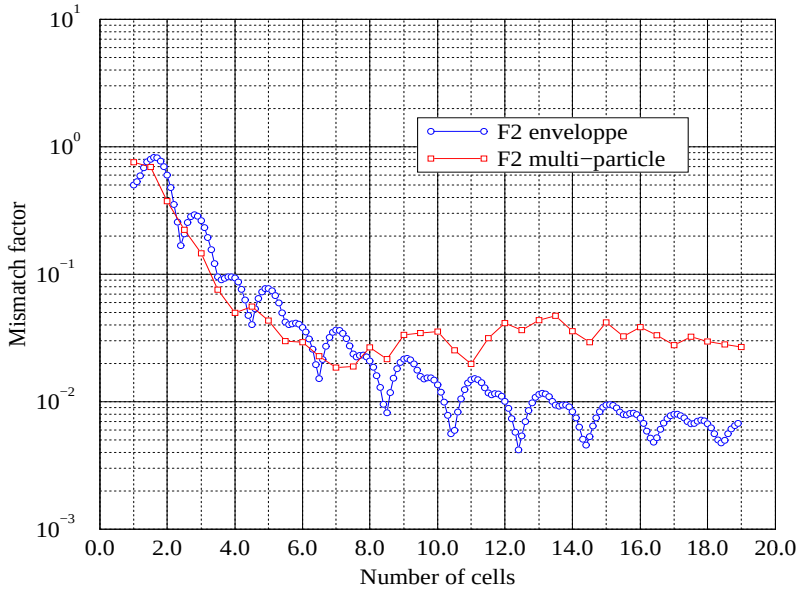

Figure 5.14: Results for formulation F2 in envelope and multiparticle cases.

disregarded. To check this hypothesis[4], we repeated the procedure using a multiparticle code that we developed to allow for emittance variations. The dynamics equations were integrated using a leap-frog process. The space charge forces were calculated by relaxation with Frankel-Young acceleration. The distribution used is of the 4D Water-Bag type [8] with the same rms dimensions as that described in Table 5.9.. The normalized emittance thus increases from 1 to $1.5\ \pi$..mm.mrad. As shown in Figures 5.14, 5.15 and 5.16, the changes in F_e in the multiparticle and envelope cases are broadly comparable as long as a yield of $\sim 10\%$ is acceptable. It would appear that F_e deviations of less than 10% can be attributed to fluctuations in emittance. Indeed, if the original value of emittance changes by 5% and transport is simulated with the envelope code, we obtain a mismatch of a few percent as compared to a few per thousand initially. We therefore consider that if it is desired to obtain mismatch of less than 1%, it is not possible to use the procedure described in Section 5.1.2.1 with an envelope code. However, in view of current diagnostic performance and overall control of beam matching in an RFQ, it would appear that the values of a few percent are quite acceptable. It is also to be noted that, with the multiparticular code, matching does not improve after six cells (Figures 5.14 and 5.15), which substantiates the choice mentioned in the previous section.

[4]This hypothesis is also used in the LANL codes, particularly TRACE 3D which gives matched parameters for the RFQ entrance.

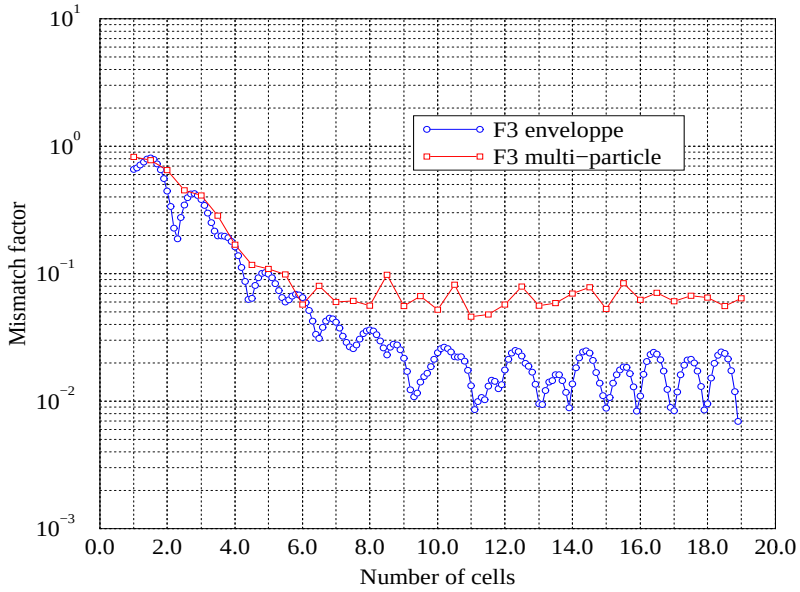

Figure 5.15: Results for formulation F3 in envelope and multiparticle cases.

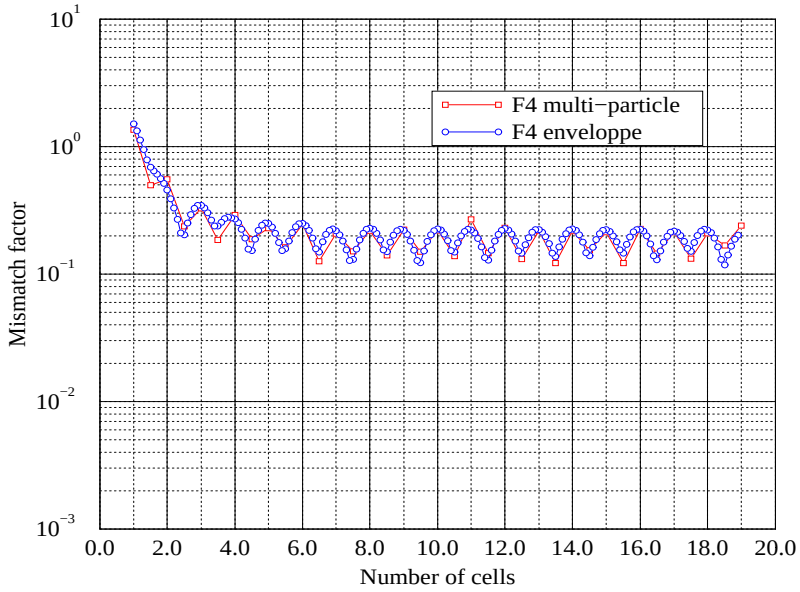

Figure 5.16: Results for formulation F4 in envelope and multiparticle cases.

5.1.2.5 Limits of method

The main hypothesis of the method is that the variations in emittance observed in the multi-particle case can be disregarded and that envelope code transport with constant emittance is acceptable. However, it may be that, when space charge forces are very large, this may no longer be true and that transport can become irreversible[5].. The longer the section, the more critical the emittance enlargement to reach equilibrium. To estimate possible degradation of the quality of the results of the method, it is possible to repeat the procedure with wave number depressions ranging from 0.3 to $1.$, with sections of 6, 12 and 18 cells using the PARMTEQM formulation (F2). The depressions are calculated at beam core level using the following formula for phase advance σ:

$$\sigma = \int_0^{\beta\lambda} \frac{dz}{\beta_f(z)} \tag{5.15}$$

where β_f is the Twiss parameter associated with the amplitude of the transverse oscillations of a core particle. The depression therefore corresponds to the ratio σ/σ_0 where σ_0 is the value when current is nil. For each instance of transport, we have calculated the difference Δ between mismatch factor $(F_e)_{av.}$ obtained in the FD channel only and that, $(F_e)_{ap.}$, obtained in the FD channel after going through the entrance section and back. This quantity Δ thus makes it possible to quantify the contribution of the section in terms of the reversibility criterion:

$$\Delta = (F_e)_{ap.} - (F_e)_{av.} \tag{5.16}$$

In view of the tolerance limits as determined in the previous section, it would appear that variations in Δ can be disregarded. Figure 5.17 shows that they remain below 5%, even with depressions that are relatively low[6] and values of F_e of a few percent. The method based on reversible transport therefore remains valid.

5.1.2.6 Conclusion concerning entrance section

This study of the entrance section shows that the method based on transport reversibility for obtaining beam-matched parameters at the beginning of the structure is valid for a relatively large wave number depression range (0.3 to 1). The optimum length for this section is six cells, i.e. 3 $\beta\lambda$, in view of the degree of matching achieved and the resulting flexibility for the transport line upstream of the RFQ. The formulation used in PARMTEQM gives the best performance in both the envelope and multiparticle cases. This substantiates the choice made by the IPHI and LEDA project teams: F2 formulation over six cells. However, the Twiss parameters given by TRACE 3D for PARMTEQM input would be of better quality if the code allowed for the dodecapolar component.

It is to be noted that, as a result of insertion of a transition cell, the exit section described in Chapter 3 behaves in exactly the same manner as the entrance section. The length can therefore

[5] In previous sections, wave number depression was 0.67.

[6] for a depression of 0.3, emittance varied by 10%.

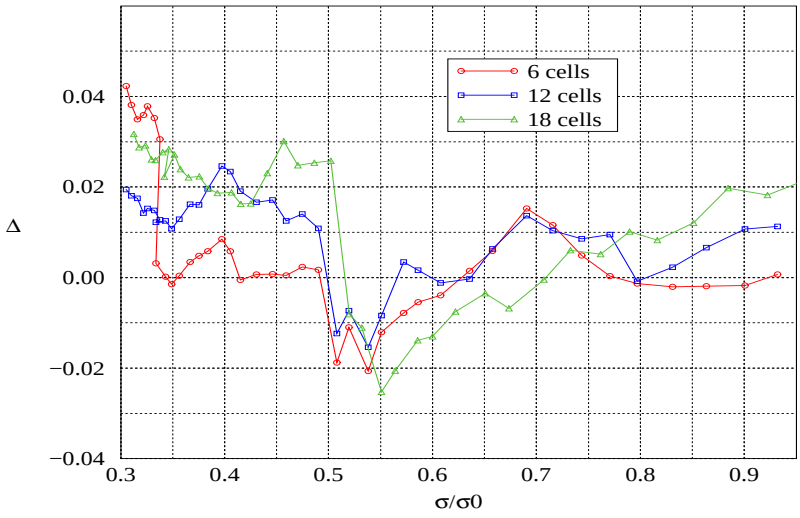

Figure 5.17: Δ for depressions ranging from 0.3 to 0.95 for PARMTEQM formulation with length of 6, 12 and 18 cells.

be adjusted to obtain optimum time independence of the beam at the RFQ exit.

5.1.3 Transition cell (“trancell”)

Section 3.2.4 shows the advantages offered by the use of a transition cell: “smooth” elimination of modulation enabling a short exit section ideal for magnetic quadrupolar insertion after the RFQ without creating energy uncertainty at the exit, and better phase stability of bunches. Since PARMTEQM uses an analytical development to describe the cell, the length of the “trancell” is imposed once continuity with the neighboring cells has been established:

$$L_t = \sqrt{3/4} \cdot \frac{\beta\lambda}{2} \simeq 0.866 \cdot \frac{\beta\lambda}{2} \tag{5.17}$$

This results in a synchronous phase change which can be calculated:

$$\Delta\Phi_s = (\sqrt{3/4} - 1) \cdot 180 \simeq -24.12\, deg. \tag{5.18}$$

It is helpful to know whether this sudden synchronous phase change results in degradation of the optical qualities of the beam, particularly longitudinally. As TOUTATIS does not have any cell length constraints to ensure continuity with the neighboring cells, the variation in emittance was calculated for each plane with lengths ranging from $(\beta\lambda/2 - \beta\lambda/4)$ to $(\beta\lambda/2 + \beta\lambda/4)$ (Figures 5.18 and 5.19). It is clearly apparent that the ideal solution is to maintain $\beta\lambda/2$ for cell length. However, the difference compared to PARMTEQM remains negligible in the three

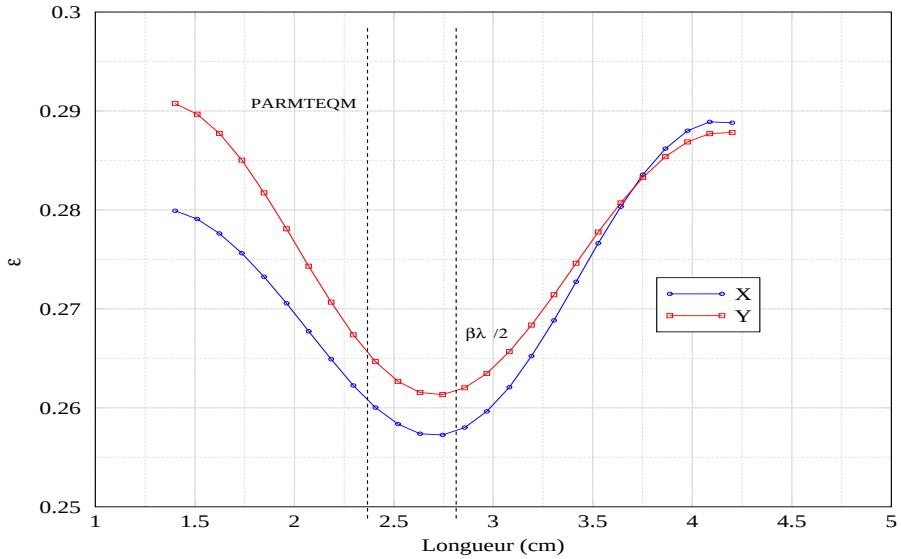

Figure 5.18: Variation in transverse emittance normalized in π..mm.mrad as a function of trancell length.

Parameter	Value
ρ_t/R_0	1.
m	1., 1.2, 1.4, 2., 2.4, 3.
L/R_0	0.75, 2, 4, 8, 11, 15, 20

Table 5.10: Cell parameters calculated with TOSCA.

planes ($\leq$ 2%). The variation in the longitudinal Twiss parameters is also negligible (Figures 5.22 and 5.23). It is possible to adjust the transverse Twiss parameters (Figures 5.20 and 5.21). It is, however, preferable to set the length at $\beta\lambda/2$, even if this means adjusting the length of the exit section.

5.1.4 Peak field

To take the validity of the form factor *F* tables used by PARMTEQM, a comparative study can be made between the values given by CHARGE 3D [4] and TOSCA. This can be revealing as the finite element calculation method of TOSCA is different from the approach used in CHARGE 3D. Calculations were made for different test cells with the parameter set shown in Table 5.10..

The cases where L/R_0 = 0.75 and m = 2, 2.4, 3. are not covered, as they correspond to cells that are difficult to make and pointless in terms of dynamics. The longitudinal profile is extrapolated from the two-term potential. Before considering results of an analysis of these situations, a description is given in the following section of the techniques used to obtain reliable results.

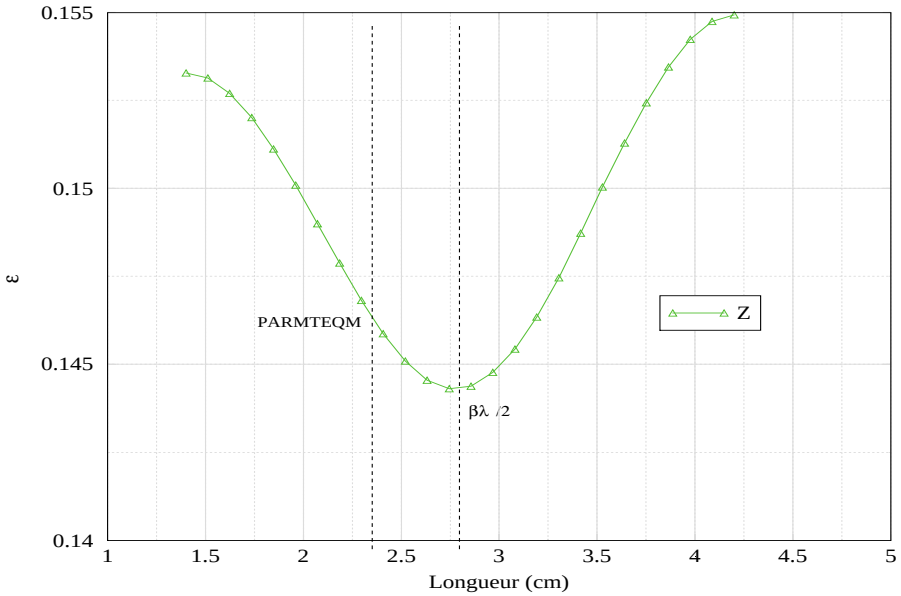

Figure 5.19: Variation in longitudinal emittance, in deg.MeV, as a function of trancell length.

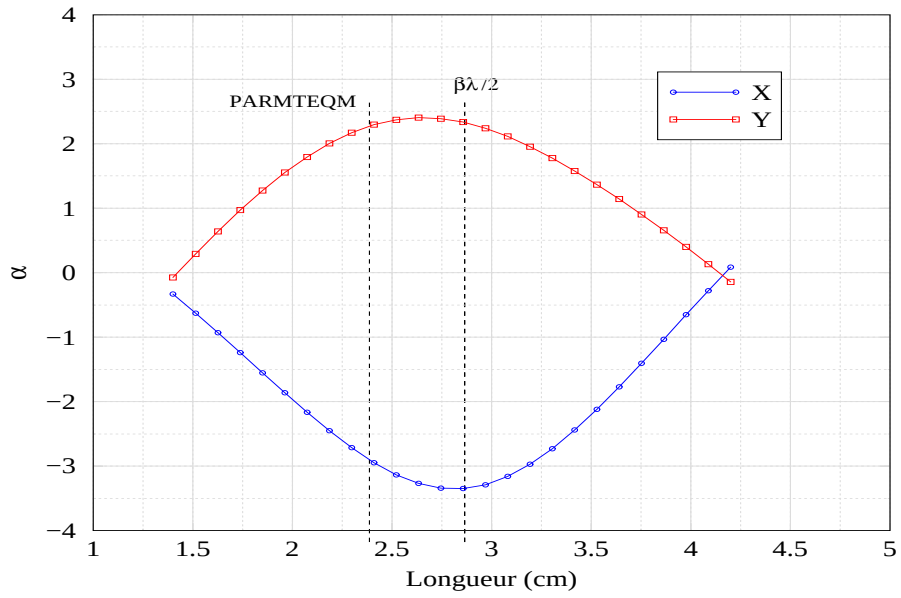

Figure 5.20: Variation in transverse α_t values as a function of trancell length.

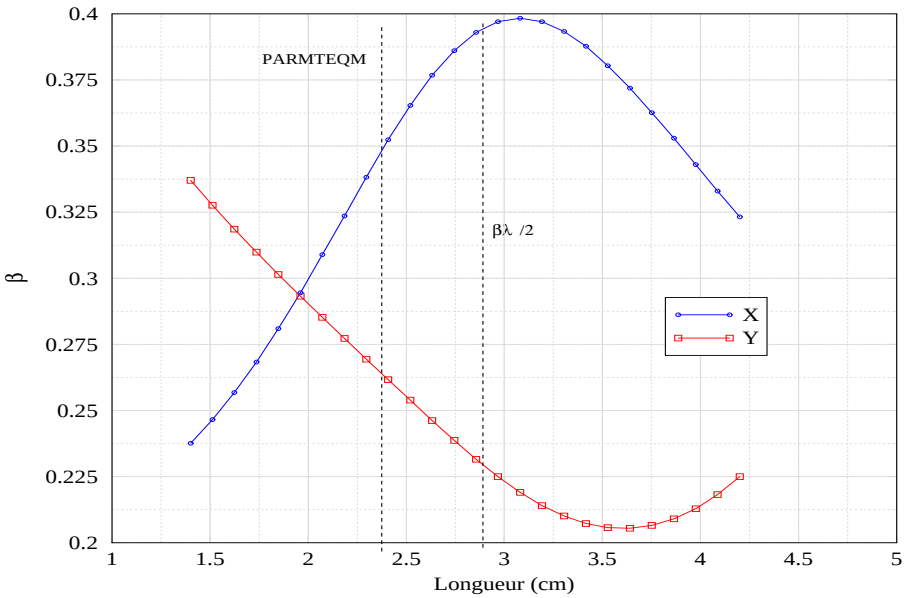

Figure 5.21: Variation in transverse β_t values, in m/rad, as a function of trancell length.

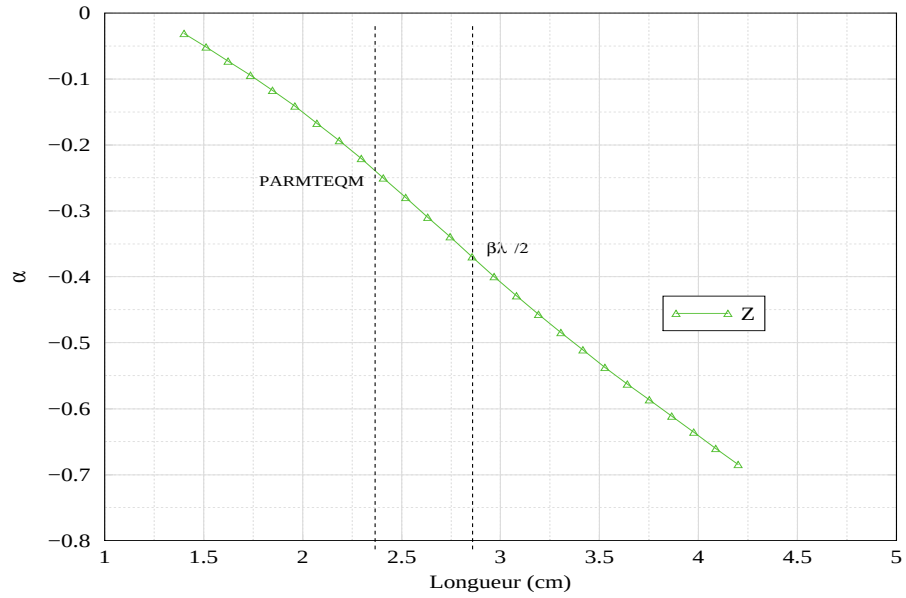

Figure 5.22: Variation in longitudinal α_t values as a function of trancell length.

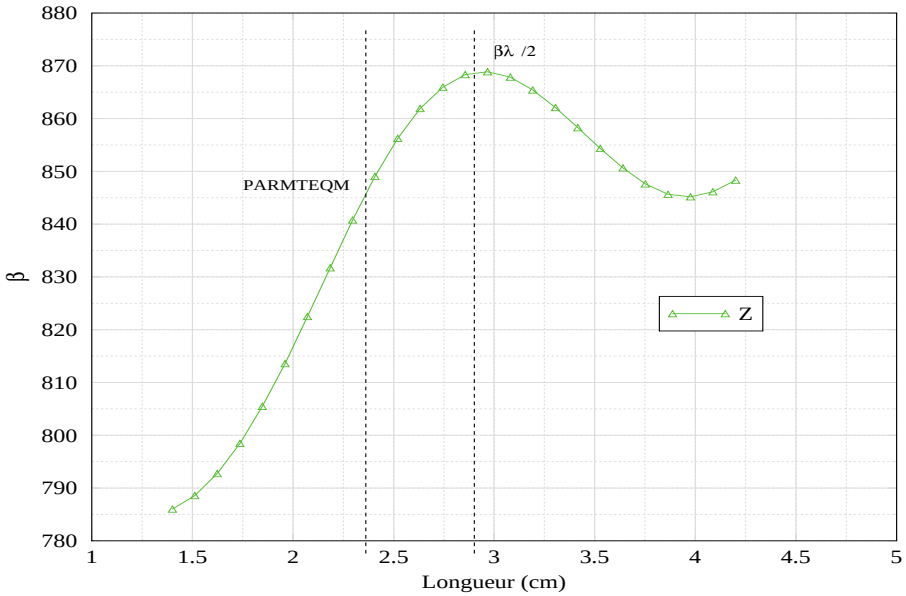

Figure 5.23: Variation in longitudinal β_t values, in deg/MeV, as a function of trancell length.

5.1.4.1 Optimization of the mesh used by TOSCA

5.1.4.1.1 Sub-division of cell

The user of the code has to make a mesh representation of the device for finite element method electromagnetic simulation. To be able to use hexahedral elements, for highest accuracy, discretization must be based on the hexaedral macroelements themselves. These elements are used as a basis for obtaining the final mesh, with each macroelement discretized as elementary bricks. In the RFQ case, unsatisfactory cell division can result in deformation of the elements and give rise to point effects causing spurious intensification of the field. One way of avoiding this type of numerical artifice is to impose a flat surface opposite the high-risk zones. It is for this reason that the sub-division in Figure 5.24 was selected. This method, which is applied in the TOSCA code, gives excellent results which were, in addition, validated by measurement during plasma screen point simulation [9]. Figure 5.25 shows a system of sub-division resulting in the spurious intensification of the electrical field shown in Figure 5.26..

5.1.4.1.2 Element density

To improve calculation accuracy, convergence to a solution is obtained by densifying the number of elementary bricks in the mesh [10]. This is accompanied by an increase in calculation time, and a compromise giving the desired accuracy must be found. This is set at a few tenths per thousand in this study. To adapt the mesh to the shape of the poles, transverse and longitudinal discretization of the cell are decoupled. The pole is discretized to an increasing extent without changing the number of horizontal elements. The cell simulated is unmodulated. Convergence on F is obtained with some forty elements on each pole (Figure 5.27). Hereafter in the study, 80 elements are used per pole in the transverse direction.

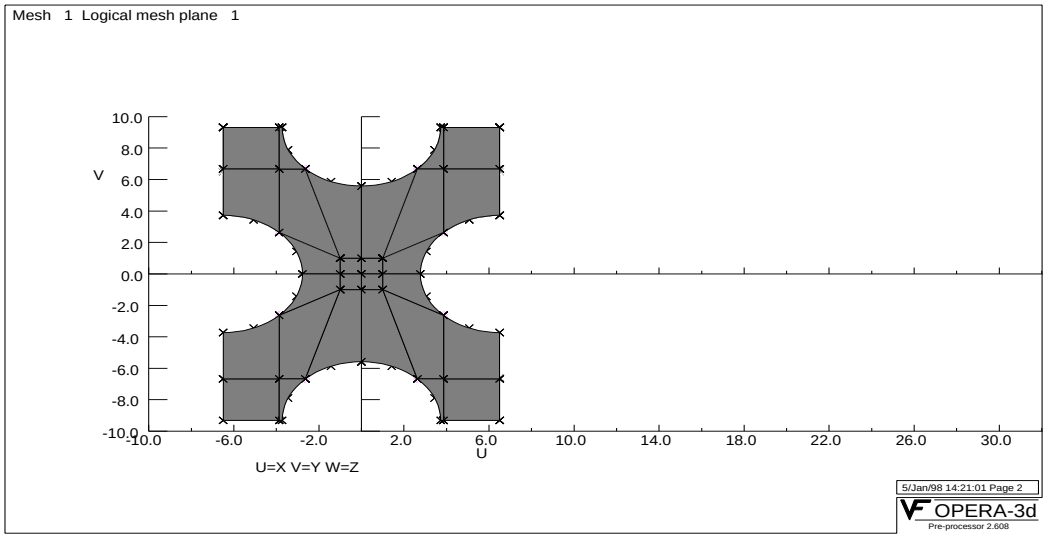

Figure 5.24: Transverse sub-division with square at the center.

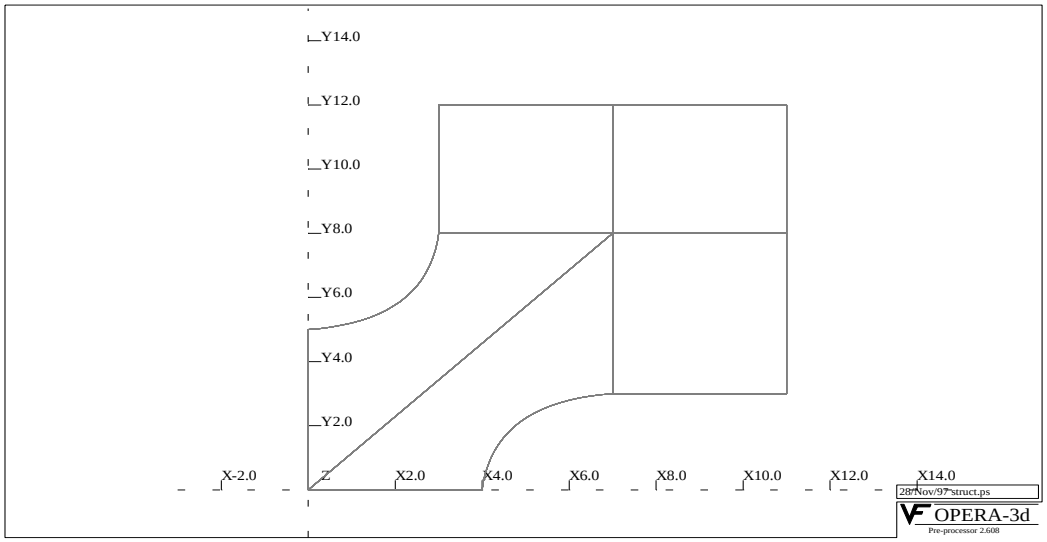

Figure 5.25: Transverse sub-division resulting in spurious point effects (see following figure).

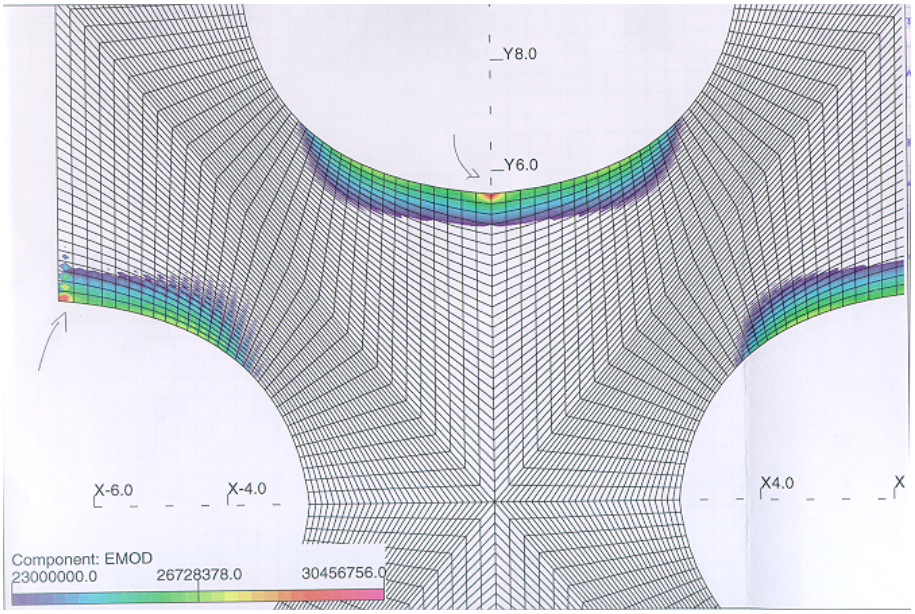

Figure 5.26: Location of peak field obtained with the sub-division shown in Figure 5.25.

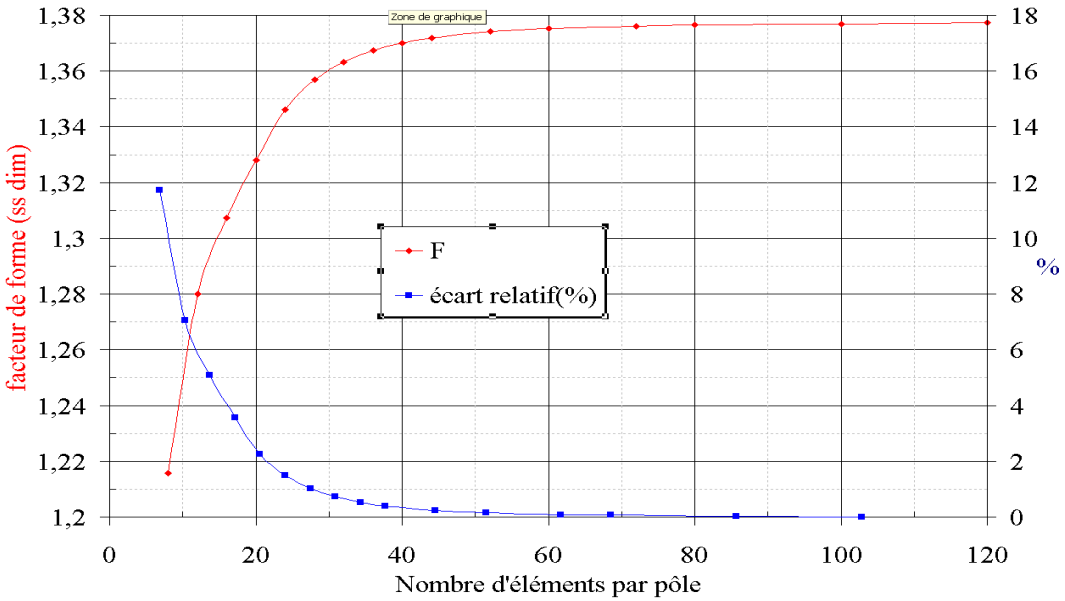

Figure 5.27: Convergence of F as a function of the number of elements per pole in a cell without modulation. The reference for the relative difference is a value F obtained with 120 elements per pole.

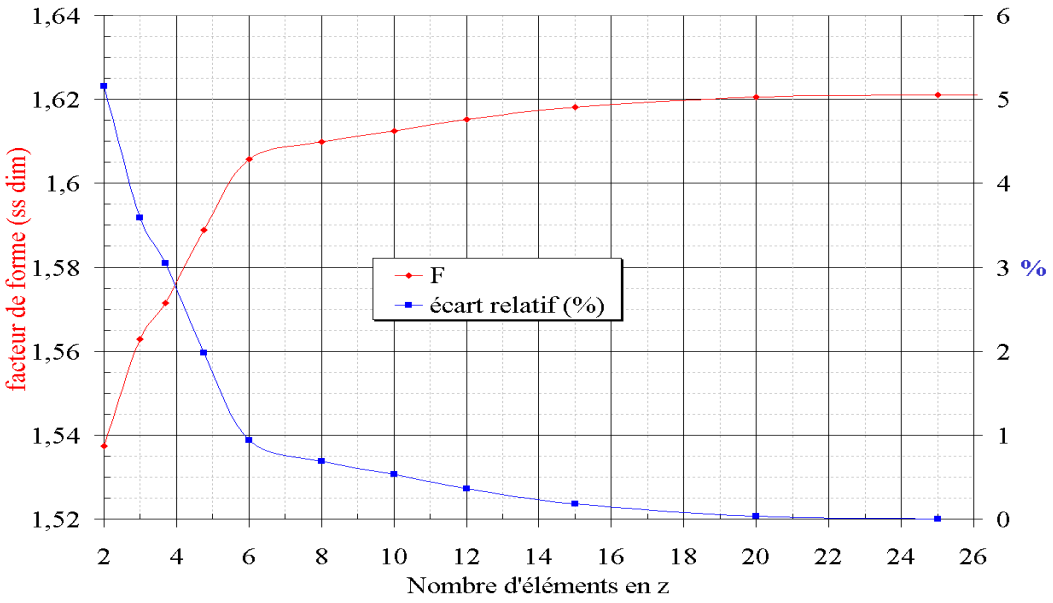

Figure 5.28: Longitudinal convergence with m=3 and L/R_0=2.

m\l	0.75	2	4	8	11	15	20
1	1.70	1.70	1.70	0.54	1.63	1.84	2.34
1.2	0.33	1.27	2.20	1.47	1.15	1.12	1.5
1.4	-0.20	1.85	2.53	1.53	0.96	0.67	1.01
2		1.53	3.26	1.30	-0.08	-0.37	0.00
2.4		1.79	2.73	1.10	-0.52	-0.95	-0.48
3		2.28	4.06	0.83	-0.93	-1.42	-1.14

Table 5.11: Relative difference $(F_{TOSCA} - F_{CHARGE3D})/F_{TOSCA}$ as a %.

For longitudinal discretization, the reference cell is that experiencing the greatest modulation over the shortest distance (i.e. a radius of high longitudinal curvature), with m=3 and (L/R_0)=2. By increasing the number of z elements, convergence is finally reached with around fifteen sub-divisions (Figure 5.28). The reference for the relative difference is the value F obtained with 25 longitudinal sub-divisions.

5.1.4.2 Comparison between CHARGE 3D and TOSCA

Compared to TOSCA, the relative distances, used for reference, are shown in Table 5.11 and plotted in Figure 5.29.. The maximum difference reaches 4% when m is greater than 2 and (L/R_0)=4. However, little use is made of this combination of parameters in RFQs of the LEDA or IPHI types. In a more general context, doubt can persist as to the values as a function of the tolerance limit set. A curious phenomenon is to be noted: neither TOSCA nor CHARGE 3D systematically gives the same values for cells without modulation of different lengths.

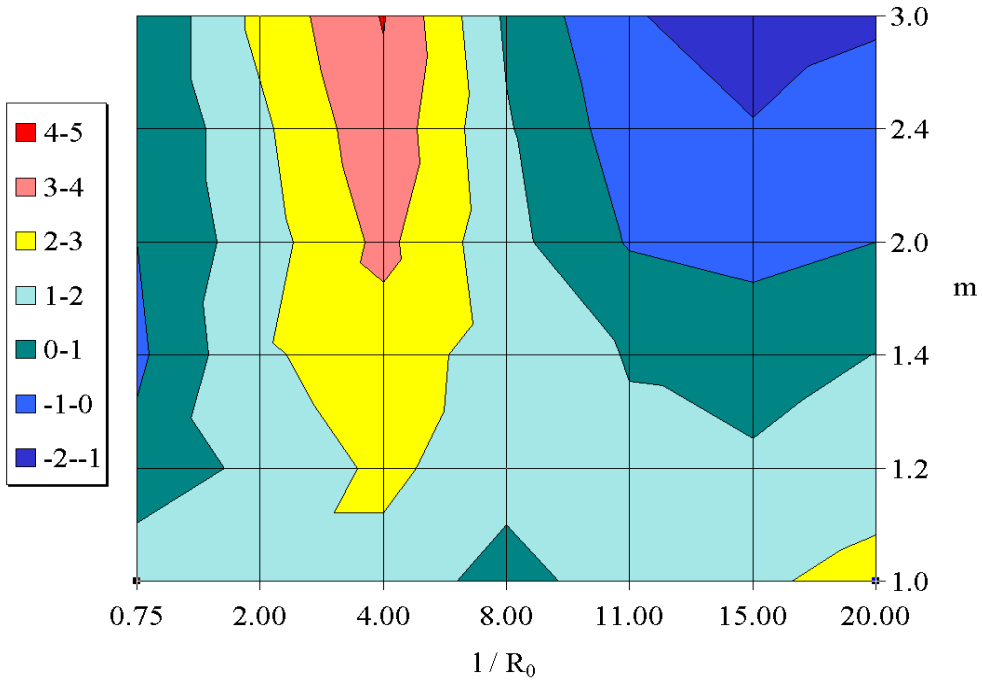

Figure 5.29: Relative difference $(F_{TOSCA} - F_{CHARGE3D})/F_{TOSCA}$ as a %.

5.1.4.3 Comparison between sinusoidal profile and "two-term" profile

One of the motives behind selection of one of the two profiles is their effect on the peak field. The relative differences is given by TOSCA for form factor F between the two profiles are shown in Table 5.12 and plotted in Figure 5.30.. The "two-term" profile is used for reference, so that when the difference is positive, the "two-term" profile gives a lower peak value, and vice-versa.

In Figure 5.30, two zones are apparent:

- For short cells, the peak field is lower for a given profile, depending on the two-term potential. This is explained by the greater longitudinal curvature with the sine. However, conventional RFQs do not have such cells.

- For long cells, a sinusoid gives better results. The phenomenon is due to the smaller inter-electrode gap at the beginning of the cell with "two terms" (Figure 5.31). In this case, the the higher longitudinal ratio L/R_0, the less marked the longitudinal form factor.

5.1.4.4 Peak field study conclusion

The form factors used in PARMTEQM are in excellent agreement with those calculated by TOSCA. A few notable differences observed correspond to cell geometries that are rarely used.

m\l	0.75	2	4	8	11	15	20
1	0.00	-0.75	-1.01	0.00	-1.11	-1.11	-1.11
1.2	6.45	0.69	-0.43	-0.60	-0.61	-0.59	-0.59
1.4	20.71	1.80	-1.07	-1.22	-1.25	-1.19	-1.16
2		4.57	-2.46	-3.58	-3.70	-3.99	-4.18
2.4		4.15	-3.38	-5.31	-5.43	-5.75	-6.18
3		3.35	-4.50	-7.19	-7.56	-8.03	-8.41

Table 5.12: Relative difference $(F_{sinus} - F_{2terms})/F_{2terms}$ as a %.

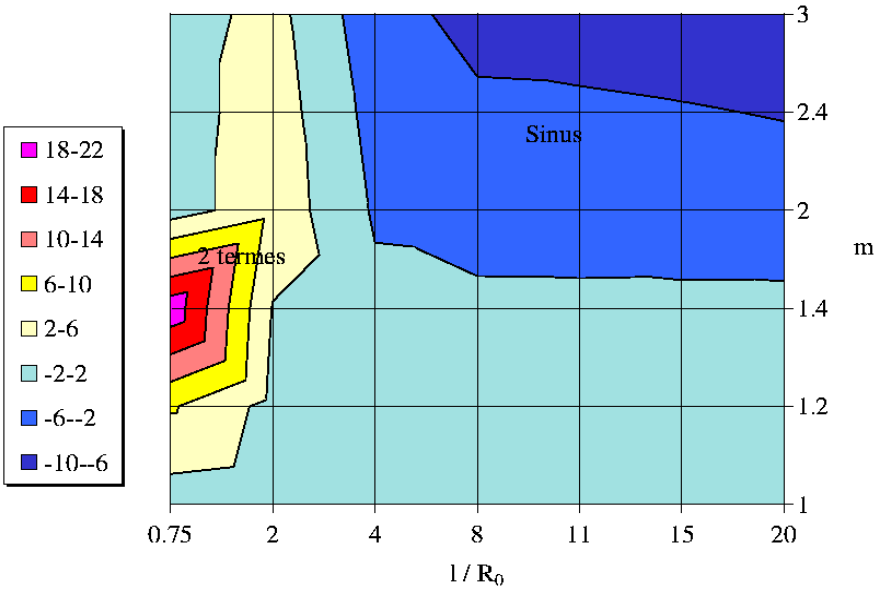

Figure 5.30: Relative difference $(F_{sinus} - F_{2terms})/F_{2terms}$ as a %.

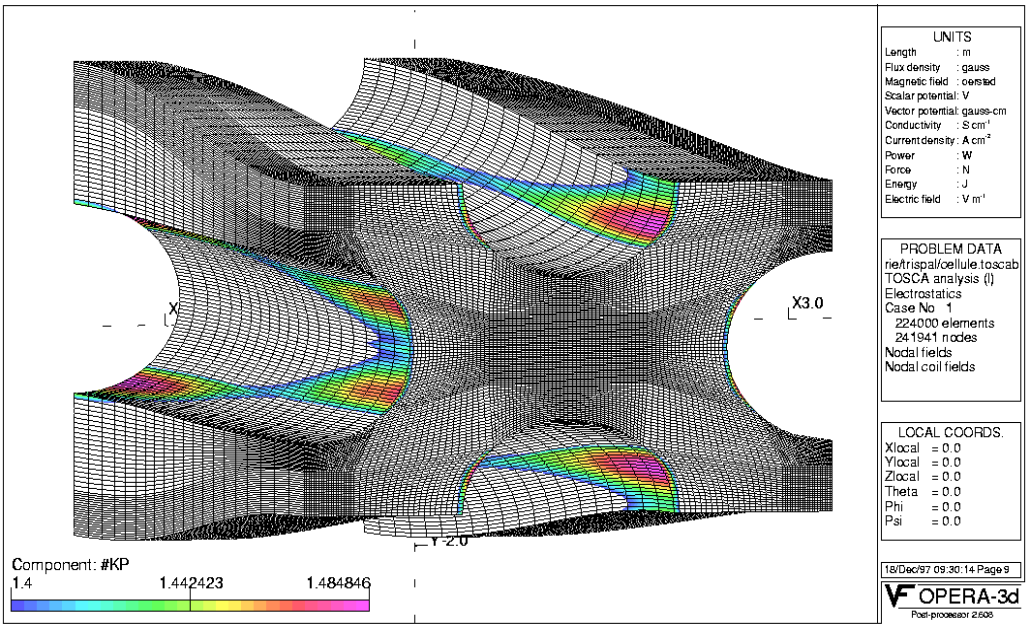

Figure 5.31: Peak field distribution in a cell with a “two-term” profile with L/R_0=11.

The type of longitudinal profile chosen has little effect on the peak field. For RFQs with high $\beta\lambda$ (LEDA and IPHI), a sinusoidal profile appears to be preferable [11]. This is in addition to the other advantages of this type of profile: a larger accelerating component [2], a symmetrical cell with a longitudinal capacity identical to that calculated for the transverse plane at mid-cell and easy construction [12].

5.2 Integration of the dynamics equations

5.2.1 Paraxiality hypothesis

The incremental movement integration method used in PARMTEQM is based on the following equations:

$$\begin{cases} (\gamma\beta_x)_{i+1/2} &= (\gamma\beta_x)_{i-1/2} + \frac{Ze}{\overline{\beta_z}E_0} E_x(\overrightarrow{OM}_i)\sin(\varphi_i)\delta z \\ (\gamma\beta_y)_{i+1/2} &= (\gamma\beta_y)_{i-1/2} + \frac{Ze}{\overline{\beta_z}E_0} E_y(\overrightarrow{OM}_i)\sin(\varphi_i)\delta z \\ (\gamma\beta_z)_{i+1/2} &= (\gamma\beta_z)_{i-1/2} + \frac{Ze}{\overline{\beta_z}E_0} E_z(\overrightarrow{OM}_i)\sin(\varphi_i)\delta z \\ x_{i+1} &= x_i + x'\delta z \\ y_{i+1} &= y_i + y'\delta z \\ \varphi_{i+1} &= \varphi_i + \frac{\omega_{rf}}{(\beta_z)_{i+1/2}c}\delta z \end{cases} \tag{5.19}$$

Parameter	Value or type
distribution	4D Water Bag
$\varepsilon_{r.m.s.,norm.}$ at entrance	0.25 π..mm.mrad
entrance current	100 mA
particles	protons
kinetic energy at entrance	95 keV
kinetic energy at exit	1 MeV
frequency	352.2 MHz
constant voltage	67 kV
constant R_0	2.844 mm
constant ρ_t/R_0	0.85
maximum m	1.46

Table 5.13: Main parameters of simulated RFQ.

where:

$$\begin{cases} x' &= \frac{(\gamma\beta_x)_{i+1/2}}{(\gamma\beta_z)_{i+1/2}} \\ y' &= \frac{(\gamma\beta_y)_{i+1/2}}{(\gamma\beta_z)_{i+1/2}} \end{cases} \tag{5.20}$$

ω_{rf} is the radiofrequency pulse, and the half-integer subscripts indicate that the quantity considered is calculated at a position between the positions where the quantities with integer subscripts are calculated.

The paraxiality hypothesis introduced by Ken Crandall gives rise to certain questions when the divergences of a number of particles reach some hundreds of milliradians. The error induced by the hypothesis can be calculated for a pure horizontal divergence of 300 mrad[7].. By replacing $\overline{\beta_z}$ and $(\beta_z)_{i+1/2}$ by $\overline{\beta}$ and $(\beta)_{i+1/2}$, respectively in equations (5.19), the term:

$$\frac{Ze}{\overline{\beta_z}E_0} \tag{5.21}$$

becomes:

$$\frac{Ze}{\overline{\beta_z}E_0\sqrt{1+\overline{x'}^2}} \approx \frac{Ze}{\overline{\beta_z}E_0}\left(1-\frac{1}{2}\overline{x'}^2\right) = 0.955 \times \frac{Ze}{\overline{\beta_z}E_0} \tag{5.22}$$

which is equivalent to 4.5% error for the fields. Most of the particles have far lower divergences, with the result that, to gain an idea of the impact of such a hypothesis, a specific RFQ was simulated with both versions of PARMTEQM: one with the hypothesis of paraxiality and the other without. Table 5.13 summarizes the RFQ parameters used, which were generated using the LANL codes (CURLI→RFQUICK→PARI).

[7]this is a typical value!

	$\widetilde{\varepsilon}_{x,n.}$($\pi$..mm.mrad)	$\widetilde{\varepsilon}_{y,n.}$($\pi$..mm.mrad)	$\widetilde{\varepsilon}_{z,n.}$(deg.
With paraxiality	0.259	0.266	0.169
Without paraxiality	0.263	0.276	0.160

Table 5.14: rms emittances normalized at exits for the two versions of PARMTEQM.

	Yield	Transmission	Variation in yield	Variation in losses
With paraxiality	87.22%	87.58%	- 5.69%	+ 93.45%
Without paraxiality	92.48%	93.58%	0.%	0.%

Table 5.15: Total transmission and yield with the two versions of PARMTEQM.

The results of the simulations are given in Tables 5.14 and 5.15.. The paraxiality hypothesis results in multiplication of the losses with this RFQ by a factor of 2. This conservatism is due to the artificial rigidity of the trajectory resulting from the hypothesis.

5.2.2 Error due to integration algorithm

To conserve emittance in linear transport, the Jacobian of the transform must be equal to 1 [13]. To quantify the leap-frog quality, it is necessary to calculate the following expression:

$$\Im = \begin{vmatrix} \frac{\partial u_{i+1}}{\partial u_i} & \frac{\partial u_{i+1}}{\partial v_i} \\ \frac{\partial v_{i+1}}{\partial u_i} & \frac{\partial v_{i+1}}{\partial v_i} \end{vmatrix} \tag{5.23}$$

Here, the transform can be written as follows:

$$\left\{ \begin{array}{rcl} v_{i+1} & = & v_i + \frac{Zec^2}{2E_0} \left[E_u(\overrightarrow{OM}_i) + E_u(\overrightarrow{OM}_{i+1}) \right] \delta t \\ u_{i+1} & = & u_i + \frac{1}{2} \left[v_i + v_{i+1} \right] \delta t \end{array} \right. \tag{5.24}$$

where $u = x, y, z$ and $v = v_x, v_y, v_z$.. As force only depends on position (electrical field), the following is obtained:

$$\begin{array}{rcl} \frac{\partial u_{i+1}}{\partial u_i} & = & 1 \\ \frac{\partial u_{i+1}}{\partial v_i} & = & \frac{1}{2}\delta t \\ \frac{\partial v_{i+1}}{\partial u_i} & = & \frac{\delta t}{2} \frac{Zec^2}{E_0} \frac{\partial}{\partial u_i} \left[E_u(\overrightarrow{OM}_i) \right] \\ \frac{\partial v_{i+1}}{\partial v_i} & = & 1 \end{array} \tag{5.25}$$

substituting into (5.23), the calculation of $\Im$ gives:

$$\begin{array}{rcl} \Im & = & 1 - \frac{Zec^2}{E_0} \frac{\delta t^2}{4} \frac{\partial}{\partial u_i} \left[E_u(\overrightarrow{OM}_i) \right] \\ & = & 1 - F(\overrightarrow{OM}_i) \frac{\delta t^2}{4} \end{array} \tag{5.26}$$

where:

$$F(\overrightarrow{OM}_i) = \frac{Zec^2}{E_0} \frac{\partial}{\partial u_i} \left[E_u(\overrightarrow{OM}_i) \right] \tag{5.27}$$

The Jacobian is therefore not strictly equal to 1. It is to be noted that if the velocities and positions were not calculated for intermediate instants, there would be no factor of 1/4 in the expression (5.26). This first calculation calls for the following remarks:

- Error is proportional to $\delta t^2/4$..
- If the force is linear, the error is constant in the plane in question.
- If the force expression contains non-linear terms, the error becomes a function of the coordinates of the particles.

To estimate the combined error for the entire transport instance, it is necessary to calculate the product of the Jacobians of each increment. For simplification, we consider the following field:

$$E_u(\overrightarrow{OM}_i, t) = \frac{V}{R_0^2} u \sin(2\pi f t) \tag{5.28}$$

where V=100 kV, R_0= 4 mm and f=350 MHz. The product sought can be written as:

$$\prod_{i=1}^{N} \Im_i = \prod_{i=1}^{N} \left[1 - \frac{Zec^2}{E_0} \frac{\delta t^2}{4} \frac{V}{R_0^2} \sin(2\pi f t) \right] \tag{5.29}$$

where N is the number of calculation increments. If this number is large, expression (5.29) can be made upper bound by:

$$\prod_{i=1}^{N} \Im_i < 1 - N \left[\frac{Zec^2}{E_0} \frac{V}{R_0^2} \right]^2 \frac{\delta t^4}{16} \tag{5.30}$$

as the large number of terms makes it possible to disregard the double products and $\sin^2$ is an upper bound of 1. If increment δt is a fraction of period $1/f$, the upper bound of error, ε, can be written:

$$\varepsilon = N \left[\frac{Zec^2}{E_0} \frac{V}{R_0^2} \right]^2 \frac{\delta t^4}{16} = N_c \left[\frac{Zec^2}{E_0} \frac{V}{R_0^2} \right]^2 \frac{1}{32 f^4 n^3} \tag{5.31}$$

where $\delta t = 1/(n \cdot f)$, N_c, the number of cells passed through, with one cell passed through in one half-period. Figure 5.32 shows the variation in the error as a function of N_c for protons with $n = 20, 30, 40$ and $f = 350, 700$ MHz. For the IPHI project RFQ case (600 cells at 300 MHz), the upper bound is around 5% when n=20 and a few thousandths when n=40. The instance of transport with a system of the leap-frog type in TOUTATIS gives a variation in normalized rms emittance of 2% in the horizontal plane and 0.3% in the vertical plane between n=20 and n=40. The variation in z is only 0.1%. It can be concluded that subdividing the cell into 10 segments in PARMTEQM is not critical. However, if it is wished to predict the exit emittance with an accuracy of less than 1%, subdivision into 20 segments is preferable. It should also be noted that the error is proportional to the force gradient and inversely proportional to the 4th power of the frequency.

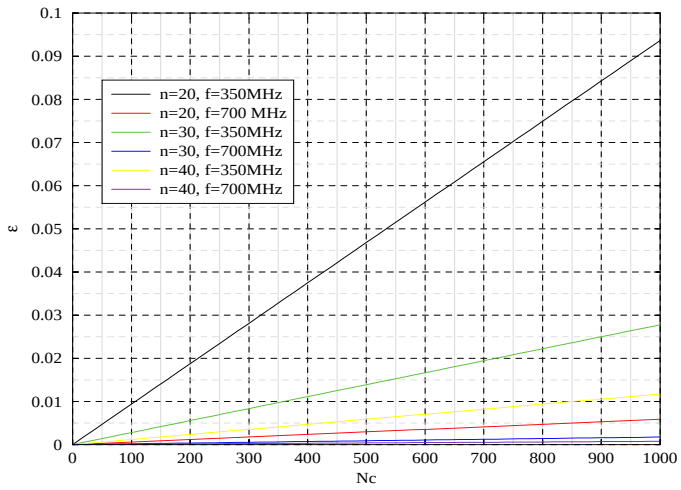

Figure 5.32: Variation in upper-bound error as a function of the number of cells passed through N_c for different frequencies and time increments.

	$\widetilde{\varepsilon}_{x,n.}/\widetilde{\varepsilon}_{0,n.}$	$\widetilde{\varepsilon}_{y,n.}/\widetilde{\varepsilon}_{0,n.}$	$\widetilde{\varepsilon}_{z,n.}$(deg.MeV)
TOUTATIS	1.33	1.34	0.209
PARMTEQM	1.28	1.29	0.237

Table 5.16: Increase in normalized rms transverse emittance and longitudinal emittance with PARMTEQM and TOUTATIS in the 225 mA case without misalignment. In these simulations, the two codes have the same integration system (leap-frog) and the same loss criterion (a square whose side is twice the minimum gap).

5.3 Image effects and space charge forces

The calculation includes a number of uncertainties: the validity of the transform used to reconstitute the bunch distribution at any time (only the quadrupolar term being considered for the transform), the symmetry of revolution of the bunch at the middle of the cell and for the rest of the cell (the space charge fields not having been recalculated), the representation of the bunch as the superimposition of a sphere and a cylinder uniformly charged for the image effects.

For the symmetry of revolution hypothesis (SCHEFF sub-program), it has been demonstrated that the approximation raises problems with a beam with elliptical transverse symmetry in a continuous focusing channel with the PICNIC sub-program [14]. PICNIC uses the same principles as SCHEFF, but is based on a Cartesian 3D mesh. In this study, a bunch of ellipsoidal shape would retain, on average, an elliptical profile transversally (ratio of axis α varying between 1.16 and 2.58). Figure 5.33 shows the increases in emittance, in each plane, in accordance with the value of the α axis ratio. Error mainly takes the form of spurious increase in emittance in certain planes caused by coupling due to the symmetry hypothesis.

It is interesting to note that, in our case, when modulation occurs in the RFQ, the tranverse distribution of the bunch tends to take the shape of a lozenge (Figure 5.34). This is the result of

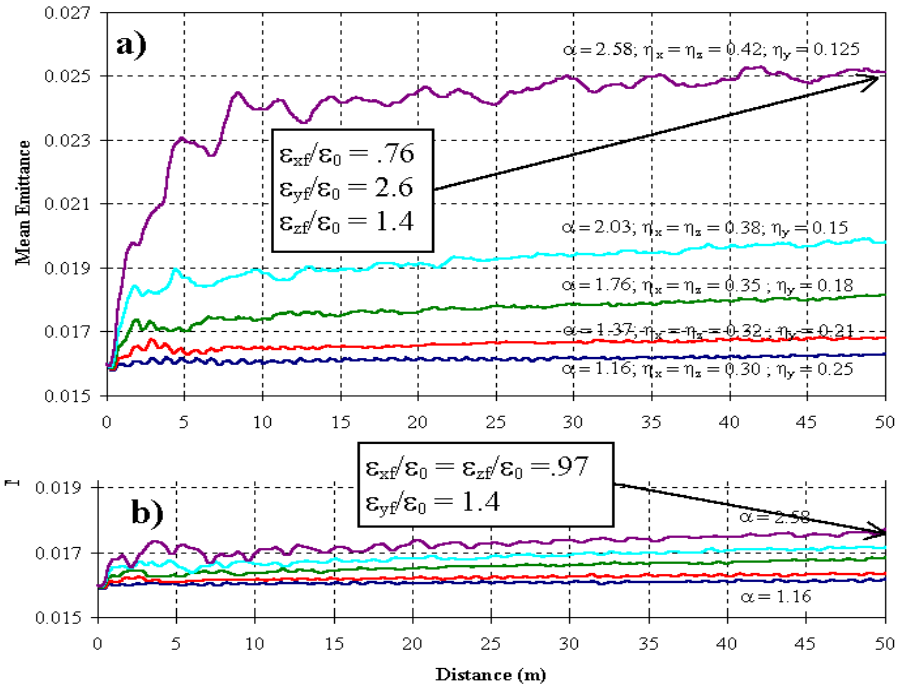

Figure 5.33: Increase in emittance with an ellipsoid of half-size X=Z=Y/α in a continuous focusing channel: a) SCHEFF (Space CHarge EFFects), b) PICNIC (Particle In Cell Numerical Integration between Cubes).

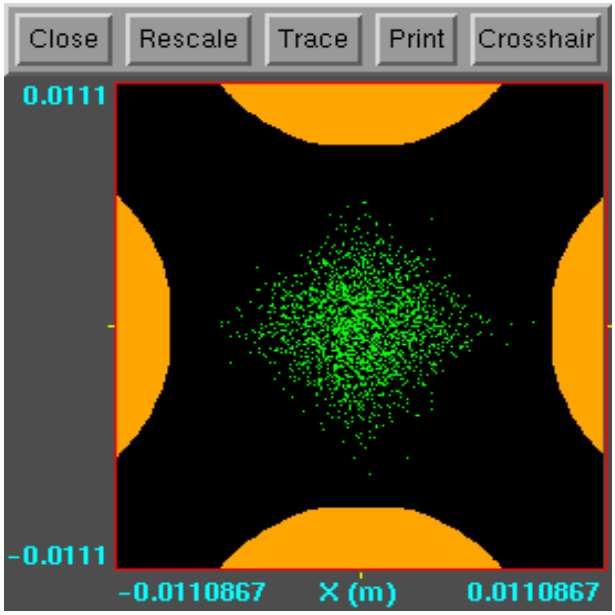

Figure 5.34: Typical transverse profile of beam induced by modulation.

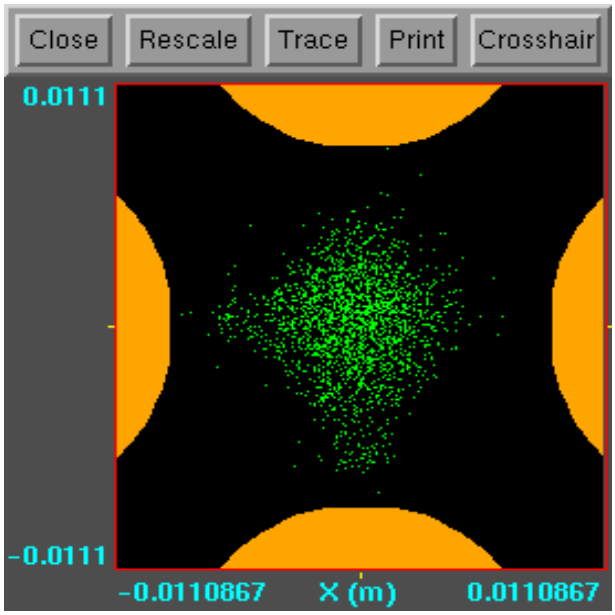

Figure 5.35: Transverse profile of beam obtained in a misalignment study.

	$\widetilde{\varepsilon}_{x,n.}/\widetilde{\varepsilon}_{0,n.}$	$\widetilde{\varepsilon}_{y,n.}/\widetilde{\varepsilon}_{0,n.}$	$\widetilde{\varepsilon}_{z,n.}$(deg.MeV)
TOUTATIS	1.35	1.23	0.519
PARMTEQM	1.28	1.28	0.501

Table 5.17: Increase in normalized rms transverse emittance and longitudinal emittance with PARMTEQM and TOUTATIS in the 0 mA case without misalignment.

	$\widetilde{\varepsilon}_{x,n.}/\widetilde{\varepsilon}_{0,n.}$	$\widetilde{\varepsilon}_{y,n.}/\widetilde{\varepsilon}_{0,n.}$	$\widetilde{\varepsilon}_{z,n.}$(deg.MeV)
TOUTATIS	1.37	1.45	0.219
PARMTEQM	1.60	1.60	0.269

Table 5.18: Increase in normalized rms transverse emittance and longitudinal emittance with PARMTEQM and TOUTATIS in the 225 mA case with misalignment by +600 μm in X and Y.

	$\widetilde{\varepsilon}_{x,n.}$($\pi$..mm.mrad)	$\widetilde{\varepsilon}_{y,n.}$($\pi$..mm.mrad)	$\widetilde{\varepsilon}_{z,n.}$(deg.MeV)
"Square" criterion	0.259	0.269	0.168
"Electrodes" criterion	0.270	0.282	0.176
Variation	- 4.07%	-4.61%	-4.55%

Table 5.19: Variation in normalized rms emittances in all versions of TOUTATIS. Variation is that induced by the "square"

an octupolar effect. Another interesting case is that of error studies to determine, for instance, the sensitivity of the machine to beam misalignment. Once again, the average profile of the beam does not correspond to a circle (Figure 5.35). This may indicate that the image and space charge forces are not properly represented in the PARMTEQM code, although the code probably reflects most of the disturbance effect. Again, this may be accepted as a function of the tolerance limits to be applied. In addition, Tables 5.16, 5.17 and 5.18 contain the exit emittances calculated for an RFQ at high current[8] with PARMTEQM and TOUTATIS. The difference, for the prediction of longitudinal emittance, reaches 13% at 225 mA as compared to 3% at 0 mA, and the increase in transverse emittance is therefore perfectly comparable for the two codes. For the beam misalignment case, SCHEFF predicts an increase in tranverse emittance of 60% whereas it is only 40% with TOUTATIS. The transmissions given by the two codes are identical.

5.4 Loss management

5.4.1 Transverse losses

In PARMTEQM, any particle outside the square twice the minimum opening of a side is considered to be lost. This criterion therefore applies to the hypothesis of a particle with an amplitude such that it is located outside the square, and cannot return within it. To verify this hypothesis, this criterion was introduced into TOUTATIS and two simulations were made of the same RFQ, one with the "square" criterion and the other with the criterion allowing for the actual geometry of the poles referred to as the "electrode" criterion. The RFQ considered is that in Section 5.2..

The results of the simulations are shown in Tables 5.19 and 5.20.. Tables 5.21 and 5.22 compare the results obtained with TOUTATIS in the "square" configuration and the two versions of PARMTEQM with and without the paraxiality hypothesis. This comparison is also of interest as here we are concerned mainly with particles with high-transverse amplitudes.

The results show that this approximation can be extremely unsatisfactory if it is wished to accurately predict activation of the machine, and certainly worse than in the PARMTEQM case. However, it must once again be emphasized that the figures given here are only valid for the RFQ simulated in the study. For the IPHI RFQ, for which the comparison was also made, there is no significant difference, as the beam is well confined within a radius smaller than the minimum gap. However, this approximation certainly raises problems for all RFQs if studies are made of errors where beam containment is substantially degraded.

[8]This RFQ is a version of the RFQ2 at CERN upgraded to 5 MeV. This structure is described in Section 15..

	Yield	Transmission
“Square” criterion	92.45%	93.81%
“Electrodes” criterion	96.72%	98.31%
Variation	-4.41%	-4.57%
Loss variation	+130.20%	+266.27%

Table 5.20: Variation in total transmission and yield for the two versions of TOUTATIS. Variation is that induced by the “square”..

	$\widetilde{\varepsilon}_{x,n.}$($\pi$..mm.mrad)	$\widetilde{\varepsilon}_{y,n.}$($\pi$..mm.mrad)	$\widetilde{\varepsilon}_{z,n.}$(deg.MeV)
TOUTATIS “square”	0.259	0.269	0.168
PARMTEQM with paraxiality	0.259	0.266	0.169
PARMTEQM without paraxiality	0.263	0.276	0.160

Table 5.21: Variation in normalized rms emittance for the two versions of PARMTEQM and the “square” version of TOUTATIS.

	Yield	Transmission
TOUTATIS “square”	92.45%	93.81%
PARMTEQM with paraxiality	87.22%	87.58%
PARMTEQM without paraxiality	92.48%	93.58%

Table 5.22: Variation in total transmission and yield for the two versions of PARMTEQM and the “square” version of TOUTATIS.

The comparison between the two versions of PARMTEQM shows how the code is improved by abandoning the paraxiality hypothesis.

5.4.2 Particles with phase shift

Management of these particles is described in Section 3.6.2.. These are dealt with by phase translation to "return" the particle to the simulation window. This translation, although legitimate, cannot properly allow for the consequences of shift on simulation.

Let us consider the case of an RFQ without transverse losses that accelerates only 90% of the bunch injected. The beam entrance velocity would be $0.01\times$c and the exit velocity would be $0.1\times$c, the initial charge by $\beta\lambda$, Q. The unaccelerated particles would retain a velocity of $0.01\times$c, and the total charge would then be underestimated in the PARMTEQM calculations as this code always gives Q whereas the exact value is $1.9\times$Q. The explanation is as follows. When the bunch is accelerated, our simulation window of length $\beta\lambda$ increases with β and unaccelerated particles from the preceding bunches enter it. There are then two beams in the accelerator: one beam modulated according to the β law in the channel, and an unaccelerated beam[9].. In the previous case, the charge of this continuous beam is therefore underestimated at the end of the RFQ by a factor of 10, and that of the total beam by a factor of 1.9.

In practice, the impact of this error on the simulation is probably negligible. There are a number of reasons for this. The transverse focusing forces are frequently increased during the capture phase, the shifted particles do not undergo the same depression as the bunch and therefore become unstable and most are lost in the first part of the RFQ. At the end of the RFQ, where the error would have greater consequences, the beam has a far lower charge density than the bunch and makes little contribution to space charge.

To seek to clarify the problem, the possibility of arbitrarily adding charge during transport was added to TOUTATIS. This was arbitrary as the actual transverse coordinates of these particles are unknown. The code uses a particle shifting from the bunch as the marker particle to estimate the actual longitudinal density. In practical terms, if the particle is shifted with a velocity 10 times lower than the synchronous velocity, nine particles with identical transverse coordinates, $\beta_d\lambda$ apart longitudinally, are injected for calculation of the space charge. β_d is equal to one tenth of $\beta_{synchronous}$.. Two RFQ cases were calculated with and without this system: the version of the IPHI RFQ with its nominal voltage, and the same version but with a voltage reduced by 10% over the entire structure. This last case is particularly interesting as a large number of particles are then shifted and total transmission remains satisfactory. Table 5.23 gives the results. The differences do not effectively appear to indicate any major problems with the nominal voltage case. The reduced voltage case results in a difference between longitudinal emittances of 30%. It cannot, however, be considered that the error is of the second order.

[9] In fact, the beam is not necessarily monokinetic. It is populated with particles with velocities that vary with the zones where the particles have been shifted.

	$\widetilde{\varepsilon}_{x,n.}/\widetilde{\varepsilon}_{0,n.}$	$\widetilde{\varepsilon}_{y,n.}/\widetilde{\varepsilon}_{0,n.}$	$\widetilde{\varepsilon}_{z,n.}$(deg.MeV)	Transmission	Yield
Nominal voltage (ss)	1.04	1.04	0.148	99.72%	99.60%
Nominal voltage (av)	1.04	1.04	0.153	99.66%	99.58%
Reduced voltage (ss)	1.08	1.09	0.182	95.48%	78.75%
Reduced voltage (av)	1.11	1.11	0.238	95.45%	75.29%

Table 5.23: Exit emittances, transmission and yield for different cases (ss = without particles added, av = with particles added).

5.5 Comparison with experimental results

In 1993, RFQ2 was integrated into the low-energy line of Linac 2 to improve the performance of the PS [16].. During the summer of 1992, RFQ2 was installed on a test bench to compare the measurements obtained on the beam with the results of simulation made at the time with the PARMULT code and a version of the PARMILA code[10].. PARMULT is an early version of PARMTEQM with only the four main multipoles (quadrupole, dodecapole, periodic monopole and periodic octupole), and with no provision for image effects. This difference is minimal in terms of the differences subsequently observed. In this section, a description is given of a new comparative study with TOUTATIS and a version of PARMILA modified by Nicolas Pichoff of the French Atomic Energy Commission (CEA). One of the main modifications to the code is the implementation of the 3D PICNIC space charge routine to replace SCHEFF. It is necessary to use PARMILA to simulate the diagnostics.

5.5.1 Description of line

The proton beam is generated by a duoplasmatron source and extracted at 90 keV. The transport line consists of two solenoids used for injecting the beam into the RFQ (Figure 5.36). The proton beam thus matched enters RFQ2 and is raised from 90 keV to 750 keV (Table 5.24). Transmission is approximately 90%, as the entrance current is not known with accuracy, probably being between 220 and 230 mA of protons. The RFQ is monitored by the diagnostic line (see Table 5.25).

The principle of each measurement is described in detail in [15]. The authors consider that the systematic transfer data error is around 5%. No indications are given concerning longitudinal error.

5.5.2 Comparison of the results of simulation and measurement

Consideration is first given to the difference in the results for the RFQ exit given by PARMULT and TOUTATIS. Table 5.26 gives the exit parameters for each code. The differences are calculated using TOUTATIS for reference. The rms sizes are calculated and are used as the main

[10]Phase And Radial Motion in Ions Linear Accelerator.

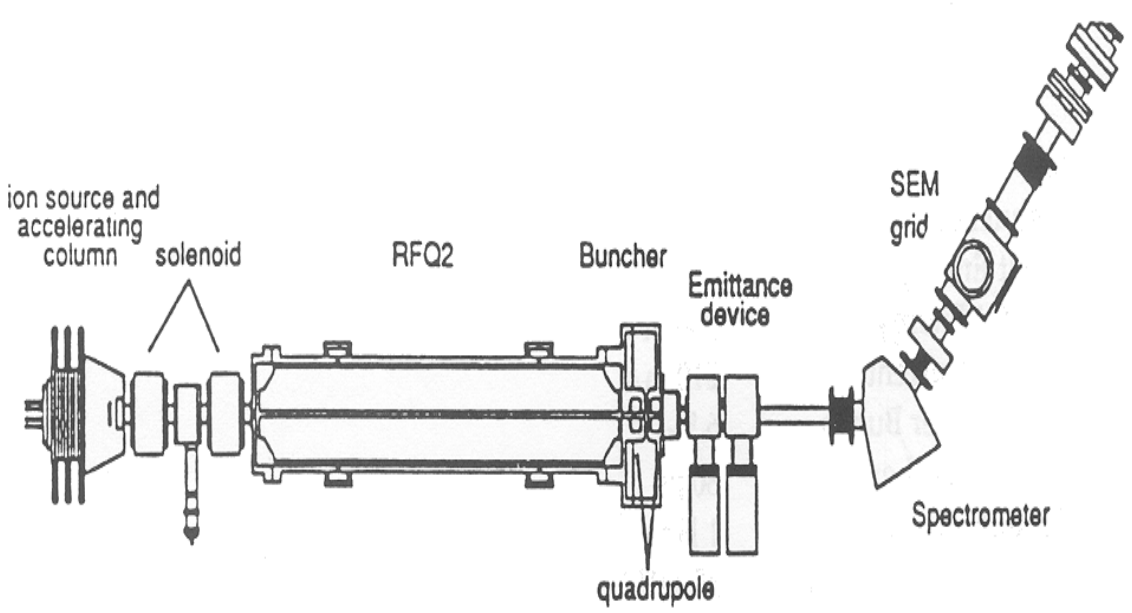

Figure 5.36: RFQ2 test bench.

Parameter	Value or type
Ion	H^+
Frequency	202.56 MHz
Entrance energy	90 keV
Exit energy	750 keV
Exit current	210 mA
Number of charges per bunch	$6.5 \cdot 10^9$
Pulse length	80 μs
Repetition rate	1 Hz
Peak field	35 MV/m (2.4 Kp)
Average gap	7.87 mm
Voltage	178 kV
Number of cells	126

Table 5.24: Main parameters of RFQ2.

Position	Element
z = 0 cm	End of RFQ poles
z = 5.5 cm	Entrance of Q10 quadrupole
z = 11.0 cm	Exit of Q10 quadrupole
z = 13.5 cm	Center of buncher
z = 15.5 cm	Entrance of Q20 quadrupole
z = 21.0 cm	Exit of Q20 quadrupole
z = 40.1 cm	Measuring slips

Table 5.25: Longitudinal positions of the different diagnostic line components.

	TOUTATIS	PARMULT	Difference (%)
α_x	-2.338	-2.787	-19.20
β_x (m/rad)	0.1819	0.1865	+2.53
$\varepsilon_{x,rms,norm.}$ (π..mm.mrad)	0.642	0.545	-15.11
$\widetilde{X}_{rms}$ (mm)	3.03	2.83	-6.60
α_y	2.758	2.771	+0.47
β_y (m/rad)	0.2509	0.2004	-20.13
$\varepsilon_{y,rms,norm.}$ (π..mm.mrad)	0.721	0.727	+0.83
$\widetilde{Y}_{rms}$ (mm)	3.77	3.39	-10.08
α_z	0.049	-0.214	-536.73
β_z (deg/MeV)	866	1592	+83.83
$\varepsilon_{z,rms,norm.}$ (deg.MeV)	0.174	0.126	-27.59

Table 5.26: RFQ2 exit beam parameters calculated with TOUTATIS and PARMULT.

criterion for estimating the quality of the simulations, as this is the parameter which is certainly the one most accurately measured.

It is noteworthy that the difference is 10% for the vertical size. On the basis of the TOUTATIS exit distribution, a number of PARMILA simulations were made for the three diagnostic line configurations. Tables 5.27, 5.28 and 5.29 give the measurements and values calculated with PARMULT+PARMILA and TOUTATIS+PARMILA for each of the configurations.

It has been verified that the two different versions of PARMILA do not give rise to differences relative to the results obtained by using the RMS parameters given by PARMULT as input for the version of PARMILA maintained by Nicolas Pichoff. The differences relative to measurements are of the same orders of magnitude: 22-23% difference for all parameters, 15-17% difference for sizes. The difference between the levels of performance of the two codes therefore results from the RFQ codes or the manner in which their exit distributions are used. The results in [15] were obtained using rms parameters and not the PARMULT exit distribution. To check whether this approximation was the cause of the differences, the instance of transport was recalculated with TOUTATIS and PARMILA but only using the rms parameters given by TOUTATIS for the exit. Table 5.30 gives a comparison of the results with the distribution and only the TOUTATIS

	Meas.	TOUTATIS+P	Difference (%)	PARMULT+P	Diff. (%)
α_x	-5.71	-7.140	25	-7.04	23
β_x (m/rad)	1.200	1.620	35	1.6	33
$\varepsilon_{x,rms,norm.}$ (π..mm.mrad)	0.720	0.780	8	0.74	3
$\widetilde{X}_{rms}$ (mm)	8.25	9.97	21	9.66	17
α_y	-1.300	-1.640	26	-2.3	77
β_y (m/rad)	1.100	1.160	5	1.2	9
$\varepsilon_{y,rms,norm.}$ (π..mm.mrad)	0.890	0.810	9	0.900	1
$\widetilde{Y}_{rms}$ (mm)	8.78	8.60	2	9.22	5
$\Delta\Phi$ (deg)	48	44	8	40	17
ΔW (MeV)	0.037	0.040	8	0.060	62
Average difference			15		22
Average difference for size			10		13

Table 5.27: Comparison between the results of simulation and measurement with the buncher on, G(Q10)=47.4 T/m and G(Q20)=28.7 T/m. P stands for PARMILA.

	Meas.	TOUTATIS+P	Difference (%)	PARMULT+P	Diff. (%)
α_x	-6.8	-5.27	23	-5.0	26
β_x (m/rad)	1.3	1.03	21	0.9	31
$\varepsilon_{x,rms,norm.}$ (π..mm.mrad)	0.62	0.82	32	0.68	10
$\widetilde{X}_{rms}$ (mm)	7.97	8.15	2	6.94	13
α_y	-1.8	-1.87	4	-2.3	28
β_y (m/rad)	1.2	1.11	7	1.7	42
$\varepsilon_{y,rms,norm.}$ (π..mm.mrad)	0.82	0.93	13	0.83	1
$\widetilde{Y}_{rms}$ (mm)	8.80	9.02	2	10.54	20
$\Delta\Phi$ (deg)	185	195	5	202	9
ΔW (MeV)	0.100	0.148	48	0.160	60
Average difference			16		24
Average difference for size			3		14

Table 5.28: Comparison between the results of simulation and measurement with the buncher off, G(Q10)= 46.7 T/m and G(Q20)= 21.9 T/m.

	Meas.	TOUTATIS+P	Difference (%)	PARMULT+P	Diff. (%)
α_x	-3.8	-2.82	26	-2.1	45
β_x (m/rad)	0.75	0.63	16	0.46	39
$\varepsilon_{x,rms,norm.}$ (π..mm.mrad)	0.70	0.76	9	0.67	4
$\widetilde{X}_{rms}$ (mm)	6.43	6.14	5	4.93	23
α_y	-2.6	-2.84	9	-3.6	38
β_y (m/rad)	1.5	1.45	3	2.1	40
$\varepsilon_{y,rms,norm.}$ (π..mm.mrad)	0.84	0.79	6	0.81	4
$\widetilde{Y}_{rms}$ (mm)	9.96	9.50	5	11.57	16
Average difference			10		26
Average difference for size			5		20

Table 5.29: Comparison of the results of simulation and measurement with the buncher off, G(Q10)= 42.6 T/m and G(Q20)= 19.6 T/m.

	Distribution	rms
Average difference	13%	13%
Average difference for size	6%	8%

Table 5.30: Comparison between the results of simulation and measurement for the three cases on average with and without conservation of TOUTATIS exit distribution (rms parameters only).

exit rms parameters. The differences are one order of magnitude lower than those observed in Tables 5.27, 5.28 and 5.29.. It can therefore be concluded that the difference in accuracy is due to the differences between the exit rms parameters given by the two codes. It is to be noted that the difference between the results given by TOUTATIS and the results of measurements are of the same order of magnitude as the uncertainty on the same measurements for the transverse direction. The case with the buncher still gives the greatest differences between the results of the codes and measurement. Should the reasons be sought between measurement or in the code? The authors of the measurement appear to be doubtful about their results in this case [16]. The question remains. Finally, it should be noted that the averages calculated are purely symbolic, as they are not statistically meaningful due to the small number of cases.

5.6 Conclusion of chapter

It has been shown that the approximations made in PARMTEQM for calculation of external fields, space charge, and image effects, for determination of losses and integration of the equations of movement all have substantial consequences in terms of dynamics. The amplitude of the errors depends on the RFQ but it negligible in standard cases. Although some of the approximations can easily be corrected, such as the paraxiality hypothesis, most are an integral part of the code, such as the analytical formulation for the fields, and the choice of z as independent parameter. Complete correction of the code would be an arduous if not impossible task.

If the defects resulting from these approximations were to be arranged in order of importance, the transverse loss criterion would probably be the first, followed by the paraxiality hypothesis. The defects resulting from the treatment of space charge and image effects would be secondary. This is due to the fact that, for the beam, focusing forces predominate. This is less true in a horizontal plane where space charge error results in substantial differences [17]. The code could therefore be substantially improved by eliminating the paraxiality hypothesis and the transverse loss criterion (square).

As concerns the validations of techniques used by the code, the method used for determining the radial matching section for a wide transverse wave number depression range and peak field estimation is particularly noteworthy.

Bibliography

[1] Vector Fields, TOSCA version 6.6, OPERA-3D reference manual version 2.5.

[2] K.R. Crandall, “Effects of vane-tip geometry on the electric fields in Radio-Frequency Quadrupole Linacs”, L.A.N.L. report LA-9695-MS, 1983.

[3] R. Duperrier et al., “Fields description in an RFQ and its effect on beam dynamics”, Linac 98 conference, Chicago.

[4] K.R. Crandall,“Computation of Charge Distribution On or Near Equipotential Surfaces”, L.A.N.L. report LA-3512 , December 1966.

[5] N. Tokuda, S. Yamada, “New Formulation of the Radial Matching Section”, Proceedings Linac conference 81, 19-23 October 1981, Santa Fe, LANL report LA-9234-C, 313 , February 1982.

[6] J.L. Laclare, A. Ropert, “The Saclay RFQ”, L.N.S. internal report 063, 1 June 1982.

[7] K.R. Crandall, “RFQ radial Matching Sections and fringe fields”, Proceedings Linac 84, p. 109, GSI-84-11.

[8] K. J. Sacherer, “RMS envelope equations with space charge”, Linac 84 conference, Darmstadt.

[9] C. Constancias, “Microtips field effect electron emitter simulation”, L.E.T.I. C.E.A. Grenoble, Département de Microtechnologie, France, XIII F.F. European User Group Meeting, San Margarita de Ligue, Italy.

[10] Suzanne C. Brenner, L. Ridgway Scott, “The mathematical theory of finite elements methods”, Springer-verlag New York Edition, 1994.

[11] R. Duperrier, “Calculs du champ électrique maximum dans une cellule RFQ”, report CEA/DSM/DAPNIA/SEA/IPHI/9843.

[12] “Effects of RFQ Vane-Tip Modulation on Local Resonant Frequency”, Los Alamos National Laboratory memorandum AT-1:82-68 to R. H. Stokes, 26 March 1982.

[13] A. Tkatchenko, “Mouvement d’une particule chargée dans un champ magnétique”, Large Instrument Technology and Physics post-graduate course, page 47.

[14] N. Pichoff, J.M. Lagniel, S. Nath, “Simulation results with an alternate 3D space charge routine, PICNIC”, MO4042, LINAC 1998 conference, Chicago.

[15] A. Lombardi, E. Tanke, T.P. Wangler , M. Weiss, “Beam dynamics of the CERN RFQ2 comparison of theory with beam measurements”, internal report CERN/PS93-13 (HI), March 1993.

[16] Private communication, by A. Lombardi.

[17] N. Pichoff, “Etude théorique et expérimentale du halo d’un faisceau intense de particules chargées dans un accélérateur”, Paris Sud Orsay University thesis, 11 December 1997.

Chapter 6

Additional developments

This chapter contains a review of the different developments for RFQ beam dynamics. Descriptions are given of the effects of radiofrequency coupling gaps on beam dynamics, a quick method for designing an RFQ, and a method for designing two consecutive RFQs. This last case is studied with a view to insertion of a high-speed beam chopper in the low-energy part of a high-intensity linac.

6.1 The effect of coupling gaps on dynamics

In relatively long RFQs (e.g. with a length of around 8 meters), the cavity is divided into a number of sections (Figure 6.1). This type of structure is commonly referred to as a “compensated structure”.. The main advantage of segmentation is longitudinal damping of any disturbances in the amplitude of the field along the cavity [1]. The limits of these segments are indicated by plates inserted into the structure at regular intervals[1].. At the boundaries of the segments, the four vanes are interrupted. The resulting gap is then adjusted to make the parasitic quadrupolar

[1] At 2-m intervals in the LEDA and IPHI of RFQs.

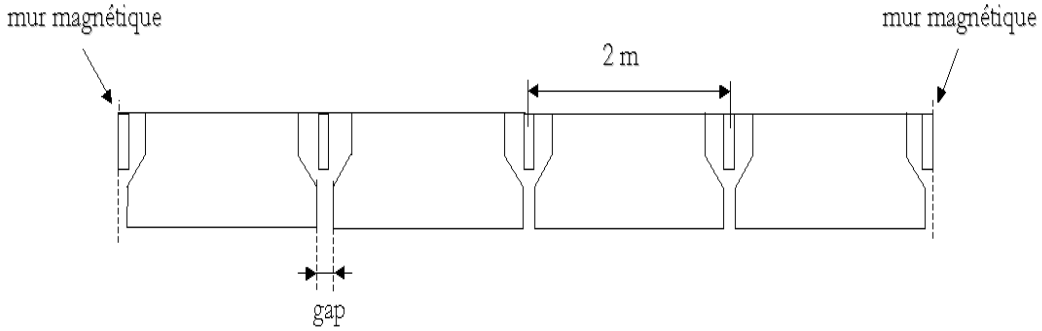

Figure 6.1: Diagram of RFQ segmentation.

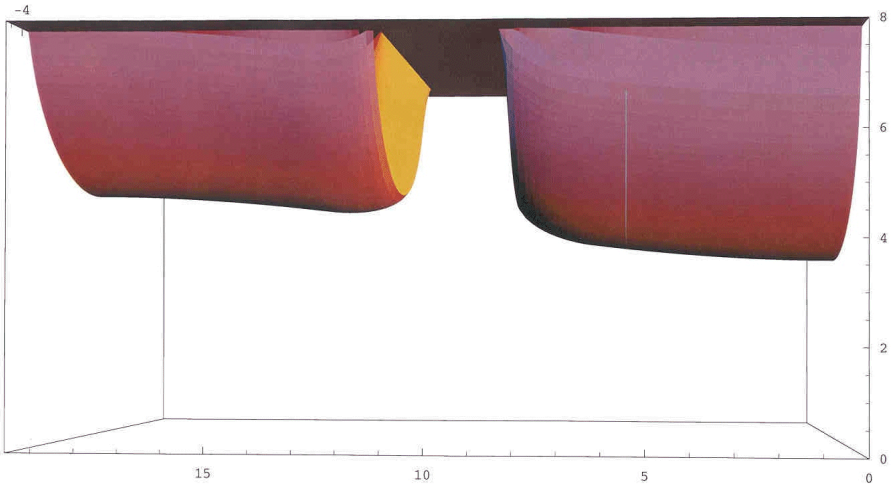

Figure 6.2: Profil of poles with radiofrequency coupling gap.

modes of the fundamental mode equidistant [2] (Figure 6.2).

The effect of interruption of the poles on the beam was unknown to the RFQ designers. To minimize the effect, Lloyd Young proposed situating the gap in an RFQ cell at a longitudinal position traversed by the synchronous particle at a moment when the amplitude of the alternating fields is nil [3]. To apply this concept to a specific cell, the position of the center of the gap is given by:

$$z = L_c \frac{\mid \phi_s \mid}{\pi} \tag{6.1}$$

where $z = 0$ at the beginning of the cell, L_c is the length of the cell, and ϕ_s is the synchronous phase at the center of the cell.

The equipotential surfaces resulting from such a geometry in the useful zone can be calculated numerically, and this geometry was implemented in the TOUTATIS code. Figures 6.3 and 6.4 show the potential distribution in a plane, with and without a coupling gap, respectively.

Another alternative for minimizing this effect simply consists in reducing the size of the gap without substantially degrading the quality of compensation of the structure. To determine the effect of the gaps depending on the configuration (Young's method, gap larger or smaller), an intermediate version of the IPHI project RFQ was simulated. Table 6.1 shows the various results. The cases marked with an asterisk indicate that Young's method was applied. The other cases correspond to a gap centered in the cell.

These simulations clearly show that coupling gaps cannot be disregarded when seeking to determine the dynamics of the beam in the IPHI and LEDA project RFQs. Combining the two methods results in the effect of the gaps on the dynamics being virtually nil in this case. For the IPHI project RFQ, it was initially planned to use 3.5 mm gaps located in the center of the cells, but they were subsequently positioned to allow for the synchronous phase and made 2.2 mm wide.

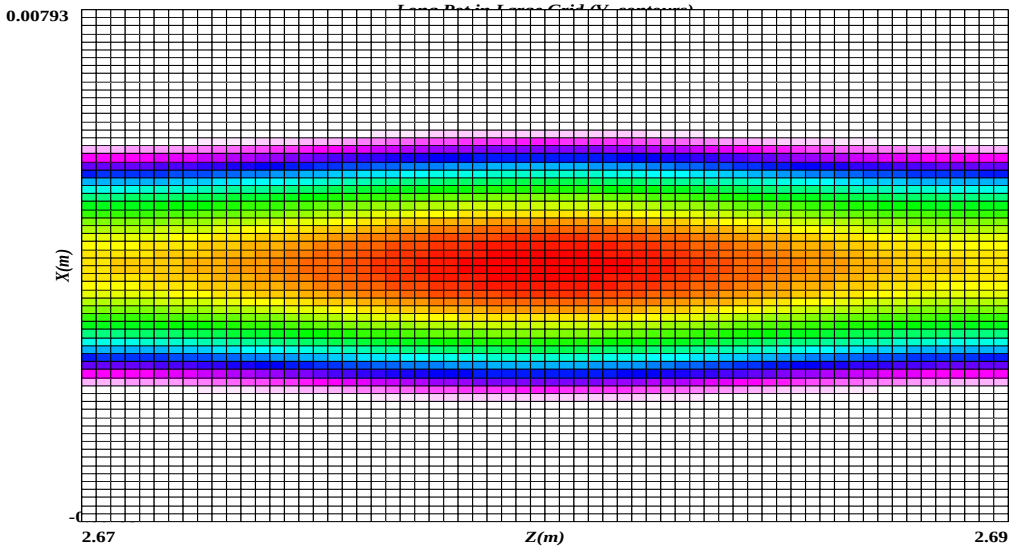

Figure 6.3: Distribution of potential in a plane with no coupling gap.

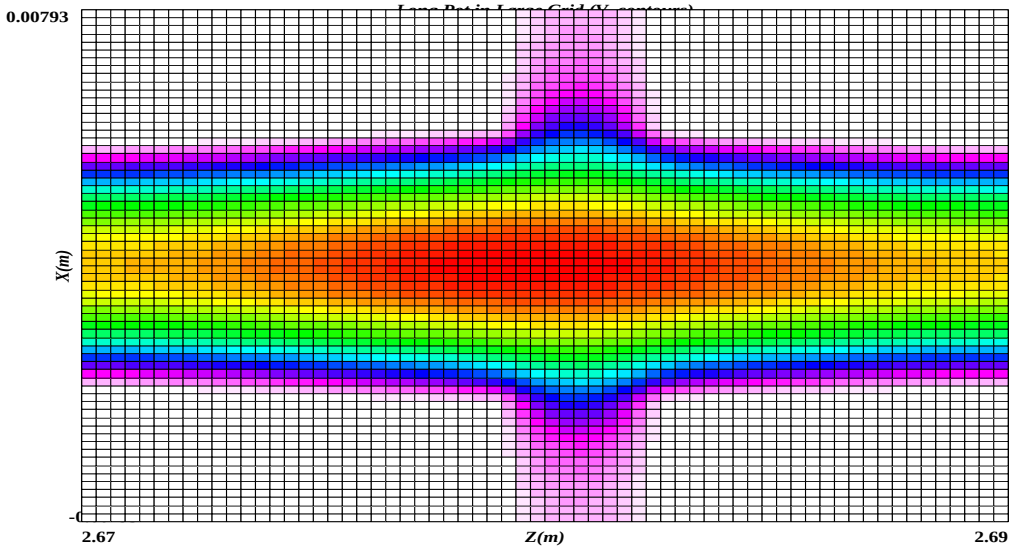

Figure 6.4: Distribution of potential in a plane with a coupling gap.

Gap width (mm)	$\emptyset$	3.5	2.2	3.5*	2.2*
$\widetilde{\varepsilon}_x$ (π..mm.mrad)	0.264	0.325	0.277	0.285	0.267
α_x	2.07	1.70	1.88	1.99	2.06
β_x (m.rad^{-1})	0.451	0.383	0.411	0.433	0.445
$\widetilde{\varepsilon}_y$ (π..mm.mrad)	0.259	0.325	0.278	0.283	0.266
α_y	-2.11	-1.95	-2.09	-1.94	-2.03
β_y (m.rad^{-1})	0.464	0.431	0.467	0.428	0.451
$\widetilde{\varepsilon}_z$ (deg.MeV)	0.156	0.182	0.162	0.174	0.159
α_z	-0.175	-0.132	-0.147	-0.162	-0.181
β_z(deg.MeV^{-1})	668	539	629	577	642
Transmission (%)	98.79	97.01	98.72	98.67	98.75
Yield (%)	96.89	94.95	96.79	96.53	96.76

Table 6.1: Results for different coupling gap configurations (width and position).

6.2 Design of an RFQ

The preceding chapters were concerned with a single issue: what is the best way of simulating an RFQ structure with known parameters? This begs another question, of equal importance: what parameters should be assigned to an RFQ structure to achieve the desired space charge regime beam acceleration and bunching functions? A number of possible solutions are to be found in the literature, combining a number of implementation criteria [4-8]. This section covers a simple method based on space charge upper-bound equations [9], making it possible to rapidly design an RFQ structure with acceptable performance.

6.2.1 Initial approximations

Consideration is only given to average effects on the beam. Therefore, rather than allowing for the alternating nature (i.e. focusing defocusing) of the external containment forces, use is made of an equivalent continuous focusing channel. These simplifications then reduce the parameters characterizing the size of the beam from three to two, as follows:

$$(\widehat{X}, \widehat{Y}, \widehat{Z}) \Rightarrow (\widehat{R}, \widehat{Z}) \tag{6.2}$$

where $\widehat{R}$ is the average radius of the beam and $\widehat{Z}$ the longitudinal half-size of the bunch. In an RFQ, the beam is initially continuous then in bunches, and being unable to precisely reflect this transition in an upper-bound equation, we continue to represent the beam as a uniformly charged ellipsoid with transverse symmetry of revolution, with the longitudinal half-size varying along the structure. In the model, it is assumed that longitudinal emittance remains nil. In reality, it is initially zero but increases along the RFQ. However, as shall be seen, this approximation gives good results, as space charge predominates in the longitudinal plane.

The rms upper-bound equations become:

$$\left\{ \begin{array}{rcl} \frac{d^2\widetilde{r}}{ds^2} + \frac{<rF_r>}{\gamma m(\beta c)^2 \widetilde{r}} - \frac{\widetilde{\varepsilon}_r^2}{\widetilde{r}^3} & = & 0 \\ \frac{d^2\widetilde{z}}{ds^2} + \frac{<zF_z>}{\gamma m(\beta c)^2 \widetilde{z}} & = & 0 \end{array} \right. \tag{6.3}$$

where m is the mass of the particle, γ and β are relativistic beam factors, c is the speed of light in a vacuum, and s is the longitudinal position of the bunch in the structure. The expression $< uF_u >$ means that the total force is linearized by integrating over the entire distribution. This includes the external forces and the space charge forces.

6.2.2 Calculation of forces

6.2.2.1 External forces

To simplify the calculations of $< uF_u >$, consideration is only given to the first term of the development representing E_r and E_z, i.e.:

$$\left\{ \begin{array}{rcl} F_r(r) & = & \frac{qV}{R_0^2} r \\ F_z(z) & = & qkVA_{10}\sin(kz) \end{array} \right. \tag{6.4}$$

where q is the charge of the ion, $k = 2\pi/\beta\lambda$, V is the inter-electrode voltage, R_0 is the average pole gap, and A_{10} is the weighting coefficient for modulation[2].. These forces are the average forces exerted on the bunch in its frame of reference (r, z).. To use the equations of movement (6.3), it is necessary to calculate the quantities $< uF_u >$, i.e.:

$$\begin{array}{rcl} < rF_r >_{ext} & = & \frac{2\pi \int_{-\widehat{Z}}^{\widehat{Z}} \int_0^{\widehat{R}\sqrt{1-(z/\widehat{Z})^2}} r \cdot \frac{qV}{R_0^2} r \cdot r\, dr\, dz}{2\pi \int_{-\widehat{Z}}^{\widehat{Z}} \int_0^{\widehat{R}\sqrt{1-(z/\widehat{Z})^2}} r\, dr\, dz} \\ & = & \frac{2}{5} q \frac{V}{R_0^2} \widehat{R}^2 \end{array} \tag{6.5}$$

and:

$$\begin{array}{rcl} < zF_z >_{ext} & = & \frac{2\pi \int_{-\widehat{Z}}^{\widehat{Z}} \int_0^{\widehat{R}\sqrt{1-(z/\widehat{Z})^2}} z \cdot qkVA_{10}\sin(kz) \cdot r\, dr\, dz}{2\pi \int_{-\widehat{Z}}^{\widehat{Z}} \int_0^{\widehat{R}\sqrt{1-(z/\widehat{Z})^2}} r\, dr\, dz} \\ & = & -\frac{3qVA_{10}\left[3k\widehat{Z}\cos(k\widehat{Z}) + (k^3\widehat{Z}^3 - 3)\sin(k\widehat{Z})\right]}{4k^3\widehat{Z}^3} \end{array} \tag{6.6}$$

[2]Note that the model was simplified by setting $A_{01} = 1$ for transverse focusing.

For convenience, these two forces can be re-written as follows:

$$\left\{ \begin{array}{lcl} < rF_r >_{ext} & = & \frac{V}{R_0^2}\hat{R}f(\hat{R}) \\ < zF_z >_{ext} & = & VA_{10}g(\hat{\varphi}) \end{array} \right. \tag{6.7}$$

where $\hat{\varphi} = k\hat{Z}$..

6.2.2.2 Space charge forces

Two cases require consideration: elongated ellipsoid ($\hat{R} < \hat{Z}$) and flattened ellipsoid ($\hat{R} > \hat{Z}$). The intermediate case (sphere) is unnecessary, as strict equality between $\hat{R}$ and $\hat{Z}$ is improbable. The fields, for such uniform charge density geometries, are given in the first volume of Emile Durand's book "Les distributions" published by Masson. The forces are calculated with integrals of type (6.6).

For the elongated ellipsoid:

$$< rF_r >_{ce} = \frac{3qI\lambda}{20c\pi\varepsilon_0(\hat{R}^2 - \hat{Z}^2)} \left\{ \frac{\hat{R}^2 \log \left[\frac{\sqrt{2\hat{Z}\left(\hat{Z}+\sqrt{\hat{Z}^2-\hat{R}^2}\right)-\hat{R}^2}}{\hat{R}^2} \right]}{\sqrt{\hat{Z}^2 - \hat{R}^2}} - \hat{Z} \right\} \tag{6.8}$$

and:

$$< zF_z >_{ce} = \frac{3qI\lambda\hat{Z}}{40c\pi\varepsilon_0(\hat{R}^2 - \hat{Z}^2)^{3/2}} \left\{ \hat{Z} \log \left[\frac{2\hat{Z}\left(\hat{Z} + \sqrt{\hat{Z}^2 - \hat{R}^2}\right) - \hat{R}^2}{\hat{R}^2} \right] - 2\sqrt{\hat{Z}^2 - \hat{R}^2} \right\} \tag{6.9}$$

For the flattened ellipsoid:

$$< rF_r >_{ce} = -\frac{3qI\lambda}{20c\pi\varepsilon_0(\hat{Z}^2 - \hat{R}^2)} \left\{ \frac{\hat{R}^2 \arctan \left[\frac{\sqrt{\hat{R}^2-\hat{Z}^2}}{\hat{Z}} \right]}{\sqrt{\hat{R}^2 - \hat{Z}^2}} - \hat{Z} \right\} \tag{6.10}$$

and:

$$< zF_z >_{ce} = \frac{3qI\lambda\hat{Z}}{20c\pi\varepsilon_0(\hat{Z}^2 - \hat{R}^2)} \left\{ \frac{\hat{Z} \arctan \left[\frac{\sqrt{\hat{R}^2-\hat{Z}^2}}{\hat{Z}} \right]}{\sqrt{\hat{R}^2 - \hat{Z}^2}} - 1 \right\} \tag{6.11}$$

where I is the beam current in amps and λ is the wavelength.

6.2.3 Parameter determination

The equations of movement are now complete. What remains is to determine the initial values of the parameters and their variation. The following criteria are therefore applied:

- To minimize the transverse losses, it is imposed that $\widehat{R} = cte$, i.e. $d_s^2\widehat{R} = 0$.. This constant is determined by matching the beam to the channel at the RFQ entrance defined by voltage and gap. This stage can be carried out by minimizing the envelope using the procedure described in the previous chapter.

- The channel is divided into two parts: one where the synchronous phase is maintained at -90* (high acceptance) for beam bunching, referred to as the *bunching zone* (ZG), and one where the synchronous phase is increased up to around -30* for acceleration of the bunch formed, which is referred to as the *acceleration zone* (ZA).

- Variation of the longitudinal half-size $\widehat{Z}(s)$ is imposed. It is in accordance with a function ranging from $\beta\lambda/2$ to the value desired in the bunching zone, and is made constant in the acceleration zone for as long as possible. The limit depends on criteria specific to the designer (maximum modulation etc.).

These different criteria simply reflect the desires of many RFQ designers. By replacing $\widehat{Z}(s)$ by the equivalent phase extension $\widehat{\varphi}(s)$, i.e.:

$$\widehat{\varphi}(s) = \widehat{Z}(s)\frac{2\pi}{\beta\lambda} = k\widehat{Z}(s) \tag{6.12}$$

and using the equivalence $\widehat{Z} = 5\widetilde{z}$ for an ellipsoid, the system defined by the expressions (6.3) becomes:

$$\begin{cases} \left(\frac{V}{R_0^2}\right)(s) & = & \frac{\widetilde{r}\gamma m(\beta c)^2}{f(\widehat{R})}\left(\frac{<rF_r>_{ce}}{\gamma m(\beta c)^2\widetilde{r}} + \frac{\widetilde{\varepsilon}_r^2}{\widetilde{r}^3}\right) \\ (VA_{10})(s) & = & \frac{\gamma m(\beta c)^2\widehat{\varphi}(s)}{5kg(\widehat{\varphi}(s))}\left(\frac{5k<zF_z>_{ce}}{\gamma m(\beta c)^2\widehat{\varphi}(s)} - \frac{\partial_s^2\widehat{\varphi}(s)}{k}\right) \end{cases} \tag{6.13}$$

even in the bunching zone where β is constant according to s.. For the acceleration zone, as the bunch is formed, it is chosen to conserve the constant focusing forces. This choice has two advantages: the first is that the bunch formed is maintained, the second is that modulation variation is given directly once the phase law is established. This is because, by maintaining the longitudinal focusing force constant during acceleration, it can be written that:

$$(VA_{10})(s) = (VA_{10})(l_{ZG})\frac{g\left(\frac{2\pi}{\beta(l_{ZG})\lambda}\widehat{Z}(l_{ZG})\right)}{g\left(\frac{2\pi}{\beta(s)\lambda}\widehat{Z}(l_{ZG})\right)} \tag{6.14}$$

where l_{ZG} is the length of the bunching zone.

Function $\beta(s)$ is completely determined by the phase law as the energy zone per cell is equal to:

$$\Delta W(s) = q\frac{\pi}{4}(VA_{10})(s)\cos(\Phi_S(s)) \tag{6.15}$$

where $(VA_{10})(s)$ varies sufficiently slowly for it to be possible to take the value calculated for the preceding cell as being that of the cell in question [4].. The process is noteworthy: from $(VA_{10})\,(l_{ZG})$, the value obtained at the end of the bunching zone and $\Phi_S > -90$* implies a gain for $\beta(s)$ and hence a gain for $(VA_{10})\,(s)$ via expression (6.14) etc. The modulation increases "on its own account" through acceleration and vice-versa. To avoid excessive modulation resulting in an excessive decrease in a, the minimum gap, the designer can set a ceiling on modulation. This second option, however, implies an increase in the longitudinal size of the bunch.

The same principle can be used for the synchronous phase law, $\Phi_S(s)$.. Phase acceptance, $\Delta\Psi$, of the linac is given by the expression [4]:

$$\tan(\Phi_S) = \frac{\sin(\Delta\Psi) - \Delta\Psi}{1 - \cos(\Delta\Psi)} \tag{6.16}$$

For the bunch to be stable, the following conditions must be met:

$$2\widehat{\varphi}(s) < \Delta\Psi \tag{6.17}$$

This condition links acceptance to velocity if it is wished to maintain the longitudinal dimension of the bunch. Variation of $\Delta\Psi$ along the structure becomes:

$$\Delta\Psi(s) = 2\pi\frac{\beta_0}{\beta(s)} \tag{6.18}$$

where β_0 is the structure entrance value. The value of $\Phi_S(s)$ can be obtained directly by means of expression (6.16). It is necessary to introduce a certain margin as acceptance is not symmetrical relative to Φ_S.. To obtain this margin at equivalent acceleration, the synchronous phase can be modified by means of the expression:

$$(\Phi_S)_f = -\arccos\left(\frac{(\Phi_S)_i}{\alpha}\right) \tag{6.19}$$

The values of α of around 1.1 are typically acceptable. As α increases, the margin increases but the RFQ will be longer for the same final energy.

To complete and finalize the method, it should also be noted that if the synchronous phase, at the end of the bunching zone, is not arbitrarily incremented, the process of "self-augmentation" of the synchronous phase, modulation and velocity does not begin. This increment is set at the initiative of the designer. It would appear that a linear increase of 5* over around ten cells is acceptable.

6.2.4 Adiabaticity criterion

The model, as it has been described, leaves the designer free to choose the length of the bunching zone. However, it must not be too short, as there would be a risk of introducing an excessively fast disturbance accompanied by an irreversible increase in the "transverse" emittance of the system, "transverse" as the longitudinal emittance can only increase in the zone. A criterion for the rate of variation of the amplitude of the transverse focusing forces is therefore necessary. In the case of expansion of a gas in a piston, the process is termed adiabatic if the speed of the piston is small compared to the speed of sound in the gas. In other words, the external forces must vary more slowly than the forces of interaction in the system [10]. The dynamics of the medium then correspond to a succession of states of equilibrium and entropy does not increase. In the present case, the forces of interaction are the space charge forces. The distance of relaxation of the beam in the space charge regime, l, is:

$$l \approx \frac{l_0/4}{1-\eta_r} = \mu\beta\lambda \tag{6.20}$$

where l_0 is the length of the betatron wave and η_r is the wave number depression due to space charge [11]. The constant μ can express this distance as a fraction of the spatial period of focusing. It must therefore be ascertained that the variation in the force applied is negligible over this distance. Rather than the total force, we take the ratio between the space charge force and the radial containment force, χ, for simplification:

$$\chi(s) \propto \frac{< rF_r >_{ce}}{< rF_r >_{ext}} \tag{6.21}$$

For 60* phase advance and 100 mA, the distance necessary for establishing equilibrium is of a few meshes. More generally, to meet this criterion, assuming that the variation is infinitesimal over a spatial period, χ must comply with the following condition:

$$\Lambda(\chi) < \varepsilon \tag{6.22}$$

by writing:

$$\Lambda = \mu\beta\lambda\frac{1}{\chi}\frac{\partial\chi}{\partial s} \tag{6.23}$$

where ε is of the order of a few 10^{-2}.. After a number of tests, it would appear that this order of magnitude for ε constitutes a good compromise. Imposing a lower value improves the quality of the channel but makes the bunching zone longer.

6.2.5 Transition to real beam

6.2.5.1 Transverse equivalence

As the RFQ channel is not a continuous focusing channel but focuses and defocuses alternately in a plane, it is necessary to establish equivalences for transposing the model to reality. For the two channels to be equivalent, phase advance of the particles must be identical over one FD channel period. The FD channel forces are modulated by $\sin(\omega t)$, i.e. $\sin(ks+\varphi)$ where φ is the phase of the particle at the moment when it enters the channel. In a continuous focusing channel, the trajectory of particles in a uniform beam can be modeled with the relationship:

$$R_c(s) = R\sin\left(\frac{2\pi}{l}s\right) \tag{6.24}$$

where l is the length of the betatron wave and R the maximum amplitude of oscillation of the particle. If l is large compared to $\beta\lambda$, which is all the more true as space charge is large, the average of $\widehat{F_r}r$ for one period is:

$$\begin{aligned} \overline{F_r} &= \tfrac{1}{\beta\lambda}\int_0^{\beta\lambda}\widehat{F_r}\cdot R_c(s)ds \\ &\simeq \widehat{F_r}\cdot R_c(\beta\lambda/2) \end{aligned} \tag{6.25}$$

where $\widehat{F_r}$ is the force gradient. For the periodic focusing channel, the trajectory of a particle, with the same phase advance as that corresponding to (6.24), is:

$$R_p(s) = R\sin\left(\frac{2\pi}{l}s\right)\cdot[1+\delta\sin(ks)] \tag{6.26}$$

where the trajectory is modulated by a small amplitude δ.. This modulation has the same period as the focusing forces and corresponds to modulation of the beam envelope. Calculation of $R_p(s)\cdot\widehat{F_x}$ then becomes somewhat more complicated:

$$\begin{aligned} \overline{F_x} &= \tfrac{1}{\beta\lambda}\int_0^{\beta\lambda}\widehat{F_x}\sin(ks+\varphi)\cdot R_p(s)ds \\ &\simeq \widehat{F_x}\cdot R_c(\beta\lambda/2)\tfrac{\delta}{2} \end{aligned} \tag{6.27}$$

With the result that, for the channels to be equivalent, the amplitude of the periodic focusing forces must comply with the expression:

$$\widehat{F_x} = \frac{2}{\delta}\widehat{F_r} \tag{6.28}$$

The $2/\delta$ factor typically amounts to around 20. This value has to be calculated during FD channel matching. For equivalences in terms of size, the technique consists of making $\widehat{X}$ equal to $\widehat{R}$..

Parameter	Value or type
Ion	H^+
Frequency	352.2 MHz
Entrance energy	95 keV
Current	100 mA
Average gap	4.13 mm
Voltage	100 kV
Number of cells for matching	6
Total emittance normalized on X (4D Water Bag)	1.5π..mm.rad
Total emittance normalized on X (Uniform) equivalent	1.0π..mm.rad
Total emittance normalized to the radial (Uniform) equivalent	2.0π..mm.rad
Wave number depression	0.67
μ	4.5

Table 6.2: Initial parameters of RFQ.

6.2.5.2 Longitudinal equivalence

The amplitude of the longitudinal focusing forces is modulated by the radiofrequency beat and the geometry of the vanes. These two amplitude modulations give a variation of the following type:

$$F_z \propto \sin(ks)\sin(\omega t) = \sin^2(ks) \tag{6.29}$$

With the result that, on average, the force is twice as small as that obtained in Section 6.2.2, the average of $\sin^2(x)$ over one period being equal to $1/2$.. It is therefore necessary to multiply expression (6.13) by 2 to obtain the longitudinal force to be applied.

6.2.6 Illustration of the method for a specific case

To illustrate the method, initial parameters typical of an RFQ for high current with the parameters indicated in Table 6.2 are considered. The search for parameters matching the entry of the structure gives a value of 1.5 mm for $\widehat{R}$ and 20 for $2/\delta$..

The analytical function chosen to impose grouping is:

$$\widehat{\varphi}(s) = 180 - 50 \times \left[1 - \cos\left(\frac{\pi}{l_{ZG}}s\right)\right] \tag{6.30}$$

which makes it possible to impose a phase reduction of 180* to 80* for the half-size. The resulting radial $(V/R_0^2)(s)$ and longitudinal $(VA_{10})(s)$ functions are calculated with expressions

$\widetilde{\varepsilon}_{x,n.}/\widetilde{\varepsilon}_{0,n.}$	$\widetilde{\varepsilon}_{y,n.}/\widetilde{\varepsilon}_{0,n.}$	$\widetilde{\varepsilon}_{z,n.}$(deg.MeV)	Yield	Transmission
1.07	1.08	0.145	99.98%	99.98%

Table 6.3: Enlargement of normalized rms transverse emittance, longitudinal emittance, yield and total transmission.

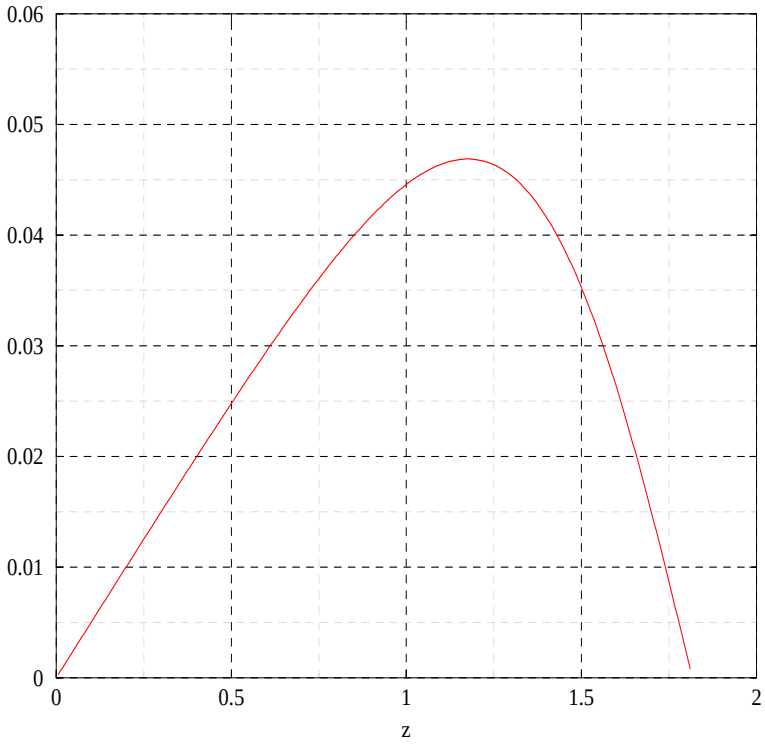

Figure 6.5: Variation in Λ along the bunching zone.

(6.13). To minimize the peak field, R_0 is constant over an initial section of the RFQ then diminishes (see Chapter 3). The voltage varies in such a manner as to comply with $(V/R_0^2)(s)$ via $R_0(s)$.. For the acceleration zone, modulation is limited to 1.7 and the synchronous phase is increased by -33*. The constant α, required for calculation of the phase law, is taken to be equal to 1.1. Other choices could have been made for these values. It is a matter of finding a compromise in terms of other constraints, such as the length of the RFQ, the peak field, or sensitivity to radiofrequency power reduction. The set of parameters selected gives an RFQ length of 6.35 m and a peak field greater than 42 MV/m (i.e. 2.3 times the Kilpatrick field). A number of parameters of the structure are described in Figures 6.5 to 6.9.. Table 6.3 summarizes the performance of the RFQ obtained. Figure 6.10 shows the variation in the beam envelope. Different exit distributions are described in Figures 6.11 and 6.12.. One interesting aspect of the method is that the structure obtained has no high-energy losses (Figure 6.13).

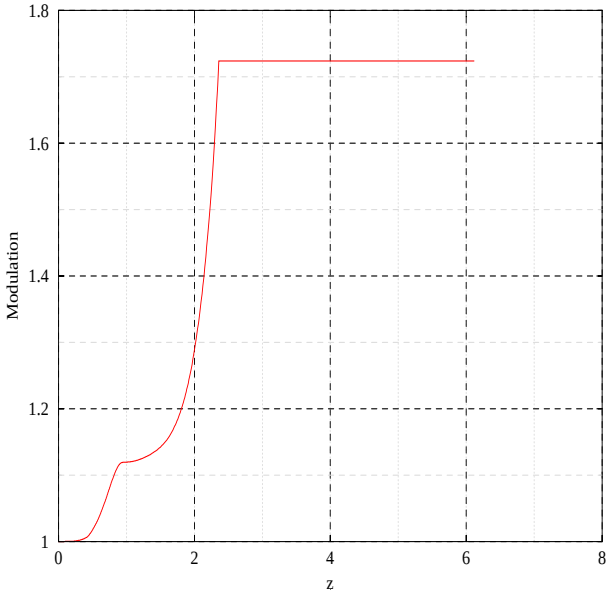

Figure 6.6: Variation in the modulation along the RFQ. The first variation is derived from the bunching zone model, the second from the acceleration zone model with a ceiling of 1.7.

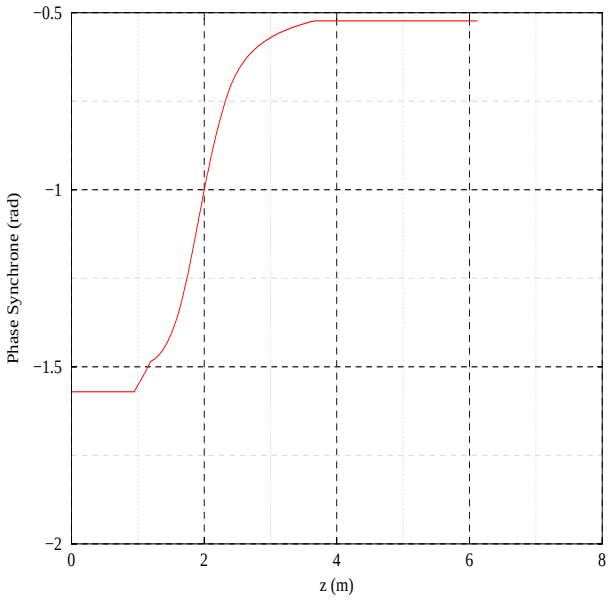

Figure 6.7: Variation in synchronous phase along the RFQ.

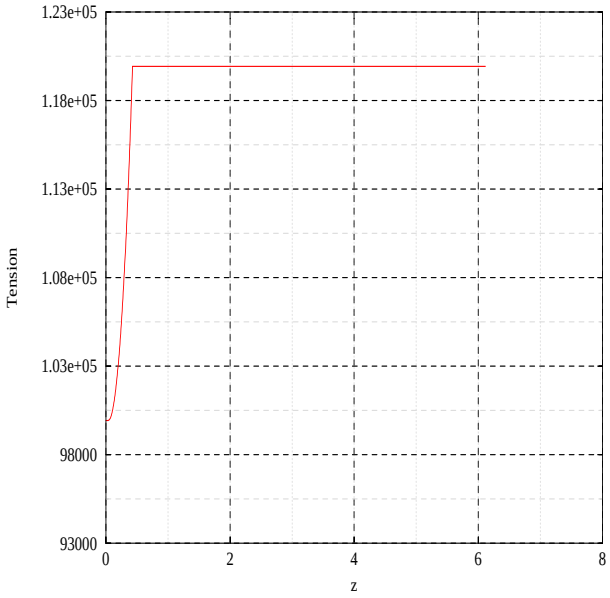

Figure 6.8: Variation in voltage along the RFQ. Augmentation only occurs in the bunching zone.

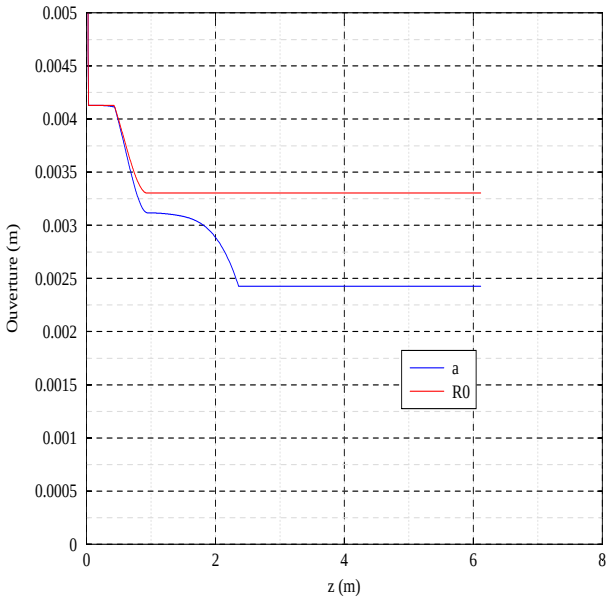

Figure 6.9: Variation in R_0 and a along the RFQ.

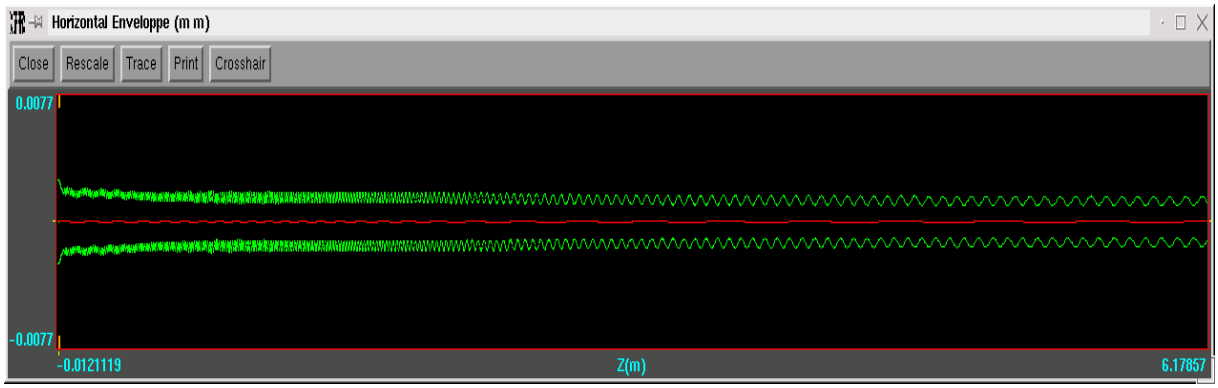

Figure 6.10: Variation in beam horizontal envelope. This envelope shows the importance of limiting the longitudinal focusing force while keeping the transverse force constant in the acceleration zone. High-energy losses are minimized by the gradual reduction in transfer size that results.

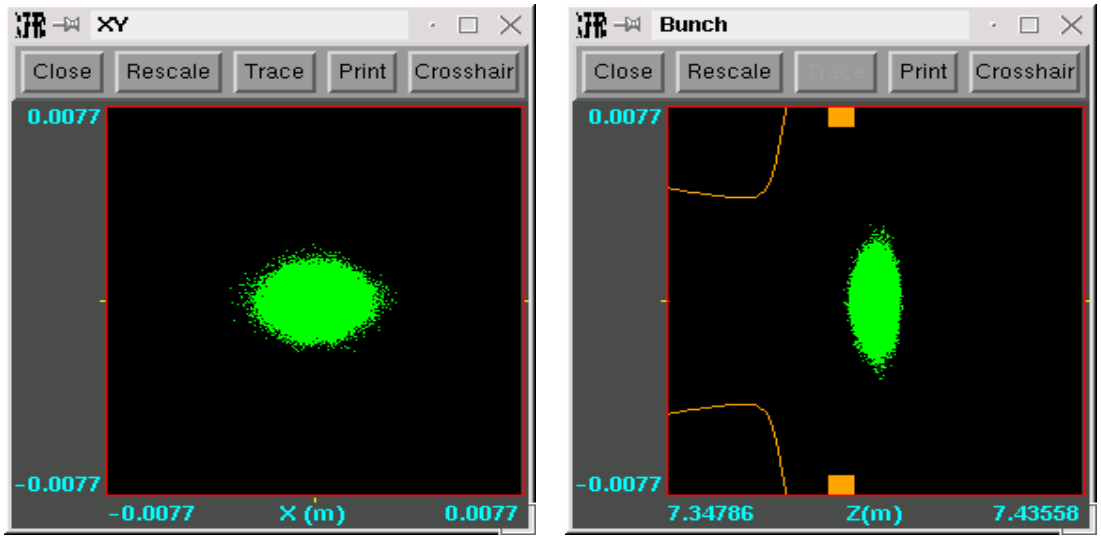

Figure 6.11: 6.12 Front and side view of bunch at RFQ exit. The geometry is effectively that of an ellipsoid, which shows that the particles are mainly subjected to linear forces, making the model used coherent.

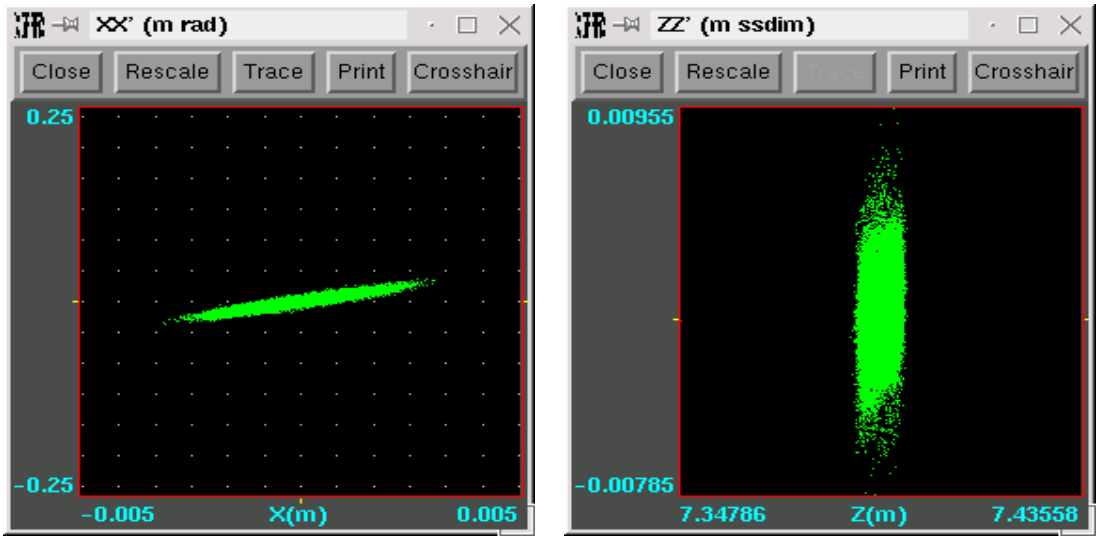

Figure 6.12: Bunch distribution in transverse XX' and longitudinal ZZ' phase domains at RFQ exit.

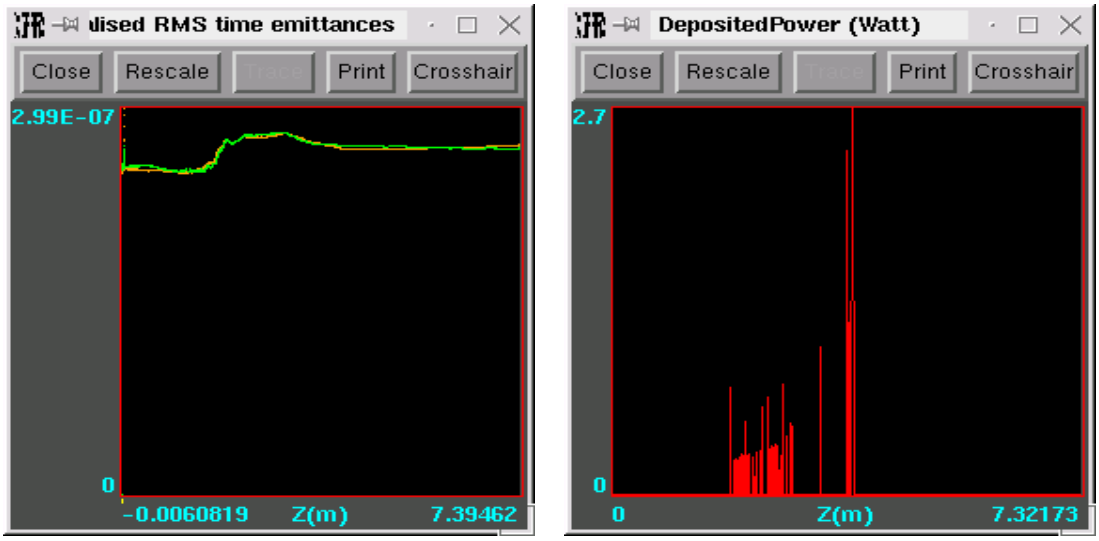

Figure 6.13: Variation in the two transverse emittances and power deposition in watts along the RFQ. No particles with energies higher than 2 MeV are lost, corresponding to the activation threshold of copper.

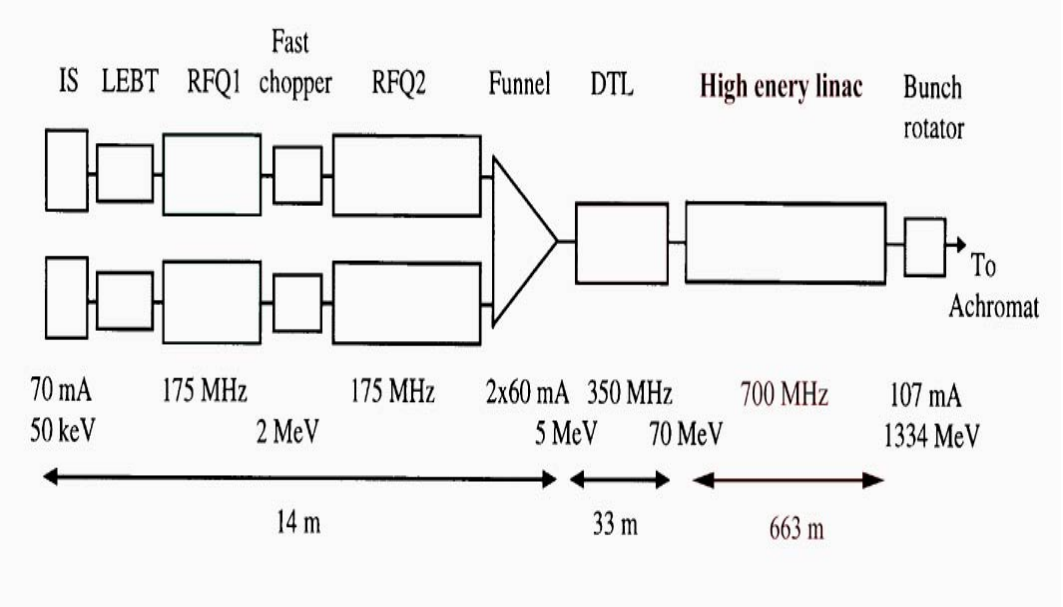

Figure 6.14: Diagram of ESS project linac with its low-energy section (2 RFQs + chopper).

6.3 Design of two RFQs

For a number of high power accelerator projects (European Spallation Source, Spallation Neutron Source and European Polyvalent Machine[3]), it is necessary to chop the beam to enable injection into a storage ring. This operation is carried out by a chopper at an energy of around 2 MeV. The low-energy part obtained is then similar to an RFQ of the IPHI type divided into two to enable insertion of the chopper (Figure 6.14).

To design such a line from the point of view of the dynamics in the RFQ, a possible method is to only finally optimize a single structure, choose a cut-off point, place a transition cell followed by an exit section at the end of the first RFQ and an entrance section followed by a transition cell making it possible to ensure continuity with the entrance modulation of the second one. Matching beam parameters for the second RFQ can be obtained by inverse transport by injecting, somewhat upstream, the matching bunch taken during simulation of the large initialized RFQ (Figure 6.15).

To allow a degree of flexibility in implementation of transport in the chopper line, it is helpful to vary the length of the exit sections of the first RFQ and the entrance section of the second one (Figure 6.16). Figures 6.17 to 6.21 show the Twiss parameters, for each plane, as a function of these lengths for the first of the two RFQs currently being designed at Saclay for the ESS project. Figure 6.19 clearly shows that variations in emittance are negligible and that inverse transport is therefore valid.

[3]These would have a number of applications: spallation neutrons, production of radioactive ions, waste treatment etc.

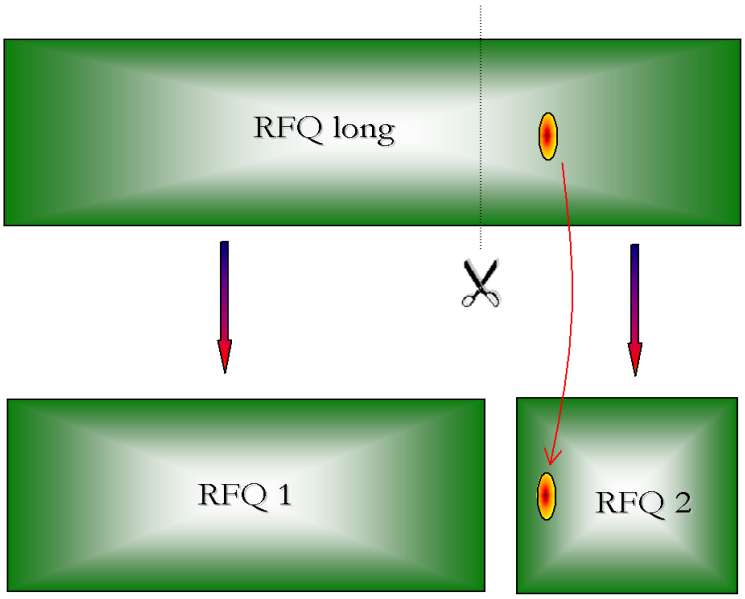

Figure 6.15: Diagram illustrating the method of designing two RFQs.

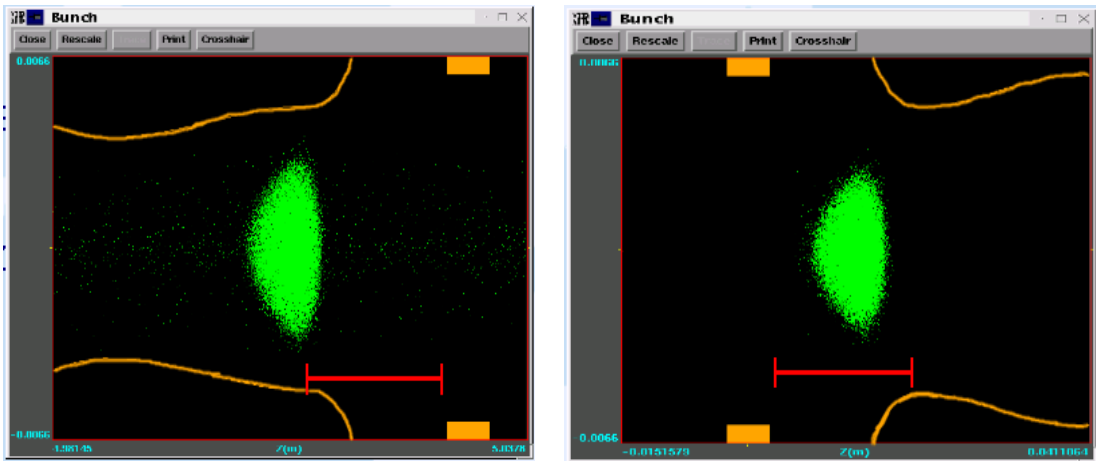

Figure 6.16: Diagram showing the distances (red segments) to be varied to obtain a set of matching beam parameters offering flexibility in implementation of the chopper line.

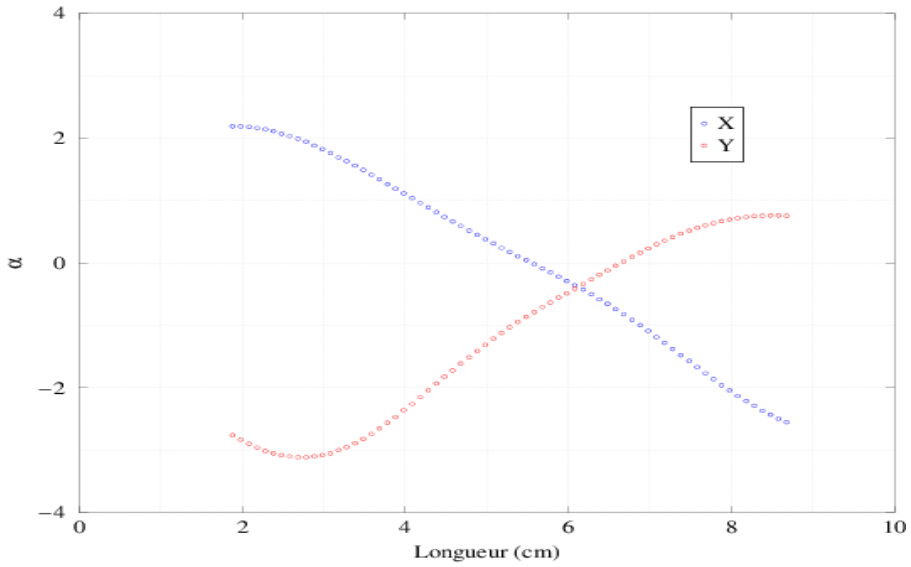

Figure 6.17: Variation in matched α for each transverse plane.

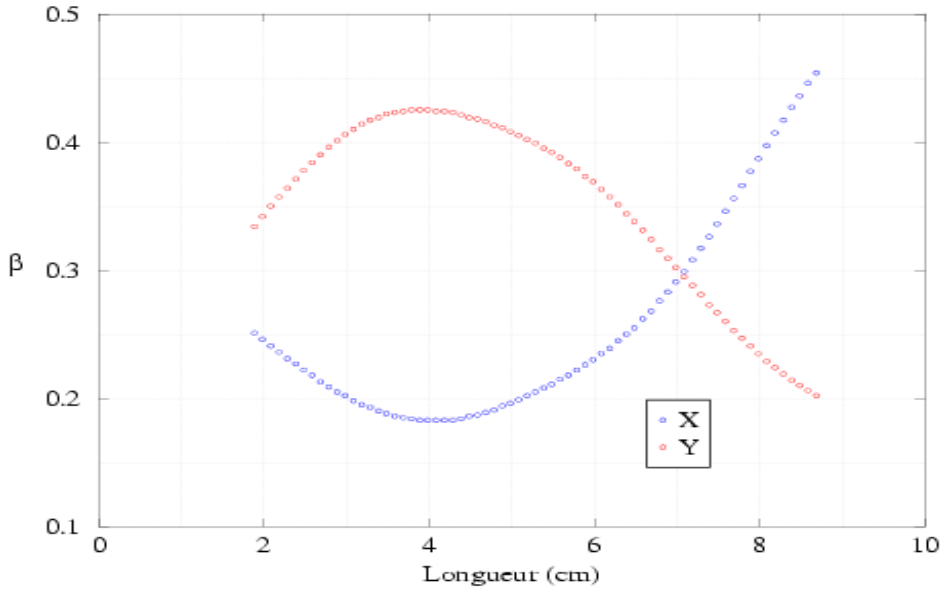

Figure 6.18: Variation in matched β for each transverse plane.

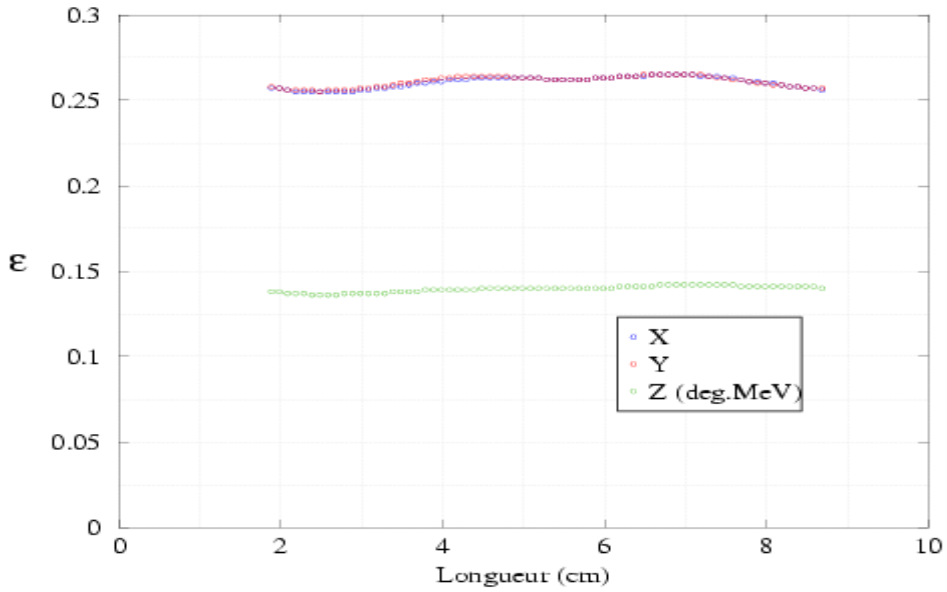

Figure 6.19: Variation in emittances in each plane.

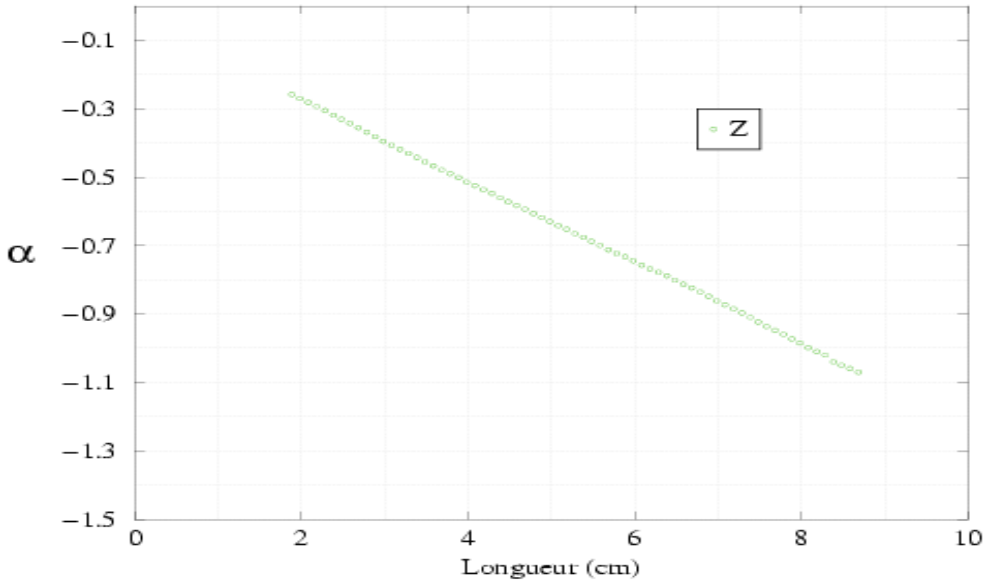

Figure 6.20: Variation in matched α for the longitudinal plane.

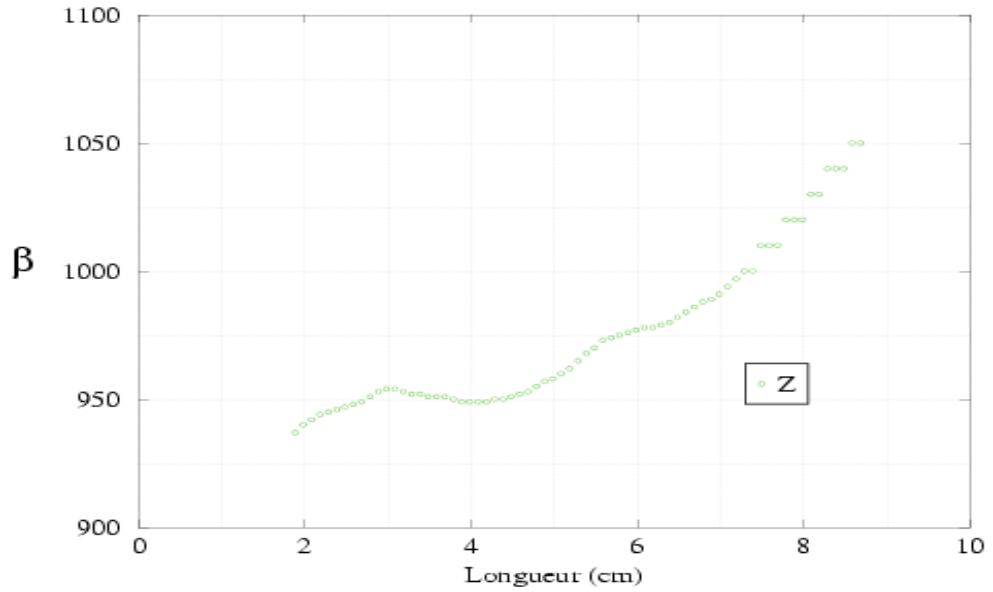

Figure 6.21: Variation in matched β for the longitudinal plane.

6.4 Conclusion of chapter

This chapter shows how to estimate the impact of radiofrequency coupling gaps on particle dynamics. To make their effect negligible, it is necessary to reduce the width of the gaps as much as possible and to position them in the cell with allowance for the synchronous phase.

A quick and simple method of designing an RFQ is described. This mainly stems from the desire to keep the dimensions of the bunch obtained in the bunching zone as constant as possible. The bunching zone is designed on the basis of beam envelope equations in a channel equivalent to the RFQ.

A simple manner of apprehending the design of two RFQs for projects such as ESS, SNS and the European Polyvalent Machine is described in detail. Indications are given concerning flexibility in the development of a chopper line to be placed between the two RFQs.

Bibliography

[1] Lloyd Young, “Segmented Resonant Coupled Radio Frequency Quadrupole (RFQ)”, Proceedings PAC 1993, Washington, D.C..

[2] P. Balleyguier, “Dimensionnement des gaps de couplage du RFQ d’I.P.H.I.”, report CEA/DIF/DPTA/SP2A n*147:99, 22 September 1999.

[3] Private communication by Lloyd Young, Robin Ferdinand.

[4] K. R. Crandall, R. H. Stokes, T. P. Wangler, “RF Quadrupole Beam Dynamics Design Studies”, Linac 1979.

[5] R. Ferdinand et al., “Optimization of RFQ Design”, THP23G, EPAC 1998 conference, Stockholm, June 1998.

[6] J.-M. Lagniel, “Tools for the design of high-current linacs”, LINAC 1994 conference.

[7] C. Biscari, M. Weiss, “Choice of parameters for the CERN high intensity RFQ (RFQ2 project)”, LINAC 1984 conference, Darmstadt.

[8] “Multilevel Codes RFQ.3L for RFQ Designing”, rencontres groupe accélérateurs IFMIF, Workshop, Paris, 26-30 May 1997.

[9] Frank J. Sacherer, “RMS envelope equations with space charge”, IEEE trans. Nucl. Sci. NS-18, 1105 (1971).

[10] L. Landau, E. Lifchitz, ”Physique statistique”, MIR publications, Moscow 1967.

[11] N. Pichoff, “Etude théorique et expérimentale du halo d’un faisceau intense de particules chargées dans un accélérateur”, Paris Sud Orsay University thesis, 11 December 1997.

Chapter 7

General conclusion

The basic principles of an RFQ have been reviewed, and consideration has been given to the state-of-the-art concerning description of the useful zone on the basis of subdivision into cylindrical harmonics. The principles of time/position matching have also been described.

The hypotheses adopted for simplification in the PARMTEQM code have been covered in detail. In terms of present-day requirements for high-current RFQs, these simplifications raise a number of issues: do they cause any error and, if so, what is their relative importance in terms of transmission, exit beam distribution and the location of losses? To find answers to these problems, a new transport code has been written to minimize the simplification hypotheses and serve as a reference for a number of comparative studies. This code is based on solving of the Poisson equation in three-dimensional grids. It uses time as the independent parameter for integration of movement, with allowance for the geometry of the poles, space charge forces and image effects.

These studies show that the approximations made in PARMTEQM for the calculation of external fields, space charge and image effects, for the treatment of losses and integration of the equations of movement all have consequences for dynamics. The amplitude of the errors depends on the RFQ, with the result that many of the approximations may be acceptable in a number of cases. Although some approximations can easily be corrected, such as the paraxiality hypothesis, most are integral parts of the code, such as the analytical formulation of the fields, and the choice of z as the independent parameter. Point-by-point correction of the code would be arduous if not impossible.

If the errors resulting from these approximations were to be classified in order of importance, the transverse loss criterion would probably come first, followed by the paraxiality hypothesis. The errors resulting from space charge treatment and image effects remain secondary in most cases. This is because focusing forces predominate. This is less true in the horizontal plane where space charge considerations can give rise to substantial error. This mode could, however, be substantially improved by eliminating the paraxiality hypothesis and its criterion for transverse losses (square twice the minimum gap of a side).

As concerns validation of the code, the method used for determining the radial matching section for a wide range of wave number depression in the transverse direction and estimation of the peak field is noteworthy.

The last chapter covers estimation of the impact of the radiofrequency coupling gaps on particle dynamics. To minimize their effect, it is necessary to make them as small as possible and to position them in the cell with allowance for the synchronous phase.

A simple and rapid method of designing an RFQ is given. The model is based on conservation of the bunch dimensions obtained at the end of the bunching zone. The bunching zone is designed using the space charge regime beam envelope equations in a channel equivalent to the RFQ.

A simple way of apprehending the design of two RFQs for projects such as ESS, SNS and the European Polyvalent Machine is described in detail. This is accompanied by indications offering a degree of flexibility for integration of the chopper line to be placed between the two RFQs.

Future work could include improvement of the TOUTATIS code, with Taylor developments of up to the fourth order in the finite differences method. It might then be possible to achieve the same precision with a smaller number of nodes. The method developed for design of the RFQ is relatively recent and a number of improvements are necessary, such as control of the peak field.

Appendix A

General information on harmonics[1]

A.1 The Dirichlet problem

Electrical potential results from the presence of charges in space. If we consider space in general, including the infinite, there is no function complying with the Laplace equation. In such a case, the Poisson equation applies:

$$\Delta\Psi = \rho \tag{A.1}$$

where ρ is a function of space representing the charge density per unit volume (i.e. the spatial distribution of the sources). But if limited portions of space are considered, solutions to equation (2.4) can be found, and this is a problem that continuously recurs. Sources are assumed to reside somewhere outside the domain in question. It is then required to find a solution in a domain Ω, using given values for the boundary Γ of the domain:

$$\Delta\Psi = 0 \text{ in } \Omega \text{ and } \Psi \text{ given } \Gamma$$

This is the *Dirichlet problem*.. If the domain is a volume limited by a closed surface (three-dimensional case, for the two-dimensional case it would be a closed curve), it is an *internal problem*.. If the domain is outside the closed surface (closed curve for the 2D case) and extends to infinity, it is an *external problem*.. The first case, which is the most frequent, is considered in this appendix.

A.2 The Sturm-Liouville problem

If the Laplace equation is described in a system of coordinates (u, v, w) and if solutions with separated variables are required, i.e.:

$$\Psi(u, v, w) = \Xi(u) \cdot \Theta(v) \cdot \Phi(w) \tag{A.2}$$

[1] This appendix describes a number of methods for representation of the scalar potential on the basis of harmonics as described in [1].

By substituting expression (A.2) into equation (2.4), three distinct differential equations are obtained of the following type:

$$\frac{d}{dw}\left[f(w)\frac{d\Phi(w)}{dw}\right] + \left[g(w) + \nu \cdot h(w)\right]\Phi(w) = 0 \quad a < w < b \tag{A.3}$$

where ν is an arbitrary constant, and a and b, are the boundaries of the domain in direction w.. The Sturm-Liouville problem consists of finding solutions to (A.3) which, at boundaries a and b, satisfy the homogenous linear conditions:

$$\begin{cases} A \cdot \Phi(a) + A^{'} \cdot \partial_w \Phi(a) = 0 \\ B \cdot \Phi(b) + B^{'} \cdot \partial_w \Phi(b) = 0 \end{cases} \tag{A.4}$$

where A, $A^{'}$, B, $B^{'}$are arbitrary constants and $\partial_w \Phi(w)$ is the derivative of $\Phi(w)$ relative to w.. When the interval $[a, b]$ is bounded, the conditions can only be satisfied if constant ν has well-determined values ν_k referred to as characteristic values [1]. For each value ν_k, there is a corresponding function $\Phi_k(w)$, referred to as the characteristic function (i.e. harmonics). A general solution to the Laplace equation can be written as follows:

$$\Psi(u, v, w) = \sum_l \sum_m A_{lm} \cdot \Xi_l(u) \cdot \Theta_m(v) \cdot \Phi_{lm}(w) \tag{A.5}$$

It is now required to determine coefficients A_{lm}; this is the subject of the following section. To conclude the last two sections, it is important to note that the characteristic functions $\Phi_k(w)$ are valid for representing a potential, solving the Laplace equation within a bounded domain.

A.3 Methods for determining series coefficients

A.3.1 Projection onto an orthonormal base in the domain

For a function $F(u)$ to be represented by a development of the following type:

$$F(u) = \sum_k A_k \cdot \Phi_k(u) \tag{A.6}$$

with:

$$\int_a^b \Phi_k^\star(w)\Phi_j(w)dw = \delta_{jk} \tag{A.7}$$

where δ_{jk} is the Kronecker symbol[2], the function must be of a square that can be integrated into the interval $a < u < b$.. The coefficients are then given by projection (i.e. scalar product):

$$A_k = \int_a^b \Phi_k^\star(u) \cdot F(u) \cdot du \tag{A.8}$$

[2]This expression is termed the closure relationship.

Under these conditions, the average quadratic error:

$$\varepsilon_N = \int_a^b \left| F(u) - \sum_{k=1}^{N} A_k \cdot \Phi_k(u) \right|^2 du \tag{A.9}$$

is minimized [1].

A.3.2 Methods with non-orthonormal base

Although it is, in principle, always possible to orthogonalize a set of functions, it can be an arduous task for complicated domains or even simple ones. The method is more a game for mathematicians! Here it is shown that, under these conditions, the coefficients are not calculated independently of each other, as closure relationships cannot be used. However, other methods are available for finding them and solving the system of linear equations. Here we briefly consider three: the Galerkine method, the direct method and the least square method (*fit*).

A.3.2.1 Galerkine method

Let us assume that it is still desired to represent function $F(u)$ in a domain Ω with a finite development of order N:

$$F(u) = \sum_{k=0}^{N} A_k \cdot \Phi_k(u) \tag{A.10}$$

but that, this time, the base is not orthogonal in Ω.. Coefficients A_k are therefore calculated separately. It is necessary to find the relationships between the coefficients. We therefore consider new coefficients B_l and C_{kl} such that:

$$\begin{cases} B_l = \oint_C \Phi_l^\star(M) \cdot F(M) \cdot dl \\ \\ C_{kl} = \oint_C \Phi_l^\star(M) \cdot \Phi_k(M) \cdot dl \end{cases} \tag{A.11}$$

where M is a point on closed curve C bounding domain Ω[3].. Equation (A.10), multiplied by $\Phi_l^\star$ and integrated, becomes:

$$\sum_{k=0}^{n=N} A_k \cdot C_{kl} = B_m \tag{A.12}$$

This is the relationship sought. All that remains is to solve $(N+1)$ equations to determine the $(N+1)$ coefficients A_k.. This method has the advantage of avoiding orthogonalizing the base used in the domain considered, but necessitates calculating a large number of integrals which, for domains with complicated bounds, is particularly arduous, if not impractical. If we are willing

[3]Curve for the two-dimensional case, three-dimensional surface.

to solve a system of linear equations, there is a more simple and effective method: the direct method.

A.3.2.2 Direct method

The solution approached is still in the following form:

$$F(u) = \sum_{k=0}^{N} A_k \cdot \Phi_k(u) \tag{A.13}$$

If $(N+1)$ values of $F(u)$ are known at points M_l, a system of $(N+1)$ equations can be written to determine the $(N+1)$ coefficients A_k:

$$F(M_l) = \sum_{k=0}^{N} A_k \cdot \Phi_k(M_l) \tag{A.14}$$

$(N+1)$ points for M_l must be judiciously selected to improve the quality of the method. This method is by far the most effective and the simplest for determining the series coefficients. However, it has the disadvantage that, for each coefficient required, a value must be previously known. It is possible to avoid this problem by using the least square method.

A.3.2.3 Least square method

This is the most popular method. It is used in a substantial number of numerical programs [2]. It consists of minimizing the quantity:

$$\varepsilon = \sum_{l=1}^{P} \left[F(M_l) - \sum_{k=0}^{N} A_k \cdot \Phi_k(M_l) \right]^2 \tag{A.15}$$

which can be considered as the sum of the least squares provided by the representation of $F(u)$ by the base on points M_l.. It is therefore necessary to know P values of $F(u)$, but P can be smaller than N.. It is in this that the advantage of the method resides: the number of known points is independent of the number of coefficients sought. The method is, however, more effective if the number of points is high. To make the quantity ε a minimum, it is necessary to find coefficients A_k complying with the $(N+1)$ equations of following type:

$$\frac{\partial \varepsilon}{\partial A_k} = \frac{\partial}{\partial A_k} \sum_{l=1}^{P} \left[F(M_l) - \sum_{k=0}^{N} A_k \cdot \Phi_k(M_l) \right]^2 = 0 \tag{A.16}$$

The final solution obtained cannot be used to accurately determine the values used, contrary to the direct method, but makes it possible to obtain a solution if only few points in the domain are known.

Bibliography

[1] E. Durand, “Electrostatique", Masson & Cie, 1966, Volume II.

[2] S. Wolfram, Mathematica 3.0, Cambridge University Press, 1996.

Appendix B

RFQ vane geometry

To simplify the analysis, the usual practice is to only consider the first two harmonics of each series of the equation (2.18). The expression for electrical potential is then reduced to:

$$\Psi(\rho,\theta,z) = \frac{V}{2}\left\{X\left(\frac{\rho}{R_0}\right)^2\cos(2\theta) + A\cdot I_0(k\rho)\cos(kz)\right\} \tag{B.1}$$

with:

$$A = \frac{m^2-1}{m^2 I_0(ka) + I_0(mka)} \tag{B.2}$$

and:

$$X = 1 - AI_0(ka) \tag{B.3}$$

to meet the following boundary conditions:

$$\Psi(a,0,0) = \Psi(ma,0,L_c) = \frac{V}{2}$$

and:

$$\Psi(ma,\frac{\pi}{2},0) = \Psi(a,\frac{\pi}{2},L_c) = -\frac{V}{2}$$

This simplified potential can be used to determine a number of quantities characteristic of the dynamics in an RFQ, which is extremely useful for designing the structure (calculation of phase advances etc.). As this simplified potential has the same disadvantages as that with eight terms as concerns machining of the poles, it is at least possible to seek to equalize the radii of longitudinal and transverse curvature of the pole and the equipotential surface corresponding to equation (B.1). For the horizontal pole, the variation in the normalized transverse radius of curvature ρ_t/R_0 is given by the following expression:

$$\frac{\rho_t}{R_0} = \frac{\alpha}{R_0}\left(\frac{\frac{2\alpha}{R_0}+\beta}{\frac{2\alpha}{R_0}-\beta}\right) \tag{B.4}$$

where $\alpha = x$ (abscissa of end of pole) and:

$$\beta = AkR_0\cos(kz)I_1(k\alpha) \tag{B.5}$$

The trajectory followed by α can be obtained by dichotomy by varying z.. The minimum value of the radius of longitudinal curvature is reached when $x = ma$, and its amplitude amounts to:

$$\frac{\rho_l(ma,0,L_c)}{R_0} = \frac{\frac{2ma}{R_0} - AkR_0I_1(mka)}{Ak^2R_0^2I_0(mka)} \tag{B.6}$$

This is effectively the minimum that is suitable for machining. The radius of the cutter must be smaller than ρ_l.. These values were tabulated for different characteristics of cells by Ken Crandall[1].. This has two implications for short cells (typically for L_c/R_0 between 0.75 and 2):

- the peak field is considerably increased,
- machining is difficult.

To overcome these problems, Crandall suggests making the radius of transverse curvature constant, the optimum value being around $0.75 \times R_0$.. Another advantage is that the inter-vane capacity is then virtually constant along the gap [2].. Crandall also proposes to apply modulation of the sinusoidal type, rather than that derived from equation (B.1) while maintaining the radius of transverse curvature constant. The radius of longitudinal curvature, in $x = ma$, is then:

$$\frac{\rho_t(ma,0,L_c)}{R_0} = \frac{m+1}{(m-1)k^2R_0^2} \tag{B.7}$$

Cutter dimensions can therefore be increased for short cells. In conclusion, consideration is to be given to two types of longitudinal profiles: a sinusoidal profile and a profile extrapolated from the simplified potential with two terms, the transverse section being circular with constant radius of curvature for vane type RFQs.

Bibliography

[1] K.R. Crandall, “Effects of vane-tip geometry on the electric fields in Radio-Frequency Quadrupole Linacs”, L.A.N.L. report LA-9695-MS, 1983.

[2] K.R. Crandall, “Effect of RFQ Vane-Tip Modulation on Local Resonant Frequency”, Los Alamos National Laboratory memorandum AT-1:82-68, 26 March 1982.

Appendix C

Procedure for obtaining A and B

(A = average envelope, B = modulation of average envelope)

It is desired to minimize the expression (5.13) with respect to A, hence:

$$\frac{\partial}{\partial A}\sum_{i=0}^{N}\left\{\widehat{X}_i - [A + BC(z_i)]\right\}^2 = 0 \tag{C.1}$$

with:

$$C(z_i) = \cos\left(\frac{2\pi z_i}{\beta\lambda_{rf}} + \varphi_{rf}\right) \tag{C.2}$$

By derivation, expression (C.1) can be re-written as:

$$\begin{aligned}\textstyle\sum_{i=0}^{N}\widehat{X}_i &= \textstyle\sum_{i=0}^{N}A + \sum_{i=0}^{N}BC(z_i)\\ &= NA + B\textstyle\sum_{i=0}^{N}C(z_i)\end{aligned} \tag{C.3}$$

Similarly, for B:

$$\frac{\partial}{\partial B}\sum_{i=0}^{N}\left\{\widehat{X}_i - [A + BC(z_i)]\right\}^2 = 0 \tag{C.4}$$

giving:

$$\sum_{i=0}^{N}\widehat{X}_i C(z_i) = A\sum_{i=0}^{N}C(z_i) + B\sum_{i=0}^{N}C(z_i)^2 \tag{C.5}$$

It is therefore necessary to solve the following system with two unknowns:

$$\begin{pmatrix} N & \sum_{i=0}^{N}C(z_i) \\ \sum_{i=0}^{N}C(z_i) & \sum_{i=0}^{N}C(z_i)^2 \end{pmatrix}\begin{pmatrix} A \\ B \end{pmatrix} = \begin{pmatrix} \sum_{i=0}^{N}\widehat{X}_i \\ \sum_{i=0}^{N}\widehat{X}_i C(z_i) \end{pmatrix} \tag{C.6}$$

finally:

$$\begin{pmatrix} A \\ B \end{pmatrix} = \frac{1}{\Delta} \begin{pmatrix} \sum_{i=0}^{N} C(z_i)^2 & -\sum_{i=0}^{N} C(z_i) \\ -\sum_{i=0}^{N} C(z_i) & N \end{pmatrix} \begin{pmatrix} \sum_{i=0}^{N} \widehat{X}_i \\ \sum_{i=0}^{N} \widehat{X}_i C(z_i) \end{pmatrix} \tag{C.7}$$

with:

$$\Delta = N \sum_{i=0}^{N} C(z_i)^2 - \left[\sum_{i=0}^{N} C(z_i) \right]^2$$

Appendix D

Analytical model for chamfer [1]

D.1 Introduction

Considerable progress has been made in computer technology over the last ten years, and it is now possible to study complex electromagnetic phenomena with codes based on the finite element method, such as the TOSCA program [1].. This has made it possible to design magnets for accelerators with extreme precision, with the result that error of around 10^{-5} relative to the ideal field can be anticipated. In some projects, such levels of performance are becoming necessary for certain projects. For the SOLEIL project, the tolerance limits for the magnets are of a few 10^{-4} [2].. Magnets can now be designed to achieve such precision, making it possible to avoid the phase of shimming[2] resulting from the multipolar components that are always detected during the measuring stage.

Control of the multipolar content is also properly mastered during 2D calculations. But the three-dimensional stage has been found to be far more difficult. To prevent the pole finishing at angles to the direction of the beam, the designer cuts the end bit by bit. Several attempts have been made to obtain a consistent model for chamfer design. Langenbeck and Francsak have obtained good results thereby [3].. But the geometry obtained was difficult and costly to machine. Their model also induced transverse-longitudinal coupling which is detrimental to particle dynamics. In most cases, the designers make do with a 45° chamfer or with multiple facets as a refinement [4, 5].. In this article, it is proposed to build electromagnets with a pole end profile that considerably reduces the amplitude of the multipolar components. This profile is based on a specific solution to the Laplace equation. The geometry indicated by the model also has the advantage of being easily machinable.

[1] This appendix is the translation of an article published in IEEE Transactions On Magnetics in March 2000. This task, which is outside the scope of the thesis, was inspired by a study made of the radial matching section of the RFQ. I would like to thank Olivier DelferriËre and Denis de Menezes for making the different simulations, which required an enormous amount of work.

[2] This stage consists of assembling the pieces of magnetic material, which is generally of small size, at the poles of the magnet, to correct the multipolar content.

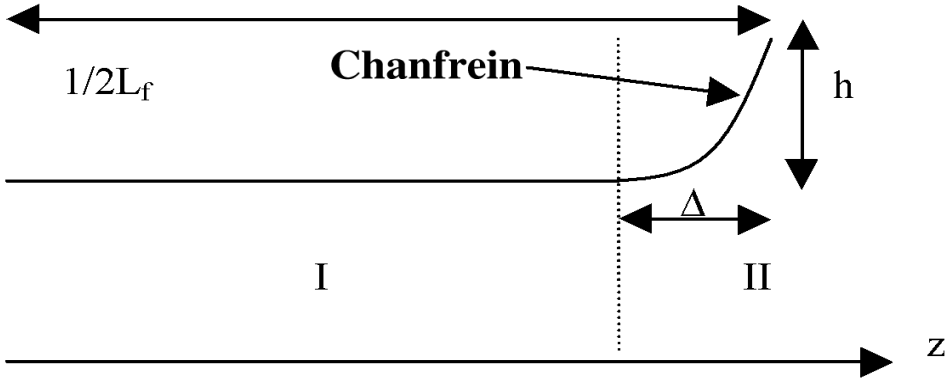

Figure D.1: Longitudinal profile of center at end of magnet.

D.2 Analytical model and simulation tools

D.2.1 Analytical solutions for the Laplace equation

The usual manner of describing the magnetic channel for the transport of charged particles is to use the following 2D series for scalar potential:

$$V(r,\theta) = \sum_n r^n \left[a_n \cos(n\theta) + b_n \sin(n\theta)\right] \tag{D.1}$$

the magnetic field is then simply obtained by applying the divergence operator:

$$\overrightarrow{B} = -\overrightarrow{\nabla(V)} \tag{D.2}$$

In practice, magnets are not of infinite length, which makes it necessary to introduce azimuthal components. To obtain a full representation of the field and ensure proper continuity between the central region (I) and the end of the magnet (II) (Figure D.1), we propose to use the following series [6, 7]:

$$V(r,\theta,z) = (az+b)\sum_n r^n \left[a_n \cos(n\theta) + b_n \sin(n\theta)\right] \tag{D.3}$$

It is also postulated that the discontinuity induced by B_z is negligible. By writing the preceding equation for a single multipole of order n and using iron length L_f and magnetic length L_m, we obtain a formula which describes the longitudinal profile for the chamfer:

$$r(z) = d\left(\frac{\Delta}{\frac{1}{2}L_f - z}\right)^{1/n} \tag{D.4}$$

where d is the minimum distance between the axis and the pole, and Δ is the distance over which the chamfer operates. The formula is all the more effective when the multipolar content of the central region is poor. It is shown below that this approximation gives good results.

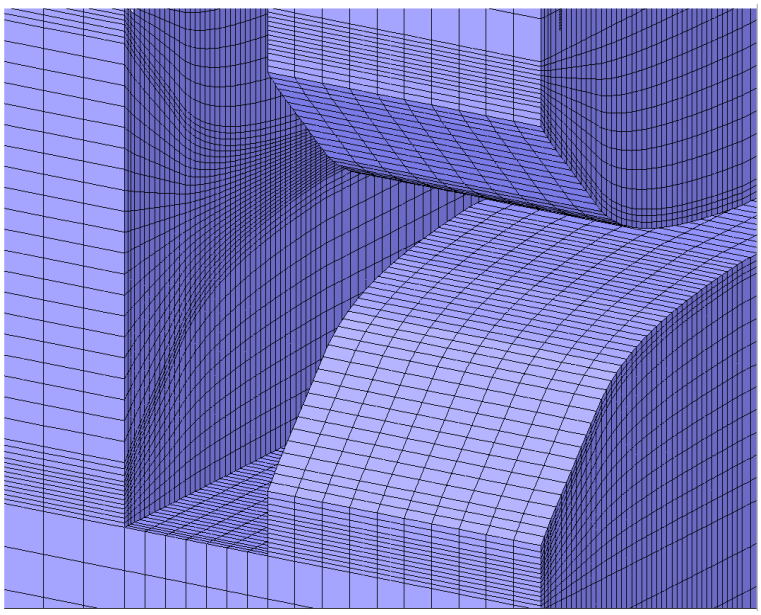

Figure D.2: Typical dipole profile.

D.2.2 Simulation tools

D.2.2.1 Mesh generation

The different models were made using the TOSCA code which uses the finite element method. A number of implementations of the code have been developed at CEA Saclay, making it possible for us to rapidly obtain geometries with chamfer management (Figure D.2).

Once meshed, the models were fed to the solver. The calculations were carried out on a HP-J282 workstation, with 512 Mb of RAM. The CPU time necessary for making the 15 non-linear iterations (saturation) was approximately 15 hours with around 450,000 nodes, to ensure a high level of precision.

D.2.2.2 Processing of results and harmonic analysis

The multipolar tolerances given for transport were calculated by integrating the magnetic field along z. We therefore used the same criterion in our simulations. The components were projected onto base (D.1) to remain coherent with the orbit calculations. The projection was made on the lateral surface of a cylinder with a radius equal to half the gap for the dipole and the groove radius for the quadrupole. The integral was made from -∞ to +∞ (actually from -L to +L, with L sufficiently great).

We began the procedure with the following 2D magnetic scalar potential:

$$V(r,\theta) = \sum_{n}^{n} \alpha_n r^n \sin(n\theta) \tag{D.5}$$

By projecting the central region potential calculated with TOSCA, we obtained component α_n:

$$\alpha_n = \frac{1}{\pi r^n} \int_0^{2\pi} V_T(r,\theta) \sin(n\theta) d\theta \tag{D.6}$$

We defined the integrated harmonic component A_n as:

$$A_n = \frac{1}{2\pi L r^n} \int_{-L}^{+L} \int_0^{2\pi} V_T(r,\theta,z) \sin(n\theta) d\theta dz \tag{D.7}$$

where V_T was the solution calculated with TOSCA. From equation (D.2), we obtained the harmonic coefficient for the radial component of field B_r:

$$\alpha_n = \frac{1}{\pi r^{n-1}} \int_0^{2\pi} (B_r(r,\theta))_T \sin(n\theta) d\theta \tag{D.8}$$

and hence the integrated term:

$$A'_n = \frac{1}{2\pi L r^{n-1}} \int_{-L}^{+L} \int_0^{2\pi} (B_r(r,\theta,z))_T \sin(n\theta) d\theta dz \tag{D.9}$$

Still in agreement with the orbit calculations, we normalized all the terms by magnetic length L_m:

$$\frac{\int_{-L}^{+L} \int_0^{2\pi} (B_r(r,\theta,z))_T \sin(p\theta) d\theta dz}{\int_0^{2\pi} (B_r(r,\theta,0))_T \sin(p\theta) d\theta} = L_m \tag{D.10}$$

where p was the order of the harmonic (p =1 for the dipole, p = 2 for the quadrupole etc.).

Automatic procedures were written in OPERA-3D for calculating the integrals of area A'_n for n=1 to n=20 [8].. The following sections describe comparison between the multipolar content of a dipole and a quadrupole with different profiles characterized by depth Δ (see Section D.2.1). In theory, chamfer height h (Figure D.1), is infinite in accordance with formula (D.4) but, for obvious feasibility reasons, we chose to make h_0<h , taking care to make the vertical plane tangential to the end of the chamfer. All the simulations were also compared with the no-chamfer case (i.e. square edge). Each profile was described by ten facets.

D.3 Application to dipole

D.3.1 Description of magnet

The dipole tested had a right “C” transverse profile corresponding to the SOLEIL ring design, with a few simplifications to facilitate construction. The length was 1 meter and the air gap 37 mm with a nominal field of 1.56 T (Figure D.3). The lateral chamfers were deleted for simplification.

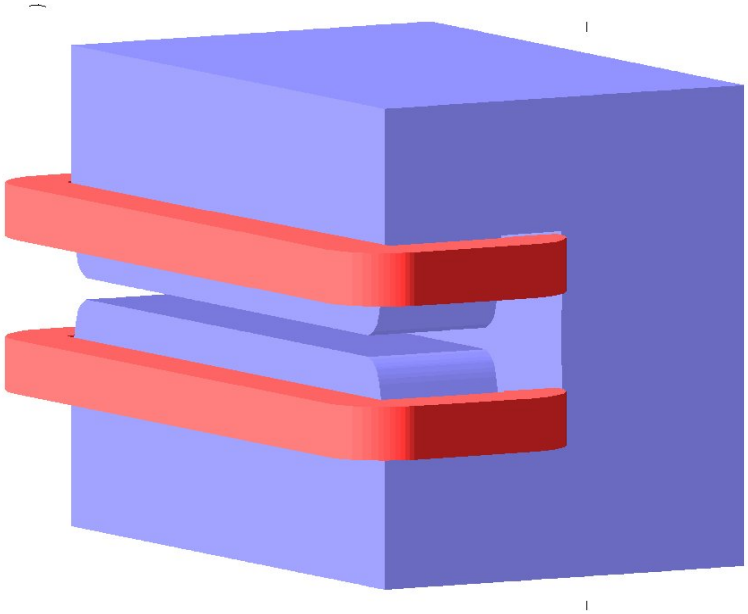

Figure D.3: Complete geometry of dipole with conductors.

D.3.2 Profile

>From the equation (D.4), we derived the following expression for the dipole profile in region II where g was half the gap:

$$r(z) = g\frac{\Delta}{\frac{1}{2}L_f - z} \tag{D.11}$$

Depth Δ was a function of the integral of the magnetic field required by the dynamics of the beam $B_{dyn}L_m$ (where B_{dyn} was the value of the fields, assumed to be constant). By applying what was imposed, i.e. L_f=L_m, the function can be written as follows:

$$\Delta = L_f\left(1 - \frac{B_{dyn}g}{\mu_0 NI}\right) \tag{D.12}$$

In our study, we sought to increase Δ to ensure freedom from the "right corner" case. In certain cases, we also made allowance for the reduction in the integral of the field due to the removal of material. This resulted in amp-turn compensation. If there were $(NI)_1$ amp-turns for a depth of Δ_1, the amp-turns $(NI)_2$ compensating for a depth of Δ_2 were:

$$(NI)_2 = \frac{L_f - \Delta_1}{L_f - \Delta_2}(NI)_1 \tag{D.13}$$

Following the procedure described in Section D.2.2.2, we calculated the amplitudes for each harmonic component relative to the main component. Figure D.4 shows these amplitudes for different values of Δ.. It was apparent that the multipolar content could be considerably reduced.

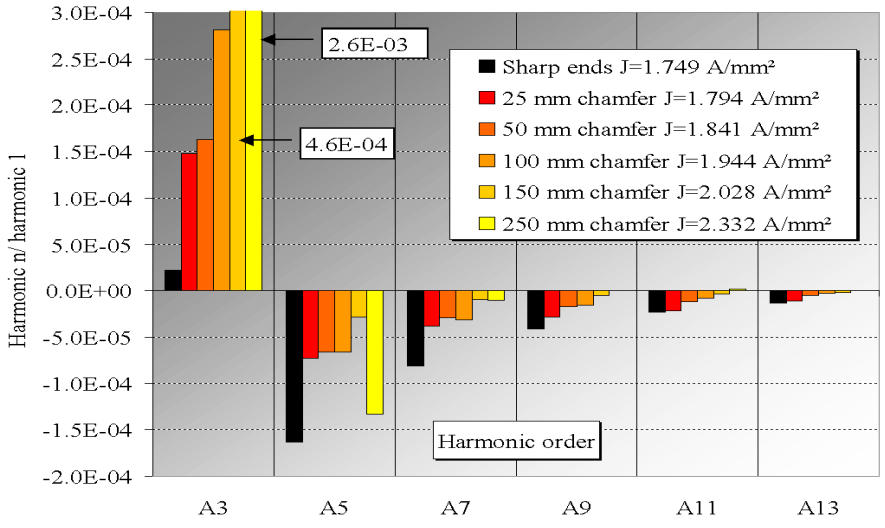

Figure D.4: Relative amplitudes of harmonics with compensation.

By compensating for the amp-turns, we caused extremely high saturation in the transverse corners of the poles, which substantially increased the sextupole (A3). It was possible, by means of a transverse chamfer, to overcome this problem. However, the problem implied an optimum Δ as a function of the level of saturation.

Figure D.5 shows the relative amplitudes of the harmonics in the case where the integral of the field is not compensated for by different values of Δ.. It was verified, for the two cases, that the results remained identical for a reasonable set of values of h_0..

D.4 Application to quadrupole

D.4.1 Description of magnet

The quadrupole used in this study was another SOLEIL project magnet on which a chamfer at 45* had previously been made. The quadrupole had a length of 0.4 m and a gap of 57 mm. Its specification included a nominal magnetic gradient of 15.2 T.m^{-1} (Figure D.6).

D.4.2 Profile

Equation (D.4) once again gave the groove radius change as a function of z:

$$r(z) = r_g \sqrt{\frac{\Delta}{\frac{1}{2}L_f - z}} \tag{D.14}$$

where r_g was the groove radius at the center of region I.
The pole surface equation was then:

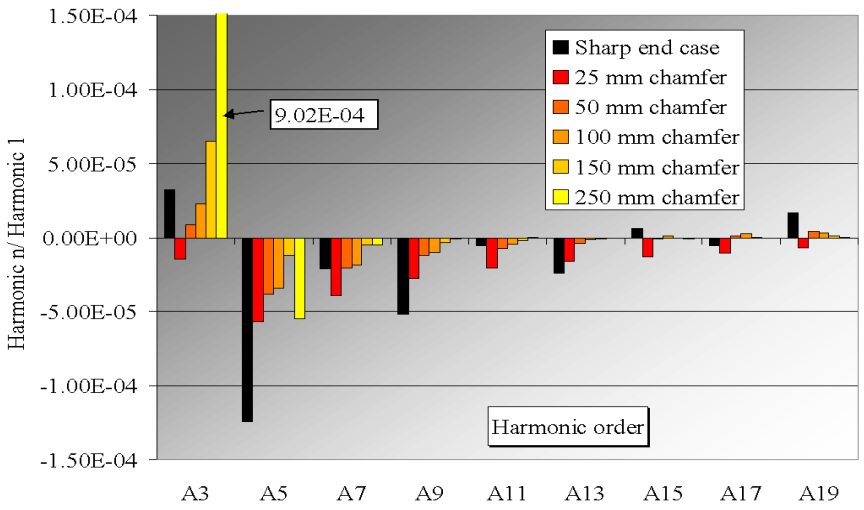

Figure D.5: Relative amplitudes of harmonics without compensation.

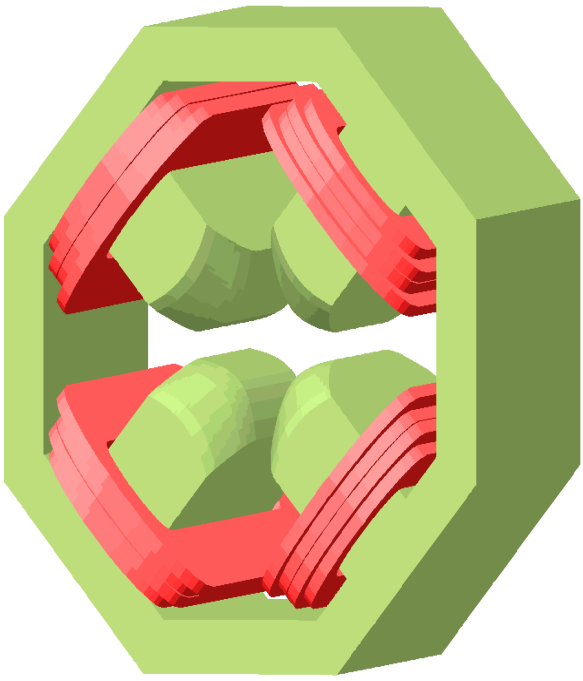

Figure D.6: Complete quadrupole with conductors.

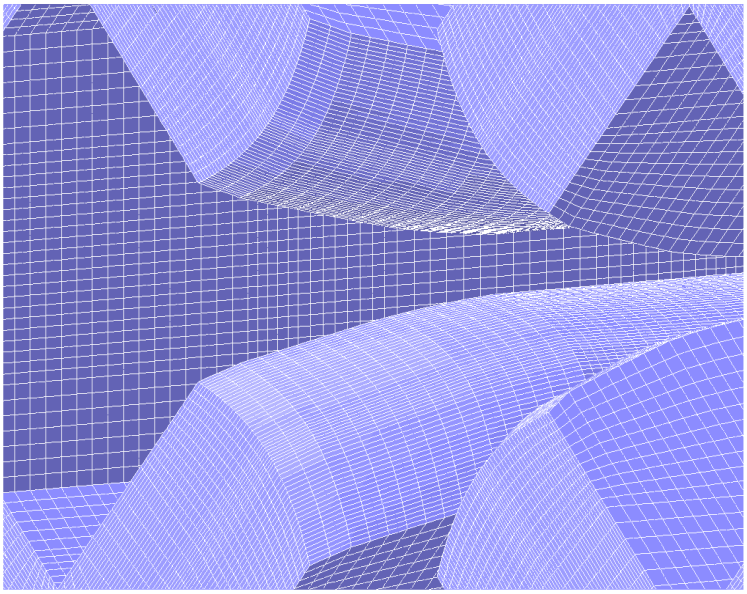

Figure D.7: Chamfer geometry for the quadrupole.

$$xy - \frac{1}{2}\left[r(z)\right]^2 = 0 \tag{D.15}$$

It is noteworthy that the transverse sections had different hyperbolas for each longitudinal position (Figure D.7). Similarly, depth Δ was given by the following expression:

$$\Delta = L_f \left(1 - \frac{G_{dyn} r_g}{2\mu_0 NI}\right) \tag{D.16}$$

where G_{dyn} was the gradient given in the specification.

To operate at a constant integral, it was also necessary to compensate for variation in the value of the gradient integrated over the length with amp-turns. As for the dipole, the optimum depended on saturation. Figure D.8 shows the different relative amplitudes of the undesirable components in the uncompensated case. Also for this case, it was checked that the results remained identical for a reasonable set of values of h_0.. This proves that only the first facets are critical when the pole is at its closest to the axis, as could be expected.

D.5 Conclusion

A coherent analytical model, without transfer/longitudinal coupling, was developed to create the chamfer. The formulation used was very similar to that adapted for beam transport calculation. Good performance was obtained with a view to minimizing the amplitude of the undesirable multipolar components. The method was developed for the dipole and quadrupole cases but could probably be adapted to any multipole. It also demonstrated that the ideal inclination was

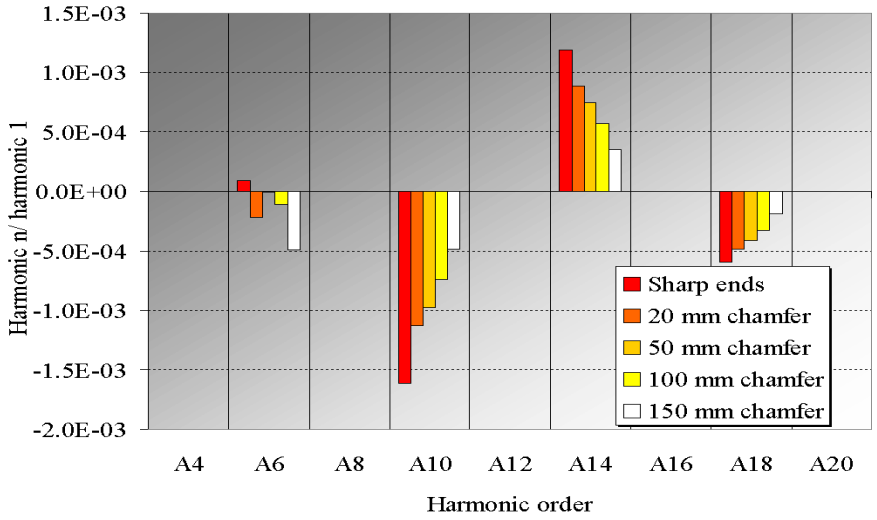

Figure D.8: Relative amplitudes of harmonics without compensation for the quadrupole.

not necessarily 45°, but depended on a number of parameters such as the depth of the chamfer, the air gap, the length of the magnet and the main harmonic. By varying the chamfer depth Δ, the magnetic length could be adjusted. The limitations of the method were due to saturation, although it was possible, in many cases, to overcome the problem with transverse chamfers.

We hope that magnet designers will find this helps them to make chamfers easily and accurately.

Bibliography

[1] Opera-3D/TOSCA, copyright Vector Fields Limited, Oxford, England.

[2] SOLEIL, Basic Design Report, CEA-CNRS, June 1999.

[3] B. Langenbeck, B. Francsak, “Shaping of pole ends to optimize field errors in quadrupole magnets”, IEEE Transactions on Magnetics, Vol. 24, No. 2, March 1988.

[4] O. DelferriËre, C. Evesque, J.P. Pénicaud, “Wide aperture conventional quadrupole for the t_{20} experiment at CEBAF”, Proc. MT15, Vol. 1, p. 195 (1997).

[5] M. Kumada, H. Sasaki, H. Someya et I. Sakai, “Optimization on the end-shaping of a quadrupole magnet”, Nuclear Instrument and Method 211 , p. 283-286 (1983).

[6] R. Duperrier, “Le potentiel électrique dans la zone utile d’un RFQ”, internal report CEA/DSM/DAPNIA/SEA/IPHI/9844 (1998).

[7] R. Duperrier, “A study of the RFQ Radial Matching Section”, internal report CEA/DSM/DAPNIA/SEA/IPHI/9967 (1999).

[8] O. Delferrière, “Décomposition harmonique sous OPERA-3D”, internal report CEA/DSM/DAPNIA/SEA/IPHI/9923 (1999).